Metastable γ-FeNi Nanostructures for Magnetic Refrigeration Near Room Temperature

Submitted in partial fulfillment of the requirements for
the degree of

DOCTOR OF PHILOSOPHY
in
MATERIALS SCIENCE AND ENGINEERING

Huseyin Ucar

B.S., Materials Science and Engineering, Sabanci University
M.S., Materials Science and Engineering, Carnegie Mellon University

Carnegie Mellon University
Pittsburgh, PA

September, 2013

Contents

List of Figures

I would like to thank my advisors Professors Michael McHenry and David Laughlin who have helped pushed me to become the materials scientist that I am today. My gratitude goes out as well to my committee members, Professors Chris Pistorius, Warren Garrison and Victorino Franco for their valuable input and critique of this research. Their critique of my thesis have honed my research and organizational skills and made my writing a little less amateurish. I would also like to extend my most sincere thanks to the past and present graduate students of Professors McHenry and Laughlin: Kate McNerny, Nick Jones, Sam Kernion, Ash Habib, Shen Shen, Alex Leary, Vincent Degeorge, Song Lan, Xinye Liu, Siyang Xu, Whittney Schoenthal, Michael Kurniawan and Jhon J. Ipus. My officemates; Nick, Sam, Kate and Ying Yi deserve special mention who have helped make my learning an enjoyable and stimulating experience. I am indebted to the technical staff; Tom Nuhfer, Jason Wolf and Adam Wise for their assistance in many of the advanced characterization tools. Their patience during the training sessions and encouragement to try new techniqes have been very helpful to gain the skillset I have today.

This work would not have been possible without the support of the National Science Foundation through agreement DMR 0804020.

List of Publications

Huseyin Ucar, Marc Craven, M. E. McHenry and D.E. Laughlin "The Effect of Mo Additions on Structure and Magnetocaloric Effect in γ-FeNi Nanoparticles", *Journal of Electronic Materials*, DOI: 10.1007/s11664-013-2725-6, (2013) (Published Online). **[LINK]**

Huseyin Ucar, John J. Ipus, M. E. McHenry and D.E. Laughlin "Tuning the Curie Temperature in γ-FeNi Nanoparticles for Magnetocaloric Applications by Controlling the Oxidation Kinetics", *Journal of Applied Physics*, **113**, 17A918 (2013) **[LINK]**

Huseyin Ucar, John.J. Ipus, V. Franco, M. E. McHenry and D.E. Laughlin "Overview of Amorphous and Nanocrystalline Magnetocaloric Materials Operating Near Room Temperature", *Journal of Metals*, **64**, 782 (2012) **[LINK]**

N.J. Jones, H. Ucar, J. J. Ipus, M.E. McHenry, and D. E. Laughlin "The Effect of Distributed Exchange Parameters on Magnetocaloric Refrigeration Capacity in Amorphous and Nanocomposite Materials ", *Journal of Applied Physics*, **111**, 07A334 (2012) **[LINK]**

J. J. Ipus, H. Ucar, and M.E. McHenry "Near Room Temperature Magnetocaloric Response of an (FeNi)ZrB Alloy ", *IEEE TRANS. MAG.*, **47**, 2494 (2011) **[LINK]**

Abstract

The observation of a giant magnetocaloric effect in $Gd_5Ge_{1.9}Si_2Fe_{0.1}$ has stimulated the magnetocaloric research in the last two decades. However, the high price of Gd and its proclivity to corrosion of these compounds have prevented their commercial use. To reduce raw materials cost, transition metal-based alloys are investigated to replace rare earth-based materials. Environmental considerations, substitution for scarce and strategic elements, and cost considerations all speak to potential contributions of these new materials to sustainability. Efforts in improving the refrigeration capacity (RC) of refrigerants mainly rely on broadening the magnetic entropy change. One promising technique is to couple two phases of magnetic materials with desirable properties. Second is the investigation of nanoparticle synthesis routes, with ball milling being the most widely used one. The motivation for the nanoparticles synthesis is rooted in their inherent tendency to have distributed exchange coupling, which will broaden the magnetic entropy curve. As proven with the cost analysis, the focus is believed to shift from improving the RC of refrigerants toward finding the most economically advantageous magnetic refrigerant with the highest performance.

Mechanically alloyed $Fe_{70}Ni_{30}$ and $Fe_{72}Ni_{28}$ alloys were characterized in terms of their structural and magnetic properties. Previous studies showed that single phase FCC γ-FeNi alloys with 26-30 at. % Ni have Curie temperatures, T_C, near room temperature. Having T_C near room temperatures along with large magnetization makes γ-FeNi alloys attractive for room temperature magnetocaloric cooling technologies. To obtain a single γ-phase, particles were solution annealed in the γ-phase field and water quenched. The preferential oxidation of Fe during ball milling was used as a means to tune the T_C of the alloy. Refrigeration capacities, RC_{FWHM}, of the $Fe_{70}Ni_{30}$ and the $Fe_{72}Ni_{28}$ alloys were calculated to be 470 J/kg and 250 J/kg at 5 T, with peak temperatures 363 K and 333 K, respectively. The RC_{FWHM} for the $Fe_{70}Ni_{30}$ is higher than the previously reported Nanoperm $(Fe_{70}Ni_{30})_{89}Zr_7B_4$ type alloy and on the same order of magnitude with other Fe-based alloys. The maximum magnetic entropy change values observed for the $Fe_{70}Ni_{30}$ and the $Fe_{72}Ni_{28}$ are 0.65 and 0.5 $Jkg^{-1}K^{-1}$, respectively, at a field of 5 T. These are smaller than those of rare earth magnetic refrigerants showing first order transformation behavior. The larger RC_{FWHM} value results mainly from the width of the magnetic entropy curve in these types of materials.

In a follow up study, nanocrystalline powders of $(Fe_{70}Ni_{30})_{100-x}Mo_x$ (x=1 to x=4) were produced by high energy (SPEX) mechanical alloying. Increasing the Mo content was found to stabilize the FCC phase in mechanically alloyed nanopowders. The T_C of the alloys was lowered with Mo additions, without decreasing the Refrigeration Capacity (RC), due to the additional temperature broadening of the magnetic entropy change. Based on the previous study on the role of disorder, the additional temperature broadening was attributed to the increased positional disorder introduced by the Mo additions into the γ-FeNi system. Alloy with $(Fe_{70}Ni_{30})_{96}Mo_4$ composition was observed to have RC_{FWHM} of 432 J/kg at 5T which is comparable to other prominent magnetic refrigerants operating near room temperatures. The economic viability of these rare-earth-free alloys, along with respectable magnetocaloric properties and potential for scalable production, make them good candidates for magnetic refrigeration applications.

Thesis Outline

This thesis is organized as follows:

Chapter 1 introduces the basic concepts related to the magnetocaloric effect which is followed by an overview of promising magnetic refrigerants. These materials are categorized according to the type of phase transformation they undergo i.e., first order and second order transitions. This chapter is concluded by a brief discussion on oxidation concentrating on the elements used in this study; Fe, Ni and Mo.

Chapter 2 gives background information on mechanical alloying as the alloys used in this study were synthesized by this technique. Each processing variable is introduced with an emphasis on the influence they have on the final properties of the alloy.

Chapter 3 discusses the kinds of motivating applications that inspired us to begin this research.

Chapter 4 can be considered as the heart of this document. While chapter 2 deals with the synthesis aspect of materials paradigm, this chapter bridges the structure, properties and performance relationship in γ-FeNi system. It elucidates how certain materials' properties can be tuned either by adjustments in composition or processing variables.

Chapter 5 briefly summarizes all the work done and chapter 6 presents ideas to consider for future studies.

1 Introduction

In the last decade, there has been an increased interest in magnetocaloric materials. Among many of the applications, the current interest has been on magnetic refrigeration near room temperature because this technology is energetically more efficient than that based on conventional gas compression refrigeration, by about 20 % [1, 2]. Besides being energetically more favorable, magnetocaloric materials are also more environmentally friendly because ozone-depleting and global warming gases are not used. The absence of a compressor in magnetocaloric cooling technology allows for compact design and noiseless operation. Moreover, this technology can be used at atmospheric pressures which would make it possible to use in air conditioning applications and refrigeration systems in automobiles as well.

The analogy between a magnetic and conventional gas refrigeration can be made by applying the laws of thermodynamics to a gas and a magnetic system separately. Application of classical thermodynamics proceeds by combining the first and second laws of thermodynamics. For a reversible system, a substance can change its internal energy as a result of either a work or heat transfer thus yielding the following relation;

$$dU = TdS + dW \tag{1.1}$$

where dU is the differential change in internal energy, TdS is the heat absorbed by the system and dW is the work done on the system. Work can be done on a system in many forms (mechanical, electrical, magnetic etc.). Considering a gas system, Eq.1.1 can be modified as;

$$dU = TdS - PdV \tag{1.2}$$

Where pressure (P) and volume (V) are conjugate properties that define the amount of work transferred to a system.

If the system is a collection of magnetic dipole moments being aligned by an external mag-

netic field, H, at a constant volume, V, then Eq.1.1 becomes;

$$dU = TdS + VHdM \tag{1.3}$$

Comparison of Eq.1.2 and Eq.1.3 reveals that, just as the applied field is analogous to the pressure so is the magnetization to the volume. Fig. 1.1 is an illustration that shows the similarity between the two mechanisms as far as the thermodynamic properties are concerned.

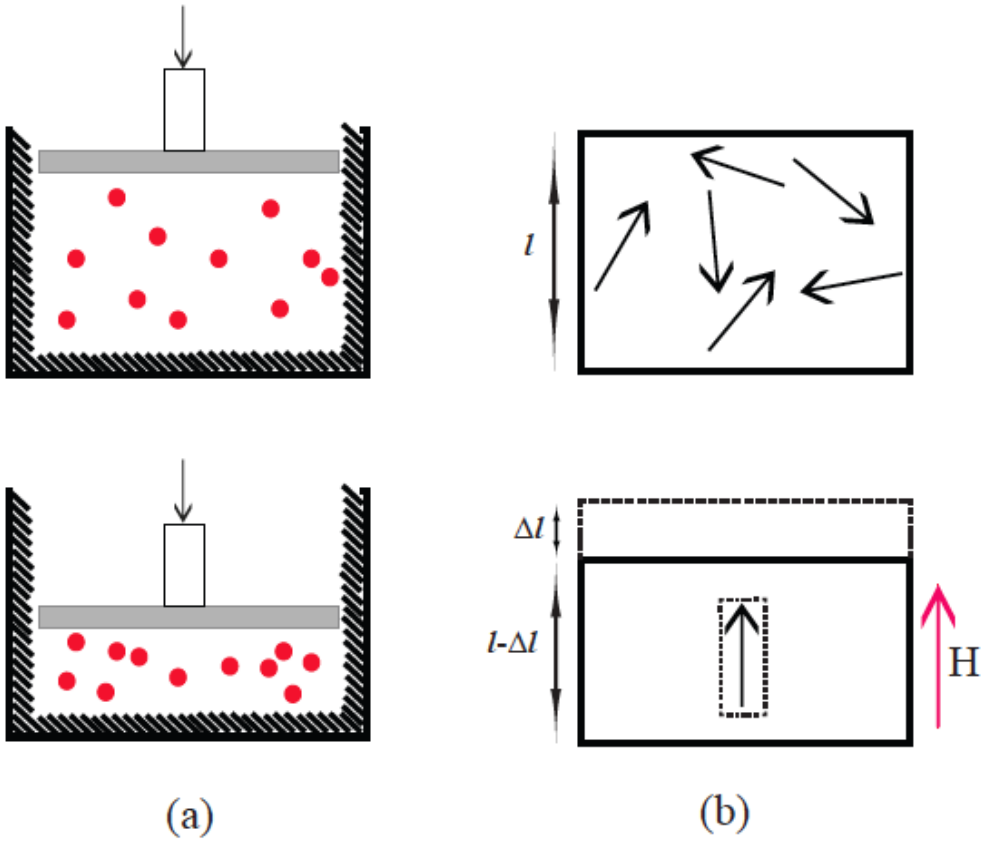

Figure 1.1: Illustration of (a) mechanical work transfer, (b) magnetic work transfer.

In a compressible substance, increasing the pressure by an external force reduces the intermolecular distance thus leading to a reduction in the entropy. In a similar fashion, applying an external magnetic field to a magnetic material with negative magnetostriction aligns the dipole moments and contracts the material along the direction of the applied field. Here, although a material

with negative magnetostriction is presented to highlight the similarity between the two systems, in reality magnetostrictive materials are not very desirable for magnetocaloric applications as their mechanical properties deteriorate after numerous magnetization/demagnetization cycles.

While a number of prototypes have been proposed to prove the efficiency of this technology, the current research focus is on developing new magnetic materials with maximum cooling capacity which operate around room temperature. In other words, materials with enhanced magnetocaloric effect (MCE) between $\sim$250 and $\sim$350 K is an important requirement in order to facilitate commercialization of magnetic refrigeration for a variety of consumer uses [3]. Besides domestic applications, climate control in heat engines and heat pumps are some other applications that rely on the same property. Magnetocaloric materials can be tailored depending on the needs of each application, which can lead to efficient and profitable use of thermodynamic cycles.

The theory behind the MCE will be provided in what follows with the equations of state that are used to describe the magnetic response of materials.

1.1 Magnetocaloric Effect (MCE) and Equations of State

The magnetocaloric effect (MCE) was first described by Warburg [4]. MCE provides a unique way for realizing refrigeration from ultra-low temperatures to room temperature. Interesting MCE materials that rely on nanostructures include paramagnetic salts used for attaining low temperatures [5, 6] and superparamagnetic particles [7] for intermediate temperatures. Materials, with transitions at room temperature and higher, rely on ferromagnetic to paramagnetic or magnetostructural phase transformations.

The MCE is a property of magnetic materials and manifested in the reversible heating/cooling of a magnetic material after the application/removal of a magnetic field. The total entropy of a magnetic material can be presented at constant pressure as;

$$S_T(H,T) = S_M(H,T) + S_r(T) + S_{el}(T) \tag{1.4}$$

where the total entropy, (S_T) is the summation of magnetic entropy (S_M), lattice entropy (S_r), and

electronic entropy, S_{el}. While S_r and S_{el} are functions of temperature only, S_M depends both on field and temperature. On adiabatic magnetization of a material, the spins orient themselves in the same direction thus lowering the magnetic entropy contribution. Adiabatic conditions require that the decrease in magnetic entropy is to be compensated by an equal but opposite change in the entropy associated with the lattice and electrons so that the total entropy remains constant. Since temperature is closely related to the kinetics of the electrons and the vibrations of the molecules, any increase in S_r and S_{el} promotes heating of a material. This temperature change, ΔT_{ad}, is known as the MCE [8].

Another important figure of merit in the evaluation of MCE is the isothermal magnetic entropy change ΔS_M. As the name implies, it is a measure of the magnetic entropy change upon isothermal magnetization and related to magnetic properties of the materials through the Maxwell relation:

$$\left(\frac{\partial S}{\partial H}\right)_T = \left(\frac{\partial M}{\partial T}\right)_H \tag{1.5}$$

After manipulating Eq. 1.5 one gets the following relation;

$$\Delta S_M = \int_0^{H_{max}} \left(\frac{\partial M}{\partial T}\right)_H dH \tag{1.6}$$

where ΔS_M is the magnetic entropy change, M is the magnetization, and T is the temperature. While the majority of ΔT_{ad} measurements are performed for the characterization of materials with first order transition kinetics, ΔS_M is used for magnetocaloric refrigerants with second order transition kinetics. The reason behind this is to avoid an overestimated MCE value which is likely to occur when performing ΔS_M evaluation for the hysteretic first order materials.

The magnetic entropy change due to the application of a magnetic field, H, is determined from temperature and field dependent magnetization curves by integrating Eq. 1.6. Intuitively, materials whose magnetization changes rapidly with temperature are expected to have enhanced magnetocaloric response. This change is greatest around the Curie temperature, T_C, in a conven-

tional ferromagnet or near the absolute zero temperature in a paramagnet [3]. This explains why MCE decreases both below and above T_C as will be demonstrated later in the results section.

From Eq. 1.6, one would consider increasing the field in order to maximize the magnetic entropy to have an enhanced MCE. However, it is important to realize that the maximum field one can achieve in domestic appliances is limited considering the current capacity of permanent magnets. Moreover, increasing the field is an external factor that has nothing to do with the material itself. Therefore, for a tangible achievement, it would be worthwhile to maximize the magnetic entropy by improving the materials' properties. This can be accomplished by finding a novel alloy system or changing the processing variables of an existing alloy system that will result in improved performance.

As much as the ΔS_M is calculated using the experimental data one can also use the equations of state to simulate the experimental result which then can be extrapolated to higher fields to predict the response of magnetic materials with continuous phase transitions; the scaling behavior of first order materials is less predictable. This not only helps to understand the physics behind magnetocaloric effect, it also provides a means to compare the efficiency of magnetic refrigerants produced at different laboratories. Initially, Arrott and Noakes proposed the following equation of state that describes the magnetic response of a material around its critical temperature for materials with second order phase transition [9].

$$H^{1/\gamma} = a(T - T_C)M^{1/\gamma} + bM^{1/\beta+1/\gamma} \tag{1.7}$$

where β and γ are critical exponents describing the temperature dependence of magnetization, M, and inverse susceptibility, (H/M) designated by χ^{-1} respectively. When mean field arguments failed to explain the field dependence of peak magnetic entropy change ΔS_M for materials with second order transition, Franco and Conde proposed to use Arrott-Noakes equation of state [10]. They found that the field dependence of the magnetic entropy change can be expressed as in Eq.

1.8.

$$|\Delta S_M^{pk}| = H^n \tag{1.8}$$

with n = 2/3 according to the mean field arguments [11]. However, this value of the exponent often deviates from experimental observations for soft magnetic materials, and it has been proven that, for a general case, an exponent governing the field dependence of ΔS_M^{pk} is related to the critical exponents in the following way:

$$n = 1 + \frac{\beta - 1}{\beta + \gamma} \tag{1.9}$$

Here β and γ can be obtained through fitting experimental results as described in the following. After determining the Curie temperature T_C of the alloy of interest, isothermal magnetization curves are obtained every 2 K in the proximity of T_C. The extrapolation of the high-field portion of the $M^{2.5}$ versus $(H/M)^{0.75}$ curves is used to obtain the spontaneous magnetization and initial susceptibility from the intercepts with the $(H/M)^{0.75} = 0$ and $M^{2.5} = 0$ axes, respectively [12]. These values were subsequently processed following the Kouvel-Fisher method to obtain the critical exponents and a precise determination of T_C [13]. The predicted and experimental field dependence of the magnetic entropy change curves were proven to be in good agreement for soft magnetic materials with second-order phase transition [14, 15]. However, one should keep in mind that this technique is not suitable for biphasic materials or materials with first-order transition.

The Arrott-Noakes equation is accurate in describing and predicting the M(T) near the transition temperature, but this is not the case at lower temperatures. Gallagher et al.modified the Handrich-Kobe equation by introducing two asymmetric exchange fluctuation parameters, δ_+ and δ_-, yielding [16]:

$$\sigma(T) = \frac{1}{2}[B_s((1 + \delta_+)x) + B_s((1 - \delta_-)x)] \tag{1.10}$$

Here, the disorder of the alloy is taken into consideration by assuming asymmetric exchange inter-

actions present in the amorphous matrix of the nanocomposite alloy. This equation describes the M(T) fairly well at low temperatures for amorphous materials. However, it is insufficient for the regime where the transition from ferromagnetic to paramagnetic phases occurs. Recently, Jones et al. combined the two equations of state to obtain a complete description of the magnetic response for soft magnetic materials [17]. The idea of combining the two models is to bring both the low temperature accuracy and disorder within the context of a modified Brillouin function and the Curie tail together into one curve. With this model, the goal is to determine role of disorder and distributed magnetic exchange interactions in metastable nanostructures for applications in magnetocaloric cooling near room temperature.

An example of the entropy curve calculated from the actual data is shown in Fig. 1.2. Experimental data were obtained from $(Fe_{70}Ni_{30})_{88}Zr_7B_4Cu_1$ alloy. Ballmilled powder was annealed at $700\,^{\circ}\mathrm{C}$ and quenched in water to stabilize the metastable γ-FeNi phase. The combined fit presented gives a more realistic measure of the actual behavior of the material in a broader temperature range compared with the fit from Arrott-Noakes, which displays a plateau at low temperatures, leading to an overestimation of refrigeration capacity (RC).

1.2 Survey of Materials

In this section, current state of the art of magnetocaloric materials are compared based on their operating temperature and magnetocaloric efficiency. The magnetocaloric efficiency of materials is compared by a parameter called refrigeration capacity (RC). However, there are different definitions of RC in the literature. Therefore, it is crucial to compare the same RC types to avoid ambiguity. One early and widely used definition is given by Wood and Potter where the RC for a reversible refrigeration cycle operating between TH (the temperature of the hot reservoir) and TC (the temperature of the cold reservoir) corresponds to the largest rectangle that can be inscribed inside the $\Delta S_M(T)$curve, i.e., $RC_{WP} = \Delta S_M \Delta T$, with ΔS_M the magnetic entropy change at the hot and cold ends of the cycle and ΔT = TH-TC [18]. According to Wood and Potter′s definition, both the peak magnitude and width are equally important, thus making them suitable metrics for com-

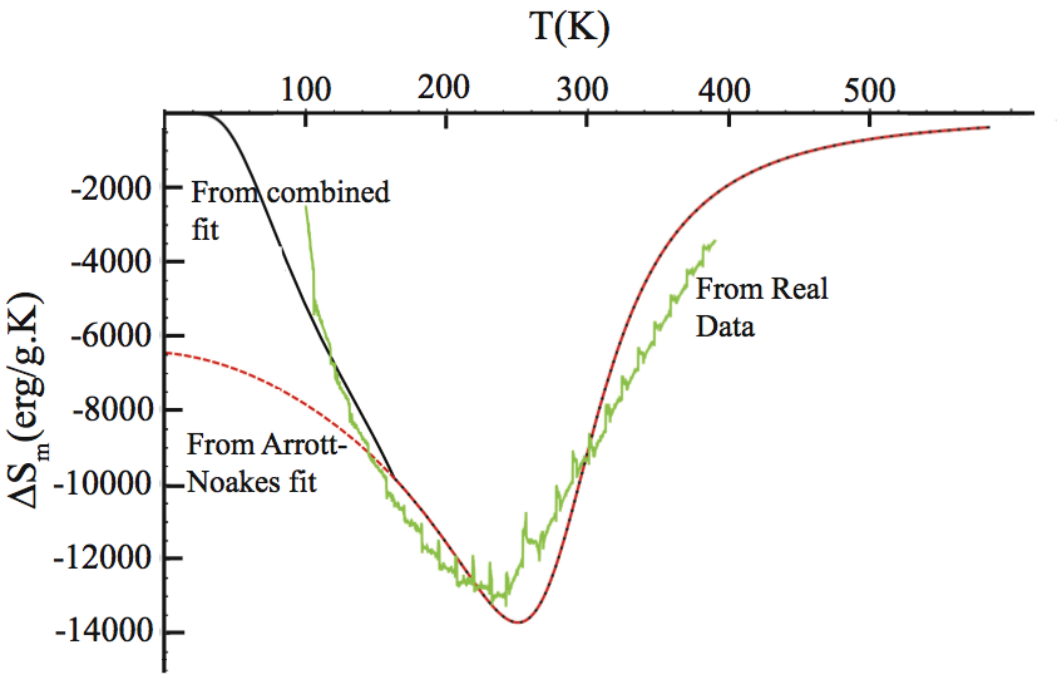

Figure 1.2: Change in entropy integrated from figure with H_{max} at 5T using just the Arrott-Noakes equation (red dashed), the combined fit (black), and averaged experimental data obtained from $(Fe_{70}Ni_{30})_{88}Zr_7B_4Cu_1$ alloy (green).

paring different alloys. Another well-known definition of RC is the product of the peak entropy change times the full width at half maximum (FWHM) of the peak ΔT, $RC_{FWHM} = |\Delta S_M^{pk}|\Delta T$. The third is designated as RC_{AREA}, which is calculated by integrating ΔS_M across the temperature range spanning the half maximum of the entropy change. When comparing different materials, the method that is used to calculate the RC will be specified to avoid confusion.

Another confusion when comparing materials arises due to the differences in the experimental capabilities from one laboratory to another. Researchers tend to present their work at the maximum field they can achieve, which causes difficulties when comparing. This is why understanding the field dependence of ΔS_M and RC is crucial. To address this issue, studies were undertaken to obtain universality curves for the behavior of ΔS_M and show that ΔS_M's field dependence follow a power law[10]. That way, one can extrapolate these metrics of a magnetocaloric material to magnetic fields at which comparison with other benchmark materials is possible.

The materials in this survey can be classified in 2 groups depending on the type of phase

transition they undergo i.e., first-order, second-order transition. While this is not true for every alloy, rare-earth containing alloys have a higher propensity to reveal first order transition kinetics and transition metal based alloys, in general, undergo second order transition. Besides the type of transformation, my goal is also to highlight the differences between rare-earth and rare-earth-free alloys in many aspects.

1.2.1 Materials undergoing first order transition

The characteristics of first order transformation are the latent heat and the discontinuity during transition. The discontinuity manifests itself in the magnetization, entropy and volume upon transformation in such a way that the ∂M/∂T and ∂S/∂T are infinite at the transition temperature. Therefore, materials showing a first order phase transition have large peak magnetic entropy change, $|\Delta S_M^{pk}|$ in a narrow temperature range, ΔT which might limit the refrigerator performance. Besides, these alloys are notorious for their large magnetic/thermal hysteresis upon transformation. Hysteretic nature of these materials is likely to cause overestimation of the entropy change which makes the adiabatic temperature change measurements, ΔT_{ad}, the preferred method for assessment. As will be explored in the following sections, the research focus in these type of alloys is to eliminate the hysteresis thus reducing the associated energy losses and minimize the volume change upon transformation which will reduce the thermal stress in the microstructure.

$Gd_5Ge_2Si_2$

The observation of giant magnetocaloric effect has triggered the magnetocaloric research when Pecharsky and Geschneider observed the potent MCE in $Gd_5Ge_xSi_{4-x}$ with x$\geq$2 (Fig. 1.3).

Initially, it was observed that the the structure of this alloy system changes depending on the Ge/Si ratio. Later on, Morellon showed that the structural transformation coincides with the temperature induced ferromagnetic transition of the alloy with x=2.2 [20] which led him into the conclusion that the giant magnetocaloric effect is a result of the coupling between the magnetic and structural transformation in $Gd_5Ge_xSi_{4-x}$ system.

However, the problem with the $Gd_5Ge_xSi_{4-x}$ compound is that the magnetocaloric response

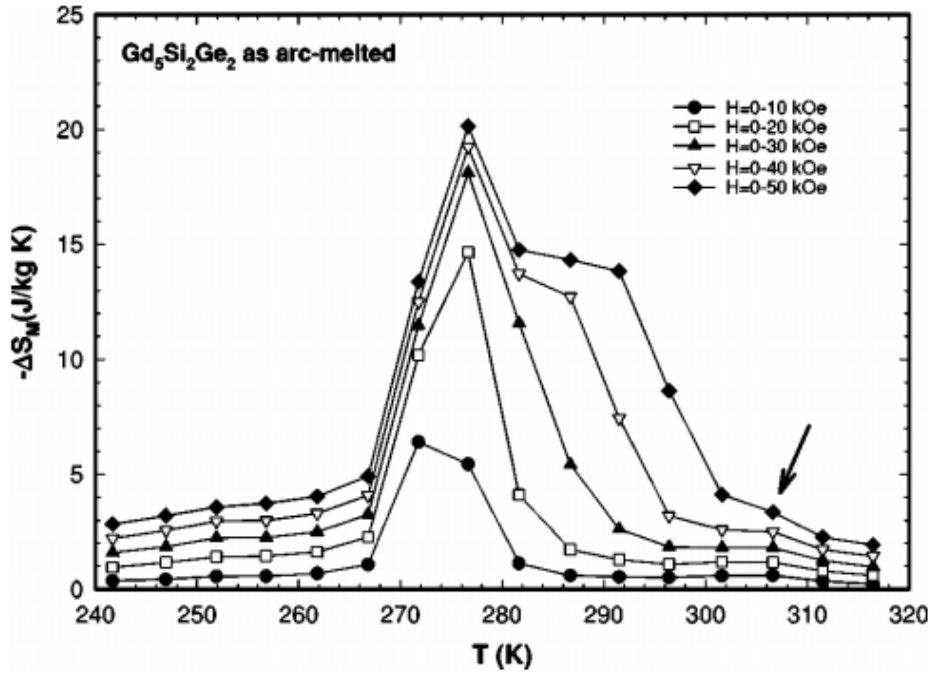

Figure 1.3: The magnetic entropy change ΔS_M of the as arc-melted $Gd_5Si_2Ge_2$ as a function of temperature calculated from magnetic measurements for 10, 20, 30, 40, and 50 kOe magnetic eld changes. The arrow points to the anomaly due to the presence of a second phase [19].

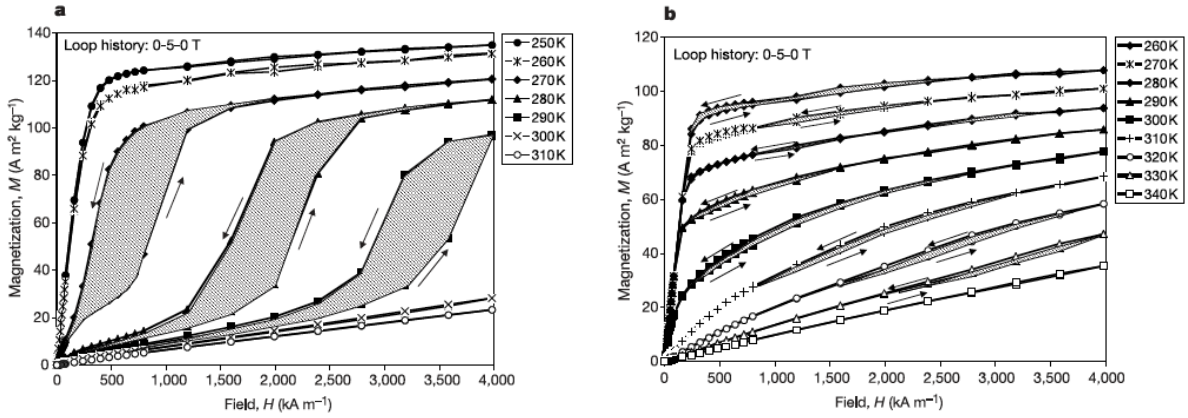

(a) (b)

Figure 1.4: Magnetization versus field curves. Magnetization versus field curves for the $Gd_5Ge_2Si_2$ compound between 250 K and 310 K (a) and for the $Gd_5Ge_{1.9}Si_2Fe_{0.1}$ alloy between 260 K and 340 K (b); arrows indicate the sequence of measurements. The curves qualitatively illustrate the large hysteresis losses of the $Gd_5Ge_2Si_2$ compound and the much smaller values of the $Gd_5Ge_{1.9}Si_2Fe_{0.1}$ alloy. In addition, paramagnetic behaviour is observed above the different temperatures 320 K and 290 K for the Fecontaining alloy and $Gd_5Ge_2Si_2$ compound, respectively.

is accompanied by an undesirable thermal hysteresis. Provenzano et. al., addressed this problem in their study on $Gd_5Ge_2Si_2$ system [21]. They found that minor additions of Fe significantly decrease hysteresis losses (Fig. 1.4). This is at the expense of changing the order of the phase transition from first order to second order which results in the reduction of the peak entropy change with respect to the undoped compound. However, the net refrigerant capacity is considerably increased due to the enhanced breadth of the magnetic entropy curve. This made $Gd_5Ge_{1.9}Si_2Fe_{0.1}$ a benchmark magnetocaloric refrigerant near room temperature and stimulated further studies on magnetocaloric refrigeration.

La(FeSi)$_{13}$

The emerging research impetus due to the discovery of giant MCE in $Gd_5Ge_xSi_{4-x}$ led to the discovery of other magnetocaloric materials that are also known to exhibit respectable magnetocaloric properties. One of the most well known compound among these is La($Fe_{13-x}Si_x$). While, magnetic transformation is accompanied by structural modifications in $Gd_5Ge_xSi_{4-x}$ type alloys, only unit cell volumes are altered in La($Fe_{13-x}Si_x$) without distorting the symmetry of the crystal.

First, it was found that the Fe rich compound La(FeSi)$_{13}$ has peak magnetic entropy change, $|\Delta S_M^{pk}|$, between 200 K and 260 K and undergoes a first-order magnetic transition which is considered the main reason for having a large magnetocaloric effect in this compound. Hu et al. investigated the magnetocaloric properties of $LaFe_{11.7}Si_{1.3}$, which exhibits a T_C approximately 188 K [22]. The metamagnetic transition above T_C of this alloy leads to significant broadening of the ΔS_M, which consequently increases its RC value. Fujieda et al. modified the alloy composition by means of hydrogen absorption, which increased the T_C from 188 K to 291 K without compromising the magnetocaloric response [23]. These findings raised hopes in engineering the magnetocaloric material that is both low-cost and energy efficient.

However, the problem with La(FeSi)$_{13}$ is that, the transition to the ferromagnetic phase is accompanied by a sizable volume change which would decrease the life time of a refrigerator. Put another way, each magnetization-demagnetization cycle expands and contracts the pollycrystalline material which introduces a considerable amount of stress in the microstructure. This eventually

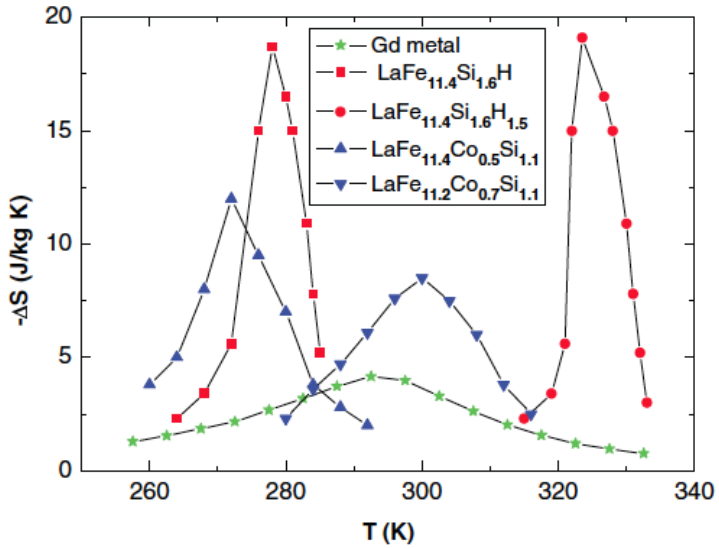

Figure 1.5: Magnetic entropy change for different $LaFe_{13}$-based samples at a field change of 2 T (after [22, 23]).

deteriorates the mechanical properties of the material thus resulting in failure. This was a major problem for this type of alloy until recently when Lyubina et. al., discovered that the introduction of pores into the microstructure significantly improved the resistance of bulk material against the lattice expansion [24].

Besides magnetocaloric properties, the soft magnetic properties of $La(FeX)_{13}$ alloy system with $NaZn_{13}$ structure was studied by Huang et. al. and this compound was also recommended as an alternative to Hiperco type alloys for high frequency applications [25].

FeRh

FeRh with ($\approx$ 1:1 stoichiometry) constitutes another class of alloy system with a giant magnetocaloric effect near room temperature by undergoing a first order transition. The transition from antiferromagnetic to ferromagnetic state can be induced either by heating or applying a magnetic field.

Initially, the giant MCE of FeRh was reported to drop precipitously after the first magnetization cycle due to the hysteretic nature of FeRh [26]. Then, it was pointed out by Manekar and Roy that this was a result of the presence of virgin curve and the erroneous calculation of the magnetic entropy [27]. They claim that the reproducibility can be achieved if the ”envelope

curve" (magnetization curve after 2^{nd} field increase) is used instead of the virgin curve in magnetic refrigeration.

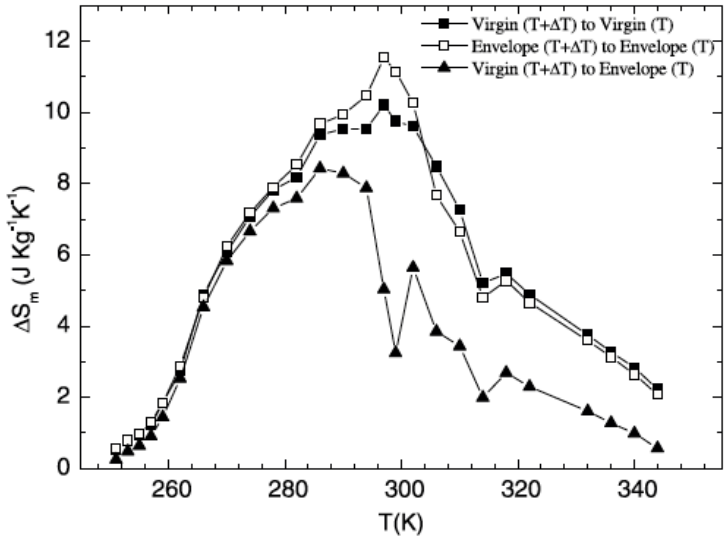

Figure 1.6: Change in entropy as a function of temperature for a maximum field of H = 5 T. The change in entropy is calculated for three possible histories of the sample

As it is obvious in Fig. 1.6, the magnetic entropy is much smaller when the calculation is carried out using the virgin and envelope curves. According to Manekar and Roy, the reduction stemming from the hysteresis losses can be eliminated when the differences between two envelope curves are taken. In an application, this can be realized when the first field increase/decrease is done isothermally which is then followed by an increase in field in an adiabatic environment.

The applicability of the proposed technique in an application or the change in volume during the phase transformation of this alloy are some of the concerns that undermine the reliability of this material.

MnAs based compounds

The transition temperature for MnAs itself is at 317 K which can be tuned by additions of Sb without compromising from the peak magnetic entropy [28]. However, this alloy possesses a large thermal hysteresis and a volume change due to the magnetic transition. Moreover, the concerns over the use of a biologically active element, As, makes this compound undesirable for magnetocaloric applications.

Heusler Alloys

Heusler alloys undergo a displacive and diffusionless transformation from high temperature austenite to low temperature martensite. This transition is thermally induced and quite sensitive to the changes in the composition. The idea is to bring the martensitic and magnetic transitions to the same temperature which would result in a relatively larger mangetic entropy change. Ni_2MnGa type alloys are one of the most well known Heusler alloys with respectable magnetocaloric properties. However, the volume changes during the martensitic transition is a major problem in these alloys which inevitably affects the life time of the material. The magnetocaloric properties of MnAs and NiMnGa type alloys are illustrated in Fig. 1.7.

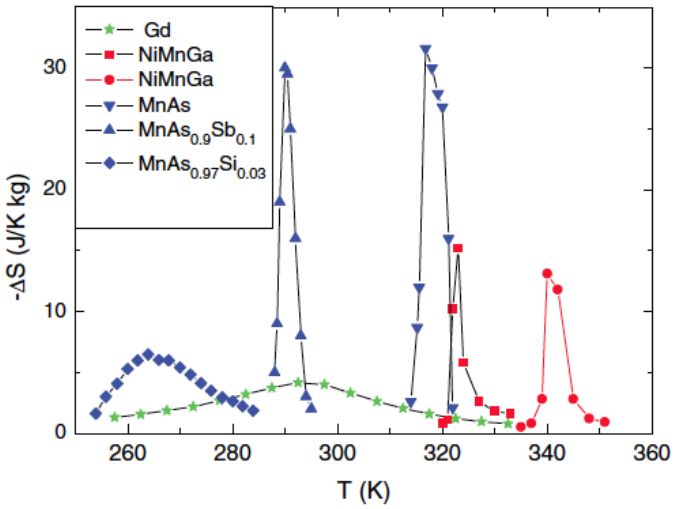

Figure 1.7: Magnetic-entropy change for MnAs and $Mn_{1+x}As_{0.9}Sb_{0.1}$, and two NiMnGa alloys at a field change of 2 T. (after [29])

Some of the NiMn based Heusler alloys with In and Sn exhibit what is known as inverse MCE. These materials cool when magnetized and heat when demagnetized. The cooling effect upon magnetization is mainly because of the structural transformation induced by the magnetic field. The structrucal transformation takes place from a non-magnetic martensite to a ferromagnetic austenite on heating. The heat absorbed during the structural transformation happens to be larger than the heat released during magnetic transformation in these alloys thus resulting in a decrease in temperature upon magnetization.

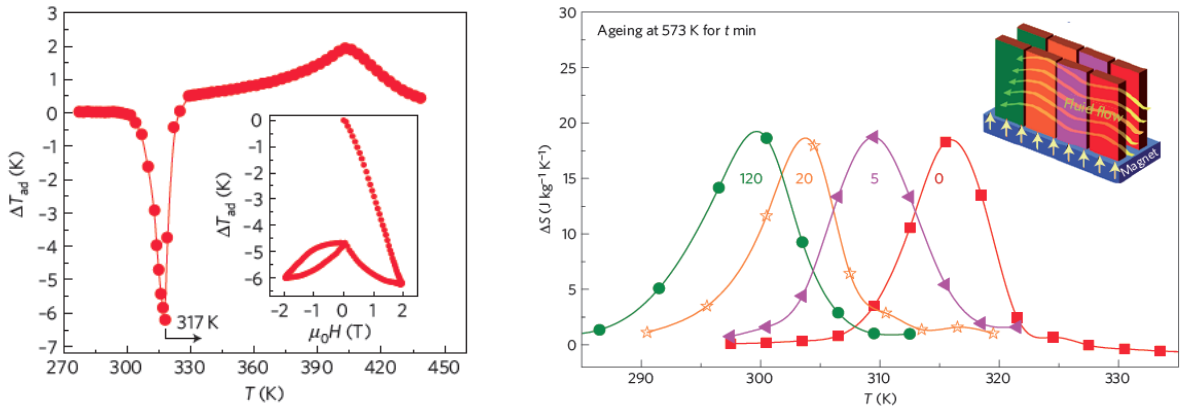

(a) (b)

Figure 1.8: Adiabatic temperature change as a function of temperature in a magnetic field (a). Magnetic entropy changes in 1.9T field after aging for different times. Inset presents the multilayered plates and the direction of flow (b). (after [30])

As illustrated in Fig. 1.8(a), the large drop in temperature upon magnetization is due to the martensitic transformation, ΔT_{ad}^{str}, and relatively smaller increase in temperature is due to the magnetic transformation or conventional MCE effect. The goal is to maximize the ΔT_{ad}^{str} and shift it to near room temperatures. The challenges that need to be overcome are the narrow operating temperature and the large thermal hysteresis during the structural transformation. These points were addressed in a recent study where multilayered plate design (see Fig. 1.8(b)) was recommended to extend the limited working temperature while adjustments in compositon, improvements in the processing technique and application of a hydrostatic pressure were utilized concurrently to minimize the detrimental effects of the hysteresis [30].

While stacking a series of alloys to broaden the transition range seems to be a good idea in an engineering standpoint, using 4-5 different materials should be taken into account when comparing the T_{ad} response of different alloys. Put another way, the T_{ad} response of the whole system should be divided by the number of plates used in the device to avoid the overestimation of the MCE response of this alloy.

1.2.2 Materials undergoing second order transition

Unlike first order transitions, materials with second order transitions transform from one phase to another continuously without any latent heat. The continuous nature of the transformation also yields a finite value for the ∂M/∂T and ∂S/∂T reaching a maximum at the transition temperature i.e., T_C. Becuase second order materials are not hysteretic, studying them are relatively easier and yields more accurate results than first order materials.

In section 1.2.1, the materials undergoing first order transition were presented as having large magnetic entropy changes with respectable magnetocaloric cooling efficiency. However, the price associated with the production of each compound makes them not very desirable magnetic refrigerants. The high price mainly stems from the constituent rare-earth elements in each compound. Therefore, it is important to find new magnetic refrigerants that are low-cost which will facilitate industrial scale up. In order to achieve this goal, transition metals have been investigated for cost reduction instead of rare earth metals. Initially, researchers were reluctant to study transition metal based amorphous alloys due to their relatively smaller peak value of ΔS_M^{pk} as compared with the rare-earth containing alloys. After realizing that the comparison of the RC values are more in favor of the transition based alloys due to the enhanced breadth, researchers concentrated their efforts on obtaining magnetocaloric responses that are comparable to those of rare-earth metals as well as reducing the cost through the use of transition metals.

Fe-based compounds are known for undergoing a second order transformation and the main interest in these alloys is to synthesize nanostructured materials. The significance of nanostructured powders and amorphous ribbons is the fact that these materials have a distribution of magnetic transitions close to room temperature and a broader temperature dependence of magnetic entropy change, giving larger temperature span in magnetic refrigeration. Moreover, nanoparticles are easy to suspend in the solutions thus providing versatility in practical applications. These particles can be used in devices with small dimensions such as magnetic refrigeration of microchips or ferrofluidic pumps where utilizing bulky refrigerants is not feasible.

While there is no compositional restrictions in producing nanostructured powders, there

are a few well known compositional routes that one needs to follow to produce amorphous ribbons. FINEMET, Fe-Si-B; NANOPERM, FeZrB; and HITPERM, FeCoZrB are three well-known compositions required to fabricate amorphous precursors for nanostructured materials [31]. Even though the composition of the phase is crucial in determining the characteristics of MCE, particle size, size distribution and the interaction between the phases in a core-shell type nanoparticle are equally important on the nanoscale and one should take into account these factors to maximize the overall efficiency.

In the following section, a brief survey will be presented on the transition metal based amorphous and nanostructured refrigerants that are considered promising for room temperature applications.

Nanoperm type alloys

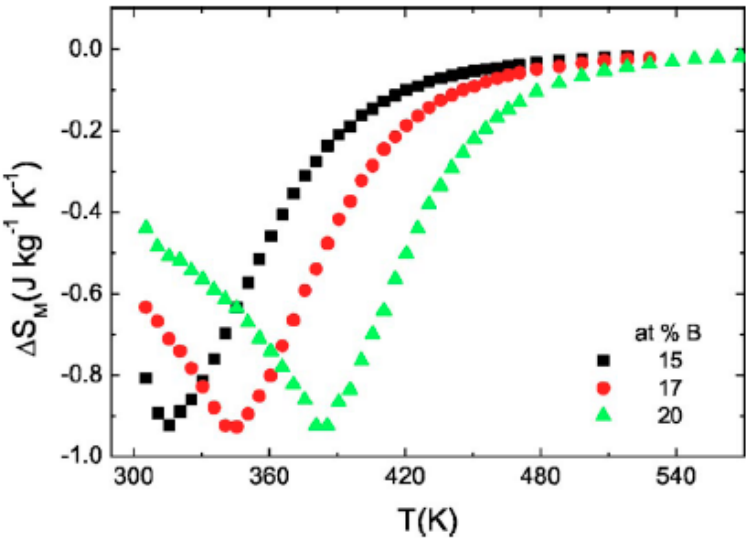

Figure 1.9: Temperature dependence of the magnetic entropy change for a maximum applied field of 15 kOe for $Fe_{91-x}Mo_8Cu_1B_x$ alloy.

Soft amorphous alloys, mainly those of Nanoperm type, were investigated as magnetic refrigerants in several studies [32, 33, 34, 35]. Besides having low cost and reduced hysteresis losses, tunable T_C of soft amorphous alloys are the main reasons for studying them. The tunability of T_C was shown by Franco et al. with additions of boron in the FeMoCuB alloy without altering the

$|\Delta S_M^{pk}|$ of the magnetic entropy curve (Fig. 1.9) [36].

In another study on nanoperm alloys, Caballero-Flores et al. showed that the combined additions of Co and Ni to $Fe_{88-x}Zr_7B_4Cu_1$ leads to amorphous materials with a large magnetocaloric response, which is superior to the well-known aforementioned magnetic refrigerant $Gd_5Ge_{1.9}Si_2Fe_{0.1}$ by 40% in terms of their RC values with a T_C approximately at room temperature [37]. However, it is important to note that while simultaneous additions of Co and Ni increase the cooling efficiency of the Nanoperm $Fe_{88}Zr_7B_4Cu_1$, Co an Ni also raise the T_C of the alloy thus pushing it away from room temperature (Fig. 1.10). This series provides the largest RC values among transition metal-based amorphous alloys published so far.

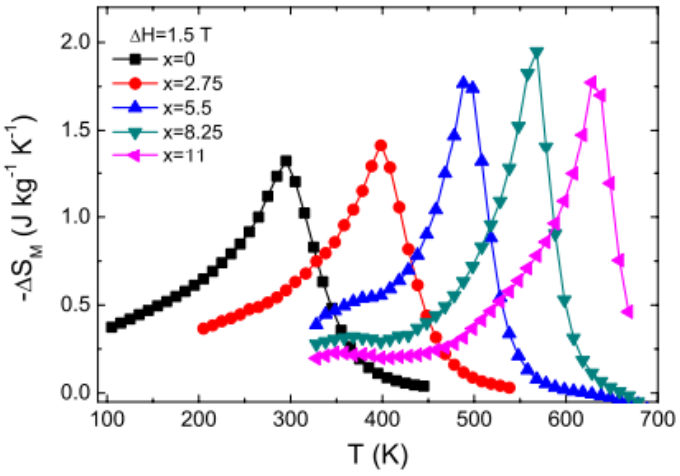

Figure 1.10: Temperature dependence of the magnetic entropy change corresponding to a magnetic eld change H=1.5 T in the amorphous $Fe_{88-2x}Co_xNi_xZr_7B_4Cu_1$ x=0, 2.75, 5.5, 8.25, and 11 alloy series.

Gd-FeCrB

Law et al. studied the effect of Gd on Fe-B-Cr amorphous alloys and investigated the possibility of tuning the T_C with small inclusions of Gd [38]. Small additions of Gd was shown to allow tuning the T_C and enhancing thermal stability (Fig. 1.11). The best magnetocaloric response in this series of alloys was observed for the $Fe_{79}B_{12}Cr_8Gd_1$, which exhibited larger RC than the benchmark alloy $Gd_5Ge_{1.9}Si_2Fe_{0.1}$ with peak magnetic entropy change around 350 K.

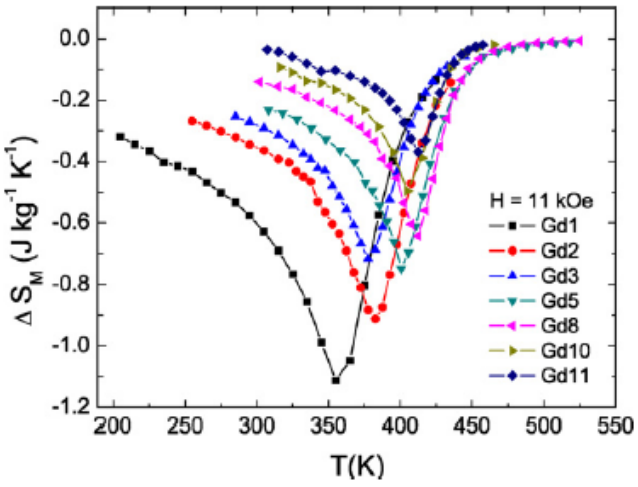

Figure 1.11: Temperature dependence of the magnetic entropy change corresponding to a magnetic eld change H=1.1 T in the amorphous $Fe_{80-x}B_{12}Cr_8Gd_x$ (x = 1, 2, 3, 5, 8, 10, 11).

Pr_2Fe_{17}

Pr_2Fe_{17} is considered as another well-known room temperature magnetocaloric refrigerant. In their study, Gorria et. al. discussed the potential for using these low cost iron based nanostructured material as a room temperature refrigerant [39]. More importantly, this study highlights the differences in the magnetocaloric properties of arc-melted and mechanically alloyed compounds. It was found that with mechanical alloying the maximum of $|\Delta S_M^{pk}|$ is increased and shifted towards room temperature. Secondly, they reported a reduction of one third in the value of the magnetic entropy change compared with that of the starting bulk alloy while the $|\Delta S_M^{pk}|$ peak width is enlarged by a factor close to 2, leading to an increase in the RC value from 506 to 573 J/kg^{-1}. Thirdly, a working temperature difference of at least 125 K between the hot and the cold ends of the cycle is observed which is wider than the bulk alloy. The differences in their magnetocaloric properties between bulk and ball milled powders are illustrated in Fig. 1.12.

The increase in RC is obviously attributed to the broader magnetic entropy curve attained after ball milling. This is due mainly to the fact that nanostructured alloys have a distributed exchange interaction which leads to a distribution of magnetic transition thus giving a larger temperature span in magnetic refrigeration. This explains why materials on the nanoscale range have gained popularity in the last two decades.

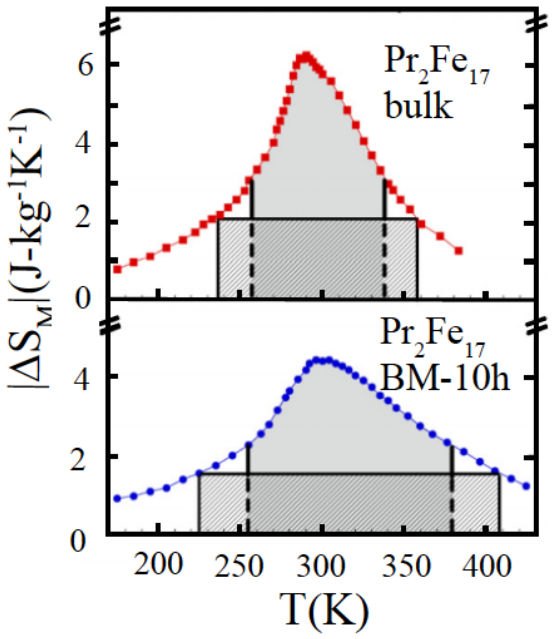

Figure 1.12: Temperature dependence of calculated $|\Delta S_M(T)|$ values under an applied magnetic eld of 5 T, for bulk Pr_2Fe_{17} and BM-10 h Pr_2Fe_{17}.

La(Fe$_{1-x}$Co$_x$)$_{11.9}$Si$_{1.1}$

La(Fe$_{1-x}$Co$_x$)$_{11.9}$Si$_{1.1}$ alloy series are arguably the most promising refrigerants satisfying majority of the criteria listed at the end of this section. These are soft magnetic materials undergoing a second order phase transformation. They can be synthesized via powder metallurgical process, a process quite adaptable for large scale production. The T$_C$ can easily be tuned by altering the Co content in the alloy as shown with the magnetic entropy curves in Fig 1.13 [40] The inset in the same figure also shows that the magnetic entropy of this compound is superior to that of Gd.

In a follow up study, the adiabatic temperature change, ΔT_{ad}, of this compound was studied [41]. ΔT_{ad} is measured to be approximately 2K/T while it is 3K/T for elemental Gd (Fig. 1.14).

All in all, LaFeCoSi compounds exhibit superior performance to many of the refrigerants introduced in this review. However, these alloys are notoriously brittle and demostrate a high propensity for corrosion. To circumvent the corrosion problem, polymer coating with water and antifreeze mixture as a cooling fluid is recommended while an improved sintering is believed to

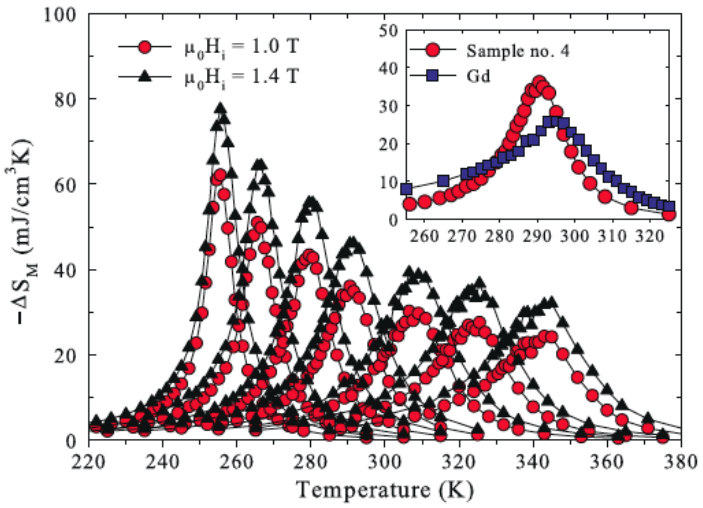

Figure 1.13: Magnetic entropy change, ΔS_M, as a function of temperature for 7 different compositions of $La(Fe_{1-x}Cox)_{11.9}Si_{1.1}$, where x= 0.055, 0.064, 0.071, 0.082, 0.095, 0.108, 0.122 from left to right at a field of 1 and 1.4 T. Inset: Magnetic entropy change of sample 4 compared to that of Gd.

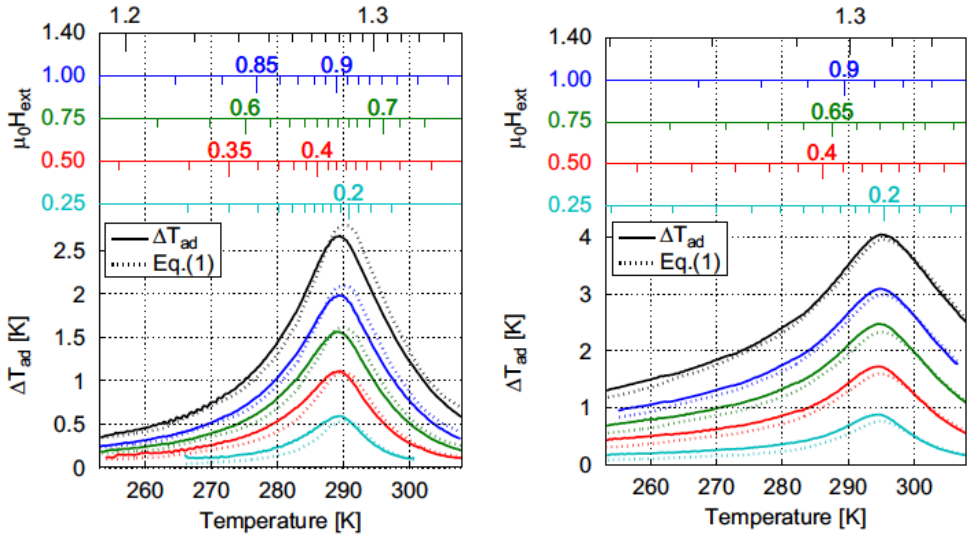

(a) (b)

Figure 1.14: The adiabatic temperature change, ΔT_{ad}, at a field of 1 and 1.4 T for (a) $LaFe_{10.96}Co_{0.97}Si_{1.07}$. (b) ΔT_{ad} of Gd.

enhance the mechanical properties in the studies cited above.

In summary, the epicenter of magnetocaloric research in the last decade has been on synthesizing the most efficient refrigerant while keeping the cost of production to a minimum. Understanding the influence of morphology and microstructure on the magnetic properties will remain

pivotal to accomplish this goal. It is now clear that the properties that are directly related to the MCE (i.e., RC, ΔS_M, ΔT_{ad}) will undeniably play a crucial role in the selection of the best-performing alloy. However, other characteristics such as;

- resistance to corrosion ,
- fast kinetics of transformation,
- large heat conductivity and low specific heat,
- good mechanical properties,
- non-toxicity,
- large electrical resistance,
- minimum environmental impact

are equally important and need careful consideration.

The important metrics for the magnetocaloric materials are summarized in Table 1.1 allowing a fast comparison. This table will be updated with the results of present work in the following sections.

Table 1.1: Peak temperature, peak entropy change, RC_{FWHM} values of promising magnetocaloric materials are presented.

Nominal Composition	T_{pk} (K)	$\lvert\Delta S_M^{pk}\rvert$(1.5T) $Jkg^{-1}K^{-1}$	RC_{FWHM}(1.5T) Jkg^{-1}	RC_{FWHM}(2T) Jkg^{-1}	RC_{FWHM}(5T) Jkg^{-1}	Ref.
$La(Fe_{0.89}Si_{0.11})_{13}H_{1.3}$	291			165.6		[23]
Pr_2Fe_{17}	300				573	[39]
$Gd_5Ge_{1.9}Si_2Fe_{0.1}$	300				630	[21]
$Fe_{88}Zr_7B_4Cu_1$	300	1.3	166		654	[37]
$Fe_{79}Gd_1Cr_8B_{12}$	355	1.42	153		627	[38]
$MnNiGa$	317			30		[42]

1.3 Oxidation

Oxidation is an integral part of this thesis such that the aim is to focus on tuning the magnetic properties by controlling the oxidation in FeNi system. Therefore understanding the oxidation kinetics of each element, the stability of oxides that are formed are crucial and will be investigated in what follows. Not only the presence of an oxide layer makes nanoparticles amenable to functionalize in solutions by the introduction of a polarized surface, it increases the life time of an application by making the particles more stable. Excessive oxidation, on the other hand, lowers the magnetic moment of the material which will inevitably result in decreased efficiency. Therefore, it is of vital importance to control the oxidation so that the nanoparticles will have enhanced properties without compromising the magnetic moment.

1.3.1 Standard free energy of formation vs. temperature diagrams

When there is more than one element that have the potential to oxidize, one would be interested in the oxide products that are likely to form. Ellingham diagrams, plots of standard free energy formation vs. temperature diagrams, are used to assess the relative stability of each oxidation product. In FeNi-Mo system, the oxides that are likely to form for Fe are; (FeO) wustite, Fe_3O_4 magnetite, α-Fe_2O_3 hematite and γ-Fe_2O_3 maghemite, for Ni; NiO and for Mo; MoO_2 and MoO_3. According to an Ellingham diagram, the lower the position of the line the more stable is the oxide and from Fig. 1.15, oxides of iron, FeO, Fe_3O_4 and molybdenum, MoO_2 are the most stable oxides among others hence will form first.

The fact that the oxides of Fe are more stable than that of Ni inspired us to selectively oxidize Fe in the FeNi-Mo system and tune the magnetic properties. In the FeNi system there is a strong compositional dependence of the Curie temperature, T_C, on composition in the γ-phase [44]. Since wustite and magnetite are Fe-based compounds, formation of these oxides depletes the Fe in the core thus changing the core composition. This in turn changes the T_C of the system. Tuning the refrigeration capacity (RC) along with the T_C can be accomplished with the formation of an oxide layer. In tuning the RC, exchange coupling of the 2-phase core/shell structure is exploited. This is

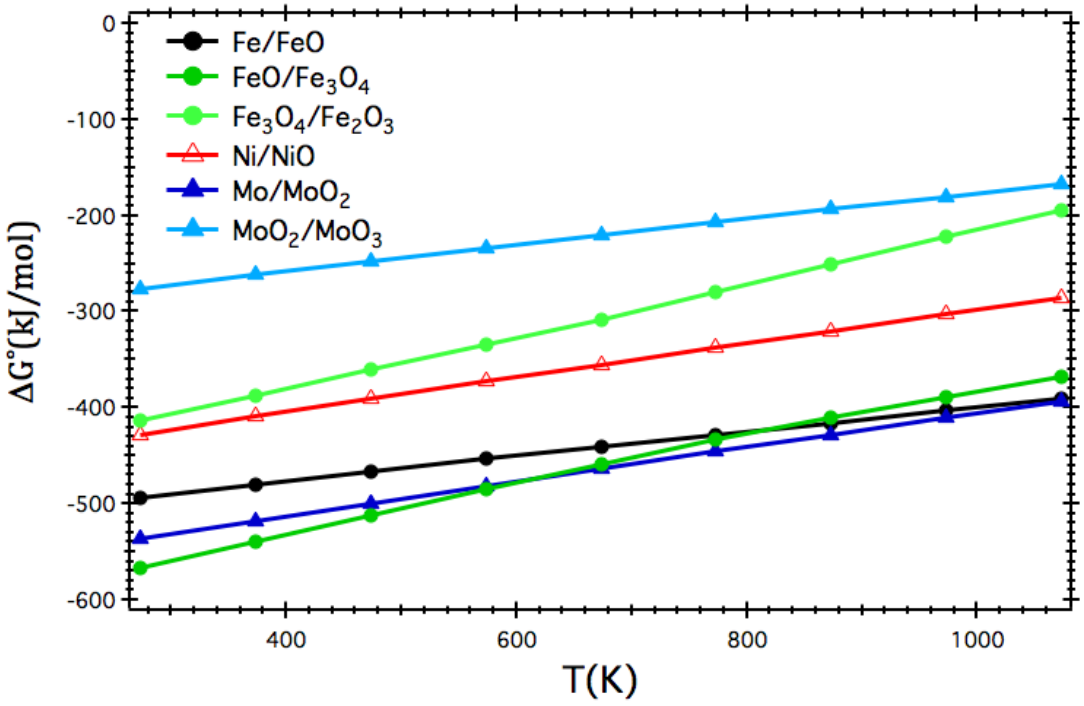

Figure 1.15: An Ellingham diagram depicting the various oxides of Fe, Ni, Mo, formed from their base elements. Plotted using data from [43]

analogous to disorder induced broadening of the transition due to distributed exchange interactions. The ideas presented here will be given in much more detail in the results section.

1.3.2 Kinetics

Oxidation proceeds either by cation or anion migration. The nature of scale growth is determined depending on which mechanism dominates. Put another way, the position of new oxide layer depends on whether cations or anions are transported through the oxide layer such that cation migration leads to scale growth at the scale-gas interface leaving vacancies in the core and anion migration leads to scale formation at the metal-scale interface.

In the initial stages of oxidation when the scale is thin, diffusion from both sides through the scale is rapid and unlikely to be rate limiting. However, the rate of the reaction is determined by the processes taking place on the surface, i.e., decomposition of the reactant gas and the adsorption of oxygen onto the surface. Even though the oxide of Fe was shown to be more stable than that of Ni in Sec. 1.3.1, they both can oxidize during the initial stages on account of being present

on the surface. Equation 1.11 is proposed for oxidation reactions where constant rate kinetics are observed.

$$x = k_1 t \tag{1.11}$$

where k_1 is the rate constant which doesn't change over time, t is time and x is the scale thickness.

As the reaction proceeds, the scale layer thickens and the diffusion of ions through the scale becomes more difficult. At this point the transport of the ions becomes the rate controlling process whereby the rate follows a parabolic rate law given in Eq. 1.12.

$$x^2 = k' t \tag{1.12}$$

Since oxygen ions are bigger than metal cations, the diffusion rate of oxygen ions will slow down more rapidly than that of metal cations. Therefore, oxidation will mainly proceed by the cation diffusion to the surface and Fe will oxidize more rapidly because of having a larger diffusion coefficient than Ni in this regime [45].

1.3.3 Oxidation of Fe

Since Fe is one of the basis elements for the alloy types presented in this study, understanding the oxidation of this element is crucial. When Fe oxidizes, it can form wustite (FeO), magnetite (Fe_3O_4), hematite (α-Fe_2O_3) and maghemite (γ-Fe_2O_3) depending on the temperature and partial pressure of oxygen. According to the Fe-O phase diagram in Fig. 1.16, Fe_3O_4 and Fe_2O_3 are the oxides that will form below $570\,^{\circ}\mathrm{C}$ with a relatively small scale thickness. However, when the temperature exceeds $570\,^{\circ}\mathrm{C}$, it forms a three layer oxide that are FeO, Fe_3O_4 and Fe_2O_3 with FeO next to the metal layer as illustrated in Fig. 1.17.

Wustite has a high defect concentration which facilitates the diffusuon of ions thus causing this layer of oxide to be very thick. As for the magnetic properties, it is antiferromagnetic meaning the spins in the lattice cancel each other out thus leaving no magnetic moment in the structure.

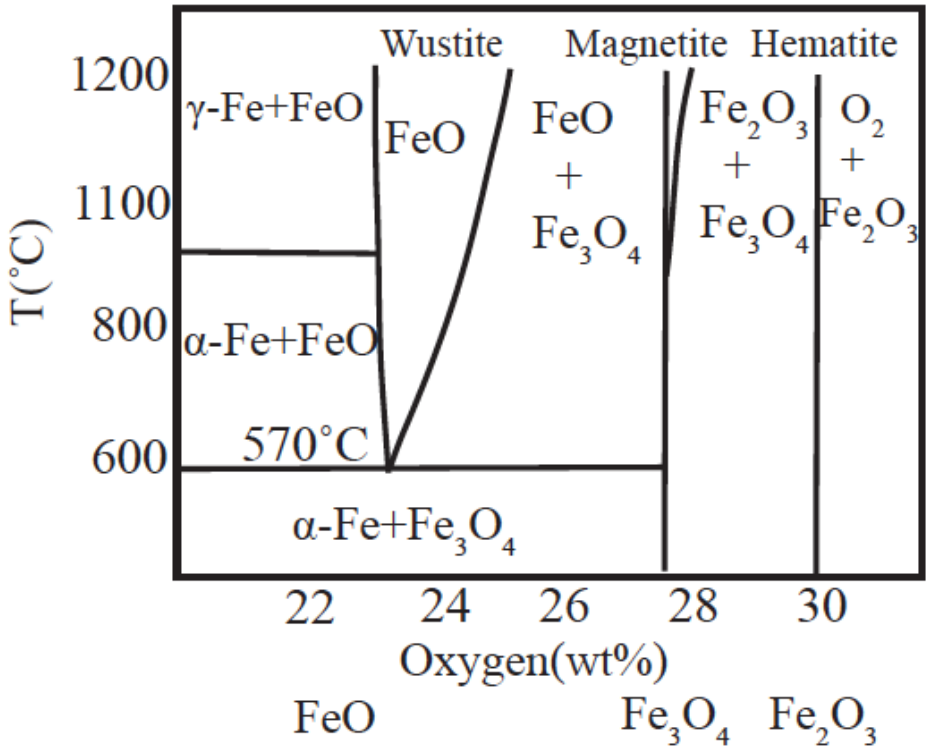

Figure 1.16: The Fe-O Phase Diagram

Magnetite is the second layer that is formed after wustite. It has an inverse spinel structure with divalent Fe^{2+} ions occupying octahedral sites and Fe^{3+} ions occupying tetrahedral sites. Magnetite is a ferrimagnet with a specific magnetization of σ =84 emu/g [46]. This moment is a result of Fe^{2+} and Fe^{3+} ions that are pointing in opposite directions. Since they have unqeual magnetic moment due to their valence electrons, the moments don't completely cancel out thus giving a net magnetization.

Maghemite adopts the same crystal structure as magnetite except the fact that it doesn't have divalent Fe^{2+} ions. Both tetrahedral and octahedral sites are occupied by trivalent Fe^{3+} ions. It is also a ferrimagnet with a specific magnetization σ= 74 emu/g [46].

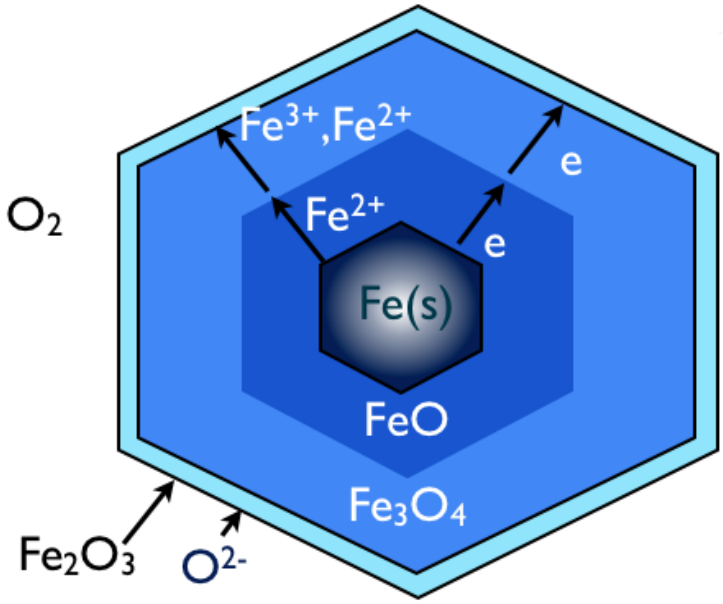

Figure 1.17: Schematic of a nanoparticle showing the oxidation of Iron above 570 °C

2 Alloy Synthesis and Characterization

2.1 Techniques used to synthesize metastable structures

The scientific framework of this thesis is to link each element of the materials paradigm i.e., synthesis→ structure → properties → performance for the FeNi nanostructured alloys. In this section, my objective is to introduce the systematic synthesis techniques and processes that are used to obtain precisely tailored set of properties for demanding applications. Then, the discussion will revolve around the synthesis and processing variables pertinent to this study which will be followed by a description of the characterization techniques used to assess the properties and performance of the alloys in this study.

It is now widely accepted that control of structure and properties is much easier when materials are processed under non-equilibrium conditions [47]. Rapid solidification from a liquid phase [48], mechanical alloying [49], plasma processing [50] and vapor deposition [51] are some of the well known methods to synthesize materials under non-equilibrium conditions. The common purpose of all these techniques is to push the material away from its equilibrium state by energizing it. This energy is supplied to the material by melting, irradiation, application of pressure or mechanical energy in the case of mechanical alloying. The characteristics of a metastable structure is evaluated by the excess energy that is stored as compared with the equilibrium structure. Table 2.1 summarizes how far a material departs from its equilibrium state when processed through different techniques.

Table 2.1: Departure from equilibrium achieved in different non-equilibrium processing techniques.

Technique	Maximum Departure from equilibrium (kJ/mol)
	Ref [52]
Solid state quench	16
Rapid solidification	24
Mechanical alloying	30
Mechanical cold work	1
Irradiation/ion implantation	30
Condensation from vapor	160

Metal powders on the micron and nanoscale can be produced by mechanical or chemical methods. While chemical synthesis route is used for high-purity powders, mechanical alloying is the preferred technique for hard metal and oxide synthesis. It is important to point out that ductility limits the powder production by milling for some metals. For alloys that can not be synthesized through mechanical alloying, atomization could be a viable method as it provides wide range of production rates with particle sizes that are comparable to those of milled powders. Although atomization produces particles having high packing densities, low surface areas which lead to good compressibility and flow characteristics, this method is limited if the elements to be alloyed are immiscible or volatile. For instance, tungsten-copper or iron-silver can not be produced via this technique [53].

Mechanical alloying does surmount the immiscibility barrier since it is a completely solid-state non-equilibrium processing technique which is not bound by the limitations imposed by the phase diagram. Below, the advantages of mechanical alloying are summarized which is followed by an in-depth discussion regarding the extended solubility achieved via this method. With mechanical alloying one can;

- go beyond the solid-solubility limit
- refine the grain size down to nanometer range
- synthesize novel crystalline and quasi-crystalline phases
- develop amorphous phases
- alloy elements that are difficult to alloy via conventional techniques

2.2 Extended solubility with mechanical alloying

In section 2.1, non-equilibrium synthesis techniques were introduced as a tool to produce materials with improved physical and mechanical properties. In this section, mechanical alloying in particular and the possibility of obtaining extended solid solutions will be discussed. The differences between non-equilibrium and equilibrium phases are also reflected on the Fe-Ni phase diagram.

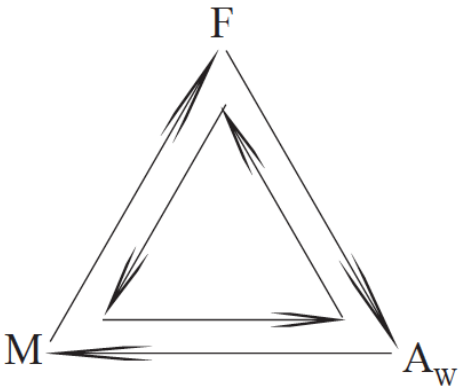

Figure 2.1: A closed loop procedure of fracture (F), microforging (M) and agglomeration by welding (A_W)

Mechanical alloying is a repeated welding, fracturing and rewelding of particles in a high energy ball mill [54]. In the initial stages of mechanical alloying, particles are deformed by cold working through microforging which is followed by a secondary stage during which the particle fracture by fatique failure mechanism. The particle size is continually reduced during these processes. As particles get finer, the coupling forces becomes greater which leads to agglomeration

and the final particles size is determined when the equilibrium is achieved between these forces (Fig. 2.1) [55].

This technique is widely used for the synthesis of nanocrystalline particles. The increased grain boundary volume and large amount of defects introduced via this technique facilitates the diffusivity of the components. Thus, the rapid diffusion of atoms from one grain to another leads to quick homogenization and results in the formation of solid solutions.

Hume-Rothery describes the conditions under which an element could dissolve in a metal, forming a solid solution. These can be listed as (a) an atomic size difference of less than $\pm$ 15 $\%$, (b) the same crystal structure, (c) the same valency, (d) close electronegativity values [56]. To see if Fe, Ni and Mo meet the Hume-Rothery requirements for solubility; the electronegativity and atomic radius of these elements are plotted in Fig. 2.2.

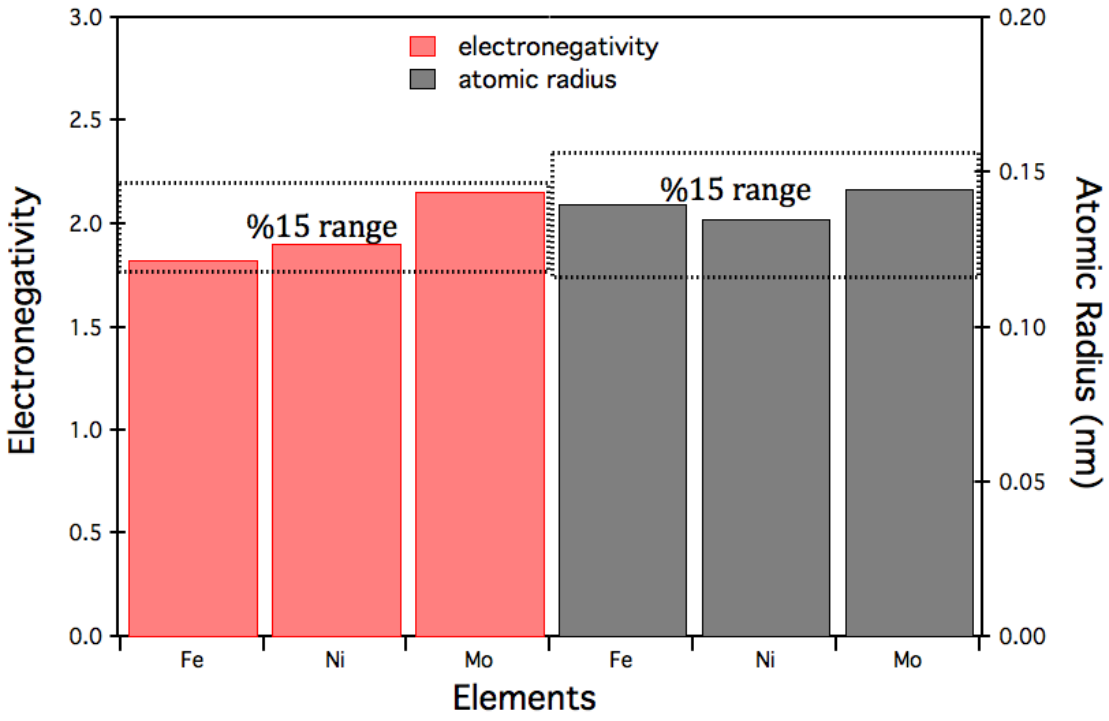

Figure 2.2: (electronegativity vs. atomic size) plot for mechanically alloyed Fe-Ni-Mo powder mixtures.

As Fig. 2.2 suggests, the electronegativity and atomic radius of Fe, Ni and Mo are well within the $\pm$ 15 $\%$ limit, which is an indication that these elements can easily form solid solutions by mechanical alloying.

How does the extended solubility provided by mechanical alloying effect the stability of phases in a binary system? Results of Fe-Ni studies will be used to address this question partly because it is an extensively investigated binary alloy but mostly because the experimental results that will be presented later will be based on this system. In addition to the the extended solubility provided by mechanical alloying, the presence of a negative heat of mixing favors the formation of solid solution over phase separation in FeNi system [57].

The two phase coexistence of mechanically alloyed samples of this study to that of previous data and the equilibrium state of Fe-Ni are presented in Fig. 2.3.

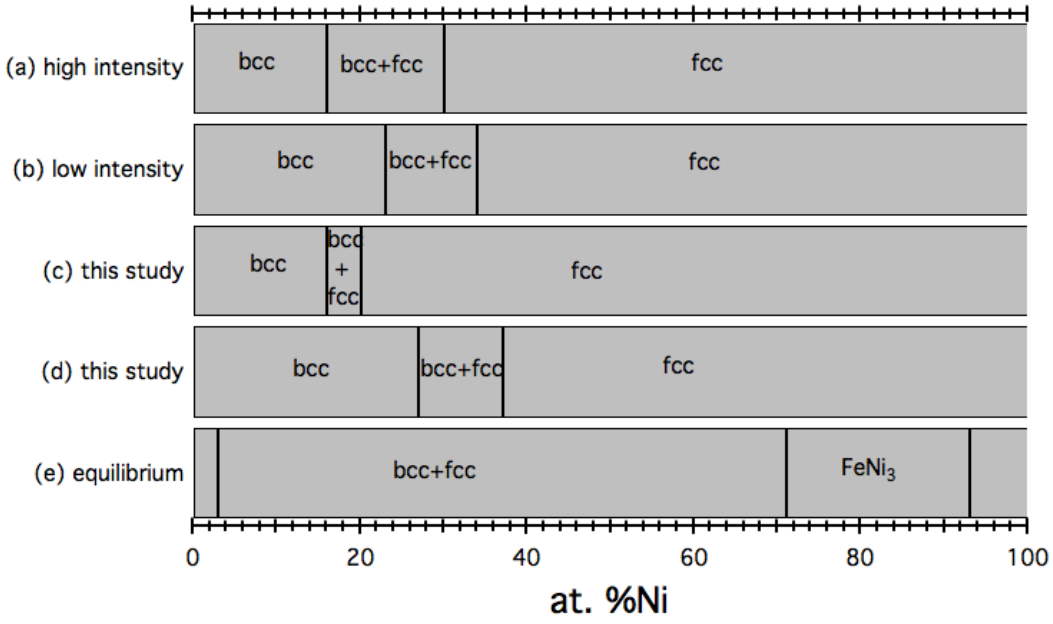

Figure 2.3: Phase boundaries at room temperature for FeNi alloys processed by mechanical alloying compared to the equilibrium state. (a) high intensity Ref. [57], (b) low intensity Ref. [57], (c) mechanically alloyed powders followed by solution annealing at 700 °C and quench in this study (d) as mechanically alloyed powders in this study. (e) equilibrium state Ref.[58]

In contrast with the results of mechanical alloying, thermodynamic equilibrium has a broad range of two phase coexistence with an L_{12} ordered phase, $FeNi_3$ (Fig. 2.3). The equilibrium phases can only be attained by very slow cooling as in meteorites [59] or under electron irradiation [60] on account of Ni diffusivity being very sluggish in the Fe-Ni matrix. Therefore, non-equilibrium phase diagram is modified with respect to the thermodynamic equilibrium by the supersaturation of α-FeNi and γ-FeNi single phases. In other words, the two phase coexistence

boundaries got narrower and shifted to low Ni contents for the MA powders in comparison with the equilibrium state. Furthermore, the influence of annealing the as milled powders over their metastable structure was also investigated. It was observed that, the subsequent annealing of MA samples led to the expansion of fcc single phase region down to 21 at. % Ni and the contraction of two-phase region to 16-20 at. % Ni. The results presented here proves that the non-equilibrium synthesis techniques can be used to extend the single phase regions and obtain improved properties which are not possible through conventional ingot processing routes.

2.3 Synthesis and Processing Variables

Mechanical alloying is a complex process which requires carefully optimized process variables to obtain the desired product. The experimental procedure will be provided in what follows along with a brief introduction to each of the variable.

Type of Mill

There are numerous types of mills used to synthesize powders. They differ in terms of their capacity, ability to control the temperature, ability to minimize contamination etc.. Depending on the purity and quantity of the powder, appropriate mill should be chosen. Since the main purpose of this study is alloy screening, SPEX shaker mill in Fig. 2.4 was used which can produce up to 40 grams of powder in a run.

Milling Container

The milling container should be chosen carefully so that the contamination of the powder is minimized. If the material of the grinding vessel is different from that of the powder, the powder might get contaminated. On the other hand, if the two are made from the same material, then the chemistry of the powder can change if certain precautions are not taken. Hardened steels, sintered corundum, yttria-stabilized zirconia (YSZ) are some of the grinding medium used for mechanical alloying. In this work, hardened steel vials were selected not only because they are relatively more stable and mechanically robust, powders of interest do not differ significantly from steel thus

(a) (b)

Figure 2.4: (a) SPEX 8000 mixer/mill in the assembled condition. (b) Tungsten carbide vial set consisting of the vial, lid, gasket, and balls. Courtesy of SPEX CertiPrep, Metuchen, NJ.

keeping the contamination to a minimum.

Milling Speed

There is a limit for the maximum speed that can be achieved during milling. The speed of the clamps are approximately 1200 rpm and the ball velocity is around 5 m/s for the Spex mills. If the velocity limit is exceeded, the balls get pinned on the inner walls and never fall off and collide with the particles. Therefore, the critical velocity should never be exceeded for the alloy formation to take place.

Increasing the velocity above a critical limit can also facilitate contamination of the powders due to the added impact force. Further, the temperature rise during milling can lead to decomposition of the alloy which is not a main concern for the alloys investigated in this thesis.

Milling Time

The milling time is perhaps the most important parameter among others. It should be chosen such that the desired alloy formation will take place with minimum contamination. The milling time depends on other parameters such as milling speed, type of mill, ball to powder ratio and the temperature during operation. In this study, Fe-Ni binary alloys were analyzed after 10, 30 and 50

hours of milling to observe the effect of milling time on the structure and magnetic properties. As for the Fe-Ni-Mo ternary, the effect of Mo additions on the structure and magnetic properties were studied by milling each alloy for 30 hours but varying the Mo concentration.

Ball to Powder Ratio

Ball to powder ratio is another important variable in milling. It has a direct impact on the operation temperature during milling and the required milling time for the alloy formation. Increasing the ball to powder ratio leads to more heat generation which increases the temperature during milling. It also increases the collision frequency thus more energy is transferred to the powders which decreases the time for alloy formation. It has also been observed that the highest collision energy is achieved when the ball sizes differ. Additionally, using large and small balls minimizes the amount of cold welding and particles coated on the surface of the grinding medium thus increasing the throughput [61]. This is related to the shearing force created between large and small balls which detaches the particles from the surface of the balls. Milling time and ball to powder ratio also have a large impact on the particle size of the final product (Fig. 2.5).

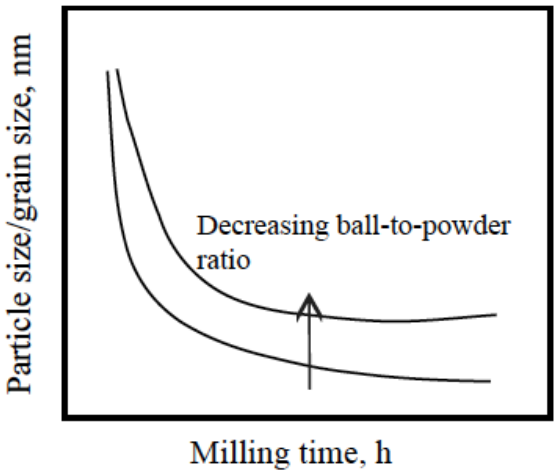

Figure 2.5: The effect of milling time and ball-to-powder ratio on the particle size. Rate of refinement increases with higher ball-to-powder weight ratios. After [62]

Milling Atmosphere

If certain precautions are not taken, milling atmosphere might lead to contamination of the

powders. While nitrogen or ammonia are used for nitride synthesis [63], inert gases are found to be the most effective in eliminating the oxidation of powders. Taking these factors into consideration, the milling container was evacuated and filled with high purity Ar to eliminate the contamination and keep the oxidation level to a minimum.

2.4 Temperature rise during milling

In each collision during mechanical alloying, particles are continuously flattened, welded, fractured and rewelded. As illustrated in Fig. 2.6, approximately 1000 particles are trapped in between the

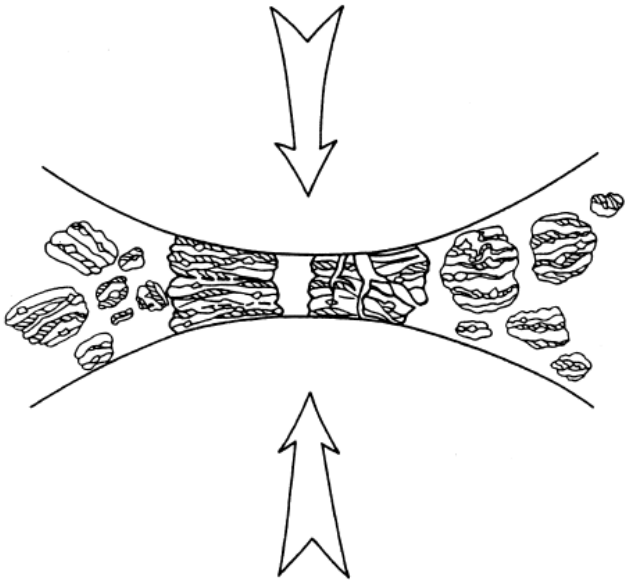

Figure 2.6: Ball-powder-ball collision of powder mixture during mechanical alloying.

balls during which particles are plastically deformed and work hardened. The temperature of the grinding medium increases due to a number of reasons. First, the friction between the balls and the milling container. Second, the transferred kinetic energy from the grinding medium to the particles. Third, the presence of an exothermic reaction during milling. However, it has been reported that approximately %80 of the temperature rise comes from the motor and the bearings while %20 from the factors listed above [64].

The temperature rise in some of the alloy systems can be found in the literature. For the

particles snyhtesized via Spex mill, the temperature rise for the Fe-1.2wt%C system has been recorded 300 °C [65], while it is 180 °C for the Ni-Zr binary system [66].

In this study, the mill was operated intermittently to avoid the excessive heating. However, as will be shown in the results section, the oxidation for the Fe-Ni alloy was unavoidable after extended milling time. The consequences of this will be explored in regards to the structure and magnetic properties in Ch. 4.2.

2.5 Characterization Techniques

X-Ray Diffraction (XRD)

X-ray diffraction is a powerful analytical technique for phase identification and provides structural information. X-ray diffractometer consists of three basic components: an x-ray tube (source), sample holder (sample) and x-ray detector as illustrated in Fig. 2.7

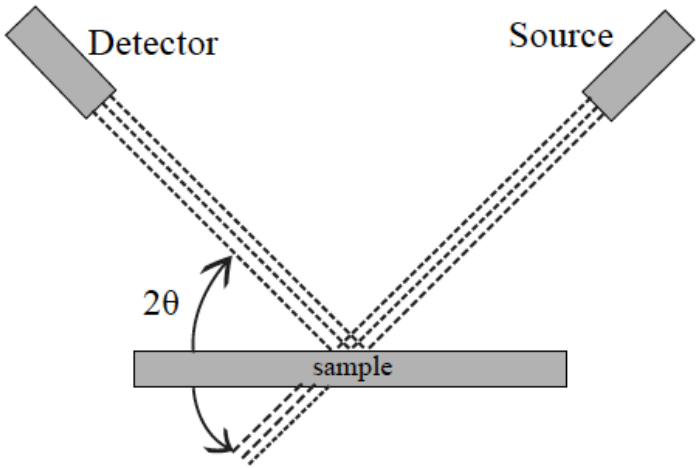

Figure 2.7: Schematic representation of the x-ray diffractometer

When the x-rays are generated by a cathode tube, they bombard the target material with electrons and perturb the inner shell electrons of the target which generates characteristic x-ray spectra. The target materials are usually Cu, Mo, Fe or Cr which produces monochromatic wavelengths. Copper is the most common target material with a λ=0.15418 nm. The reflected x-rays

are recorded by a detector. When the diffracted beams satisfy Bragg's law (Eq. 2.1), they constructively interfere which results in peaks in the intensity profile.

$$n\lambda = 2dsin\theta \tag{2.1}$$

With λ and the angle θ already known, the d spacing can be calculated according to Eq. 2.1.

In addition to the lattice parameters, crystallite sizes can also be calculated using X-ray peak broadening data. There are 3 effects that contribute to the peak broadening; (a) instrumental effects, (b) small particle size, (c) lattice strain in the material [67]. The instrumental and strain contributions can be subtracted for an accurate crystallite size calculation. Alternatively one can calculate it using the Sherrer equation:

$$D = \frac{0.9\lambda}{Bcos(\theta)} \tag{2.2}$$

Eq. 2.2 is only valid when peaks broaden due to the crystallite size only. Thus, this calculation only gives a lower limit for the particle size. This is why double checking the particles size calculated from the indirect X-ray peak broadening studies by direct electron microscope is important. Even though, electron microscope can be used to determine any particle size, X-ray technique can be used only within 1-100 nm range.

X-Ray Fluorescence (XRF)

The principles of XRF are similar to other characterization tools such as SEM-EDS or WDS which involves utilization of the interaction between electron beams and x-rays with the specimen. When x-rays interact with the sample they dislodge the inner electrons thus making the atom unstable. Thereafter, the hole created by the inner electrons gets filled by the electrons in the higher orbitals upon which energy is released in the form of photon. The wavelength of the photon depends on the energy difference between the two orbitals. This procedure is deemed fluorescence and it can be used to detect the elements that are present in a particular sample.

The ease and low cost sample preparation make this a widely used non-destructive analytical

technique in detecting the trace and major elements in bulk samples. Materials science, geochemistry, archaeology and forensic science are some of the disciplines that extensively use this characterization tool. While this technique is well suited for detecting heavy elements with $Z \geq 11$ such as Si, Ti, Al, Fe, Ni, Mn, Mg, Ca, Na, K, P it fails to give a precise and accurate measure of the lighter elements with $Z \leq 11$.

Vibrating Sample Magnetometer

The Vibrating Sample Magnetometer (VSM) is used to measure the magnetic properties of materials at high and low temperatures. It is a widely used technique due to its high sensitivity and ease of operation. Sample can be placed in between the sensing coils by attaching it to the end of the sample rod (Fig. 2.8). Then, the sample starts vibrating in a magnetic field generated by the electromagnets. When the vibrations of the material changes the magnetic flux, it induces a voltage in the pick up coils through Faraday's law of induction. The voltage is usually very small but it gets amplified by a lock in amplifier at the same frequency specified by the sample head.

The VSM Lake Shore 7407 at CMU can measure moments with sensitivities in the μemu range and at fields as high as 20 kOe. Recording the weight of the sample accurately before the experiment is crucial as it can give misleading results if not done properly. For high temperature experiments, a furnace can be attached to the unit which allows for monitoring the change in magnetic moment with temperature. However, it is important to realize that the magnetic moments measured in the furnace are not reliable since saddling the sample in the center of the coils can not be done properly. To circumvent this problem, measurements done at room temperature are used to normalize the high temperature moment values.

Since VSM Lake Shore 7407 did not have the apparatus for low temperature measurements, a liquid helium cooled Physical Properties Measurement System (PPMS) with a VSM head was used instead. Its working principle is very analogous to the VSM 7407 except it can do measurements from 3 K to 1000 K with fields upto 90 kOe.

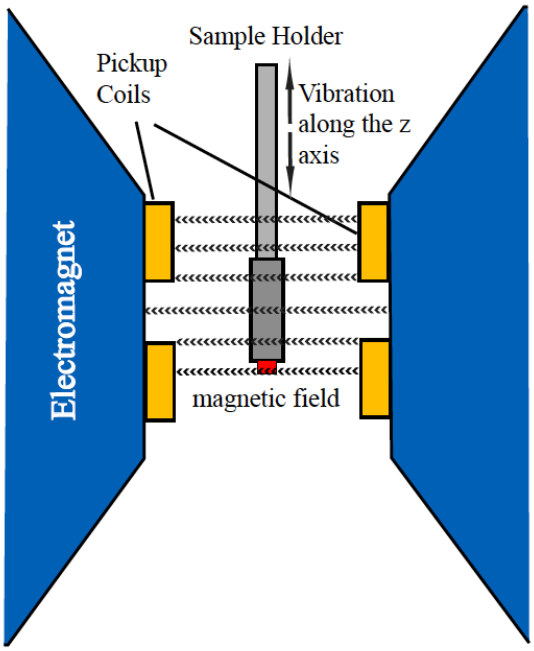

Figure 2.8: Schematic representation of the vibrating sample magnetometer

Scanning Electron Microscope

Scanning Electron Microscope (SEM) allows the observation of materials with a resolution on the nm scale. In SEM, the electrons impinging on the surface get absorbed or bounced off of the specimen from which the information is gathered. Unlike a transmission electron microscope SEM allows the 3-D appearance of a material. Although SEM can also be utilized for quantitative compositional analysis of the sample, it was used mainly for surface characteristics and particle size analysis in this study.

3 Motivating Applications and Hypothesis

3.1 Magnetocaloric Cooling

The magnetocaloric effect is a property of magnetic materials and manifested in the reversible heating of a magnetic material after the application of a magnetic field. When the field is applied suddenly, the process is considered adiabatic and the temperature of the material rises. Magnetic refrigeration, air conditioners, heat engines and heat pumps are some of the well-known applications in which this technology is utilized. For applications operating near room temperature as in air conditioners or refrigeration, the maximum adiabatic temperature change of the magnetic material should be around room temperature for enhanced efficiency. This is accomplished simply by synthesizing refrigerants with T_C's near room temperature.

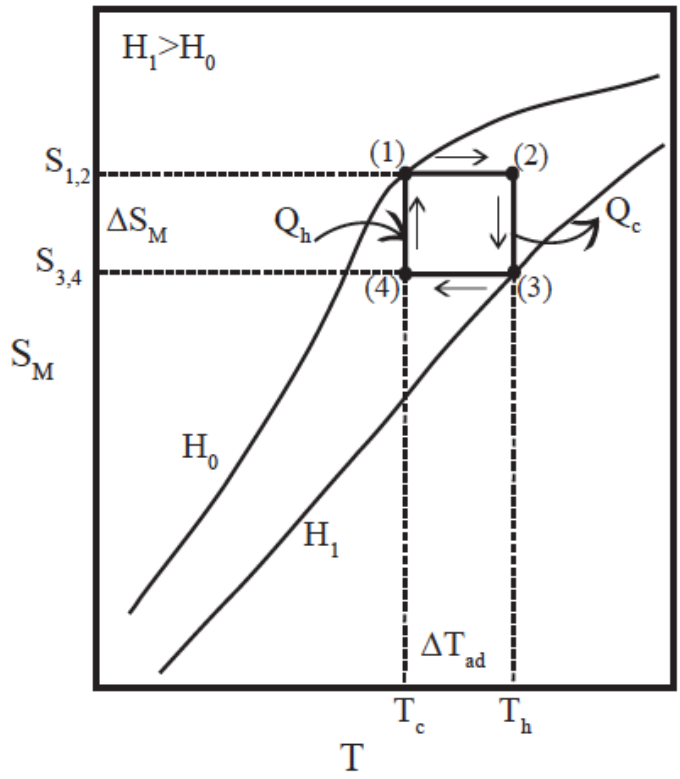

Figure 3.1: S-T diagram of an magnetic refrigeration Carnot cycle.

Construction of a closed thermodynamic cycle using a magnetic entropy (S_M), temperature (T) diagram could aid in understanding the principles behind this technology. In Fig. 3.1, a Carnot

cycle is illustrated which consists of two isothermal and adiabatic magnetization/demagnetization processes. The cycle begins by adiabatically magnetizing the refrigerant upon which the temperature increases from T_c to T_h (Process 1 $\rightarrow$ 2). This is followed by an isothermal magnetization of the material by increasing the intensity of magnetization and maintaining good thermal contact between the refrigerant and the heat sink (Process 2 $\rightarrow$ 3). At this stage, the temperature of the refrigerant is constant while the heat generated is extracted out of the system. In process 3 $\rightarrow$ 4, the intensity of the magnetic field is decreased which lowers the temperature of the refrigerant adiabatically, from T_h to T_c. Finally, the cycle is completed by demagnetizing the material isothermally which brings the system to its virgin state. The efficiency of the system depends on its ability to transfer the heat generated during isothermal magnetization (Process 2 $\rightarrow$ 3) to the hot source and it's ability to absorb the heat from the cold source (system to be cooled) during isothermal demagnetization (Process 4 $\rightarrow$ 1). The temperature spanned upon the completion of the Carnot cycle is the well known magnetocaloric effect and the research efforts in the last decade has been on maximizing the temperature difference while maintaining the material cost at a reasonable level.

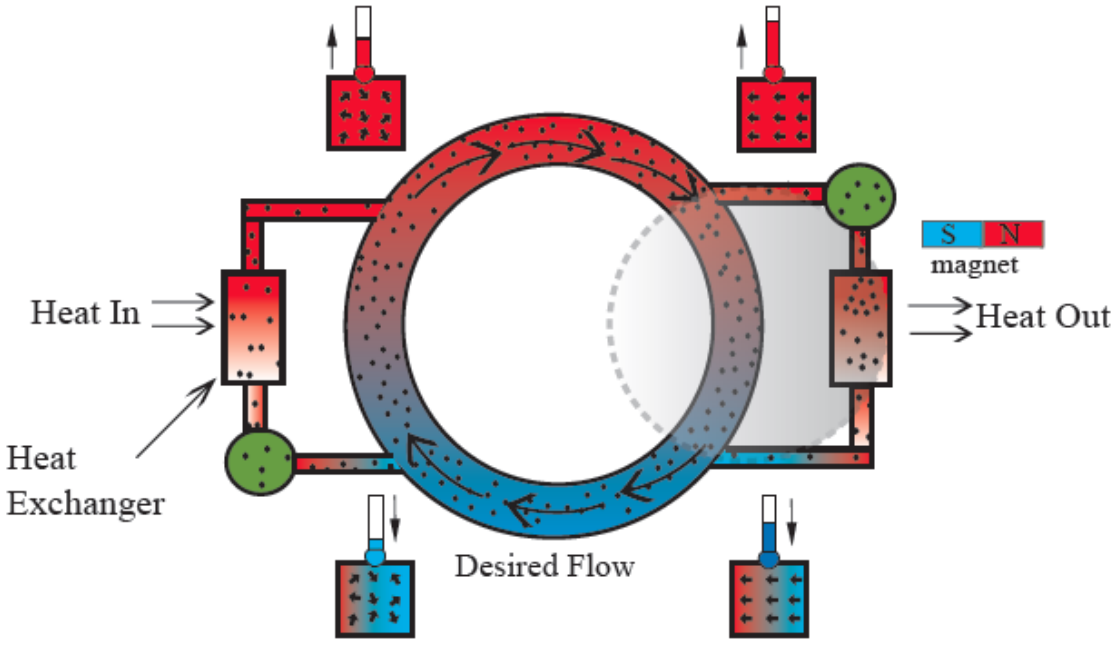

Figure 3.2: Schematic representation of a self-pumping system.

Several magnetic refrigerants were developed in the solid state hoping that the higher density of solids would allow compact design of cooling devices. However, the general consensus is that the slow heat transfer in the solid state would decrease the efficiency of magnetic refrigeration at the same time. This is why colloidal suspension of ferromagnetic particles (ferrofluids) to be used in magnetic refrigeration has been proposed as an alternative in several studies [68, 69, 70, 71]. The enhanced surface area of nanoparticles suspended in the fluid ensures good thermal contact, unlike in a solid state device, thus leading to a fast heat exchange. This is why nanostructured alloys were synthesized in this study which would facilitate their suspension in a liquid carrier. In ferrofluid cooling technology though, achieving a high concentration of magnetic nanoparticles in the fluid and the stability of the system in the long run still seem to be potential bottlenecks that need to be resolved [72]. This is crucial as the efficiency of the device is directly related to the concentration and stability of the magnetic nanoparticles in the fluid.

Fig. 3.2 is a simple depiction of a ferrofluid refrigeration cycle. Consider the nanoparticles at 1 o'clock position out of the magnetic field with temperature T_H. As the nanoparticles enter the magnetic field, their temperature increase adiabatically from T_H to $T_H+\Delta T$. Then, the heat from the nanoparticles is extracted by a heat transfer coil upon which the temperature of the refrigerant is reduced to $T_C+\Delta T$. At 4 o'clock position, as the nanoparticles are rotated out of the high field region, the spins disorient due to the thermal agitation which results in adiabatic cooling from $T_C+\Delta T$ to T_C. As the working material passes through the thermal load, it absorbs the heat from the thermal load and travels back to its original position with the aid of convection. The cycle can be repeated as desired without significant energy loss as this technology is proven to be reversible. The refrigeration cycle is also illustrated with an entropy vs temperature diagram in Fig. 3.3.

Depending on the application, a careful adjustment of the composition of the alloy is needed. If this technology is to be used in domestic applications, the T_C of the nanoparticles should be engineered in such a way that it coincides with room temperature. This is mainly because of achieving greater heat absorption rates due to the magnetocaloric effect when magnetic nanoparticles with T_C's near room temperature are used. As previously introduced, the temperature increase produced

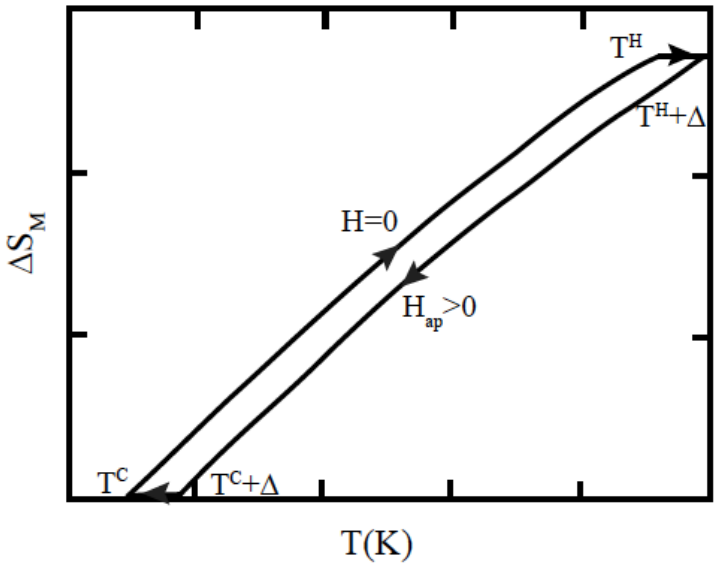

Figure 3.3: A magnetic refrigeration cycle illustrated with entropy vs temperature curves for a ferromagnetic material.

by this effect goes through a maximum at T_C because at this temperature the change in spin order accompanying forced magnetization is greatest.

As stated, this application entails the suspension of magnetic nanoparticles in fluids. This seems to be the only way to utilize magnetism in a liquid medium as there is no known substance whose Curie point exceeds its melting point. The stability of a ferrofluid is an important property that can be perturbed by various factors such as a magnetic field gradient, gravity and dipole-dipole forces that are present in the nanoparticles while thermal energy constantly works to counteract these effects. Each factor will be considered along with the possible ways to achieve the physicochemical stability in a ferrofluid based on the theory developed by Rosensweig [68].

There are three energy terms when considering the stability of a ferroluid. These are:

thermal energy= kT

magnetic energy= μ_oMHV

gravitational energy= $\Delta\rho$VgL

where k is Boltzmann's constant and T is the absolute temperature in Kelvin, μ_o is the permeability of free space, V=$\pi d^3/6m^3$ is the volume for a spherical particle of diameter d, and L is

the elevation in the gravitational field.

Stability against a magnetic field gradient

Upon the application of a magnetic field, nanoparticles are attracted to the field. Thermal energy, on the other hand, works against the magnetic field and randomizes the nanoparticles. The interplay between these two forces determine the stability of nanoparticles against segregation.

$$\frac{thermal\ energy}{magnetic\,energy} = \frac{kT}{\mu_o MHV} \geq 1 \tag{3.1}$$

A high ratio of the thermal energy to the magnetic energy is required for stability. Plugging in the volume of a spherical nanoparticle and rearranging terms in Eq. 3.1 gives us the maximum particle size allowed for a stable solution:

$$d \leq (6kT/\pi\mu_o MH)^{1/3} \tag{3.2}$$

Considering an FeNi nanoparticle subjected to a magnetic field of 500 G with a saturation magnetization of 6000 G in cgs units.

H=4×10^4 A.m^{-1} (SI)

M=4.8×10^5 A.m^{-1} (SI)

T=298 K

corresponding to d$\leq$ 6.9 nm above which the particles are unstable in a solution.

Stability against gravity

Here, the situation is quite similar to the previous case except this time gravity pulls the particles out of the solution while thermal agitation works against it. The stability is determined by whichever force wins out eventually. However, as will be shown in the following calculation, gravity doesn't play a major role in the segregation of the nanoparticles.

$$\frac{gravitational\ energy}{magnetic\,energy} = \frac{\Delta\rho gL}{\mu_o MHV} \tag{3.3}$$

Plugging in L=0.05 m , $\Delta\rho$=ρ_{solid}-ρ_{fluid}=4300 kg.m^{-3} and g=9.8 m.s^{-2}, the ratio of Eq. 3.3 is 0.047.

Stability against particle agglomeration

Nanoparticles in a solution adhere together due to energy resulting from their dipole-dipole interactions.

$$E_{dd} = \frac{1}{12}\mu_o M^2 V \tag{3.4}$$

The magnitude of the dipole energy in Eq. 3.4 to that of thermal energy determines the stability of a solution.

$$\frac{thermal\ energy}{dipole-dipole\ contact\ energy} = \frac{12kT}{\mu_o M^2 V} \tag{3.5}$$

from which the particle size can be obtained as:

$$d \leq (72kT/\pi\mu_o M^2)^{1/3} \tag{3.6}$$

For FeNi nanoparticles the maximum particle size is estimated to be 7 nm. Beyond this value, particles tend to agglomerate due to the dipole-dipole interactions.

To summarize, there are 3 main factors that unstabilize the nanoparticles in a solution which can be listed as gravitational force, external magnetic field and dipole-dipole interactions while thermal energy counteracts them. Comparing their relative magnitude gives a threshold size of the nanoparticles above which these 3 forces dominate thus yielding unstable ferrofluids. This size happens to be ≈7-8 nm for FeNi nanoparticles. This is why synthesizing fine particles on the nanoscale with a high degree of monodispersity is crucial for long term use of ferrofluids.

Besides domestic appliances, magnetocaloric cooling technology can also be utilized in hybrid and electric vehicles. Hybrid vehicles are re-emerging as an alternative to conventional gas-

only internal combustion vehicles. One of the three key components in hybrid vehicles is the permanent magnet (PM) motors as shown in Fig. 3.4 [29]. PM motors are far more advantageous than induction motors in that they allow for compact, light weight design with high torque.

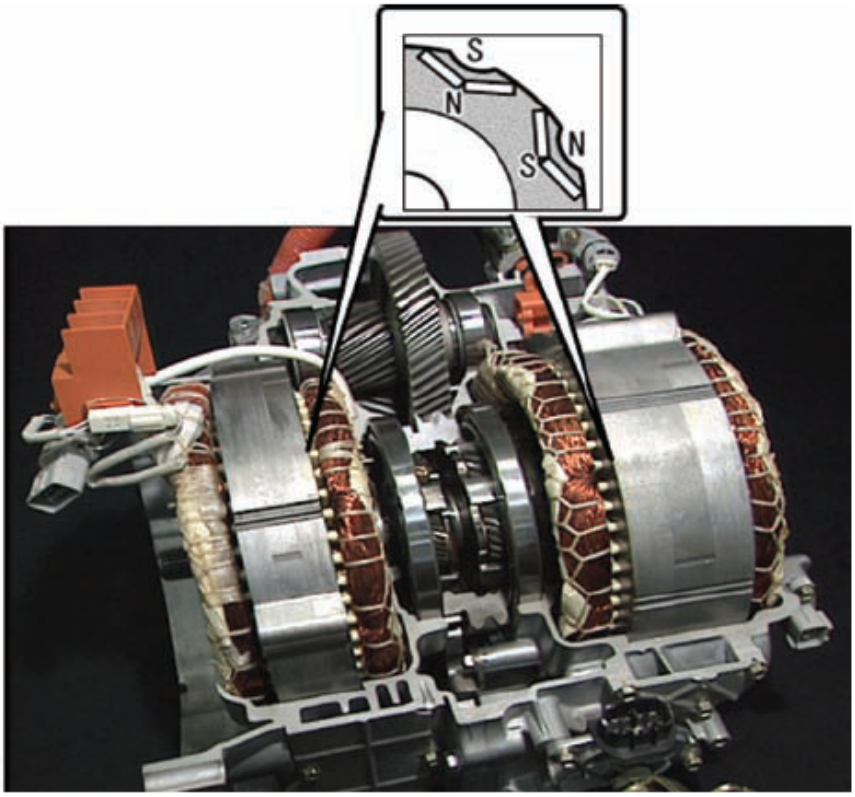

Figure 3.4: Prius generator and motor

According to Toyota, each hybrid motor uses $\sim$1.3 kg Nd-Dy-Fe magnets [73] and a good thermal stability at temperatures of $150 - 250\,^{\circ}\mathrm{C}$ should be attained for maximum acceleration with the best fuel economy. If the temperature exceeds this limit, the thermal demagnetization disorients the spins in the permanent magnet thus rendering it useless for this application.

Magnetic cooling can be utilized in hybrid motors to achieve the thermal stability for the reasons given above. The T_C can be tuned in such a way that the operating temperature is near $180\,^{\circ}\mathrm{C}$. With this requirement met, not only maximum efficiency is achieved, self-regulated operation of the system is also possible. Besides, the magnetic field necessary for the operation can be supplied by the built-in permanent magnets of the hybrid motor.

The advantages listed so far are pertinent to the magnetocaloric cooling technology in gen-

eral. As for the magnetic materials that are going to be used in this technology, there is a little controversy among researchers. Some groups support the idea of using magnetic nanoparticles with a first order transition (see Sec. 1.2.1), others think that using materials with a second order transition is far more advantageous (see Sec. 1.2.2). While first order materials are preferred for their large entropy response over a narrow temperature range, second order materials are preferred for their broad entropy response with a relatively smaller magnitude. The materials investigated in this study are Fe-Ni based alloys with second order transformation kinetics. They offer benefits over other magnetic materials in that they have cheap raw materials costs and do not rely on the critical rare earth materials. Their magnetic properties can be tailored depending on the needs of each application which can lead to efficient and profitable use of thermodynamic cycles.

3.2 Biomedical Applications

When magnetic nanoparticles are exposed to an alternating current magnetic field, they dissipate heat through Néel and Brownian relaxations. The generated heat by the nanoparticles, having T_C within $40 - 50\,^{\circ}\mathrm{C}$, have been reported to destroy the cancer cells while not harming the healthy tissue [74]. This is mainly becuase of cancer cells being less resistant against thermal shocks. Hence hypothermia, which is a cancer treatment technique that is involved of heating of tumor regions upto $42 - 46\,^{\circ}\mathrm{C}$ for an extended period of time, is being investigated as an alternative to the conventional cancer treatments [75].

For this application, magnetic nanoparticles with small particle size need to have a high saturation flux and a high anisotropy energy. High saturation flux and high anisotropy is needed for maximizing the heat generated under AC field. Small particle size, as proven in the previous analysis, is needed for the formation of stable solutions and safely injecting the nanoparticles into the body.

An oxide layer on the particles is another necessity not only because it introduces an added anisotropy to the system, it prevents magnetic nanoparticles from reacting while in the body. In addition, an oxide layer aids in the suspension of the nanoparticles into the solution because of the

surface polarity that comes with it.

3.3 Hypothesis

As the review of magnetic refrigerants made it abundantly clear, the magnetocaloric research is shifting towards developing new materials design paradigms and high-performing magnetic refrigerants with minimum rare-earth content. This has been a critical issue since it was realized that little expertise in the rare-earth processing industry remained in the United States on account of China leading the market in the past 20 years [76]. It is also projected that as the demand for the rare-earth magnets remains at this level, the prices will soar by as much as 200 % in the coming years [77].

The general engineering objective of this research is to pioneer new compositions based on γ-FeNi nanostructures that will have attractive magnetocaloric applications thus eventually diminishing the dependence on rare-earth magnets in energy applications. The structure and magnetic properties of these alloys can also be tuned through controlling the oxidation kinetics during synthesis and composition choices. The ternary elements can be chosen in such a way that they not only stabilize the γ-phase but also bring the T_C to room temperature.

Furthermore, the magnetocaloric properties in these materials can be explained by a distributed exchange interaction model which leads to broader magnetic entropy curves and can give rise to larger refrigerant capacities. Nearly 100 K intervals spanning the freezing and boilings points of typical solvents can be achieved with these alloys thus making them promising for ferrofluidic applications.

4 Structure and Magnetocaloric Effect in γ-FeNi

Even though Fe-Ni system has been extensively studied in the last century, little is known about the metastable extension of the fcc gamma phase in the Fe-rich region. By extending the known T_C for the gamma phase in the nickel rich region to low nickel concentrations, T_C's near room temperature can be achieved (Fig. 4.1). In the Fe-rich region, FeNi alloys have two phases in their equilibrium state. Here, solid state quench, one of the techniques used to synthesize metastable structures (see Sec. 2.1), is utilized for retaining the high temperature fcc phase on cooling. In this technique, the idea is to cool the high temperature phase fast enough, ≈300 K/s, before the atoms reorient themselves in the matrix.

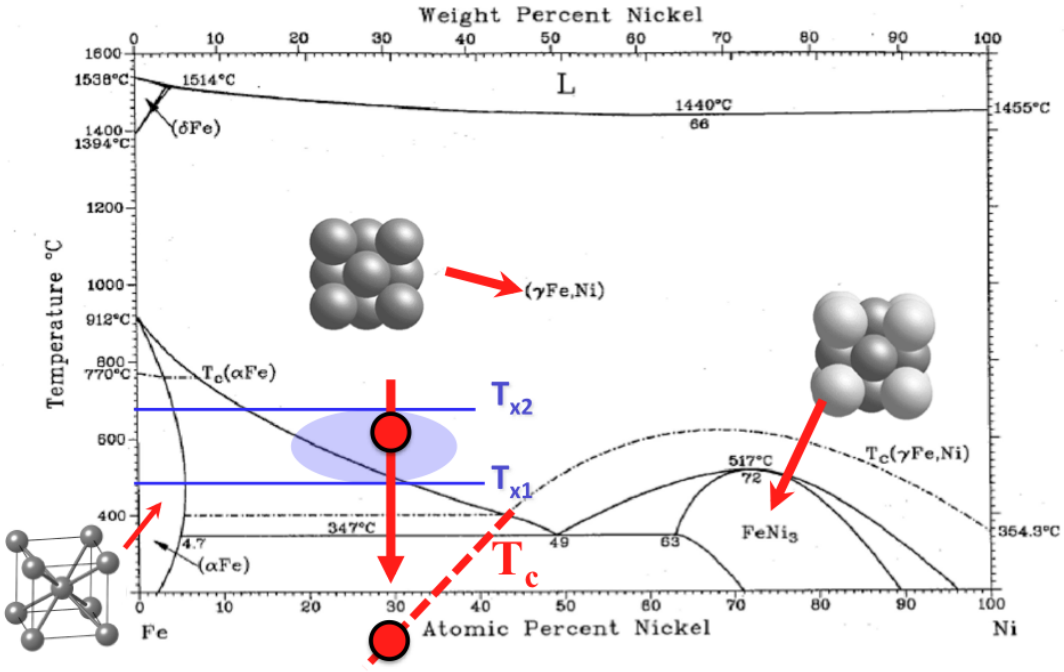

Figure 4.1: Fe-Ni phase diagram and extrapolated T_C line for the gamma phase

4.1 Stability of γ phase in Fe-Ni alloys

Melt spun $(Fe_{70}Ni_{30})_{88}Zr_7B_4Cu_1$

In this section, thermal stability of metastabe fcc γ-phase will be investigated. This is especially important as the stability of this phase is integral in determining the life time of an application.

First attempt was made by Ipus et. al., in a study in which they carried out a detailed structural and microstructural characterization for the Fe-Ni system [78]. This study confirmed the extension of the thermal stability of nanostructured γ-FeNi phase to room temperature. One aspect of this work in the context of nanocomposite magnets was in probing the phase evolution during primary nanocrystallization to model its role in determining structural disorder. In that study, high-temperature x-ray diffraction data were taken during nanocrystallization of $(Fe_{70}Ni_{30})_{88}Zr_7B_4Cu_1$ amorphous alloy ribbons (Fig. 4.2).

Temperature-dependent XRD patterns showed the amorphous phase to be thermally stable up to $\sim$673 K where the primary crystallization occurred. The product of the primary crystallization event was a body-centered cubic (bcc) FeNi phase. At increasing temperatures, the phase fraction of bcc FeNi phase was observed to increase and eventually transformed into face-centered cubic phase, which is in agreement with the Fe-Ni phase diagram and previous observations reported [79]. Moreover, XRD patterns and magnetic moment measurements on cooling showed the stability of γ-FeNi phase at room temperatures. These results confirm our claims on the stability of fcc phase at low temperatures which is mainly considered to be the result of slow diffusion kinetics of Ni in the FeNi system.

Mechanically alloyed (MA) $Fe_{70+x}Ni_{30-x}$

In the last section, the stability of gamma phase in $(Fe_{70}Ni_{30})_{88}Zr_7B_4Cu_1$ amorphous alloy was demonstrated with high temperature x-ray results. However, the effect of glass modifiers (Zr, B), or the nucleation agents (Cu) on the stability of γ phase were not discussed. To see if the stability of γ phase prevails without additions of these elements, series of binary $Fe_{100-x}Ni_x$ alloys

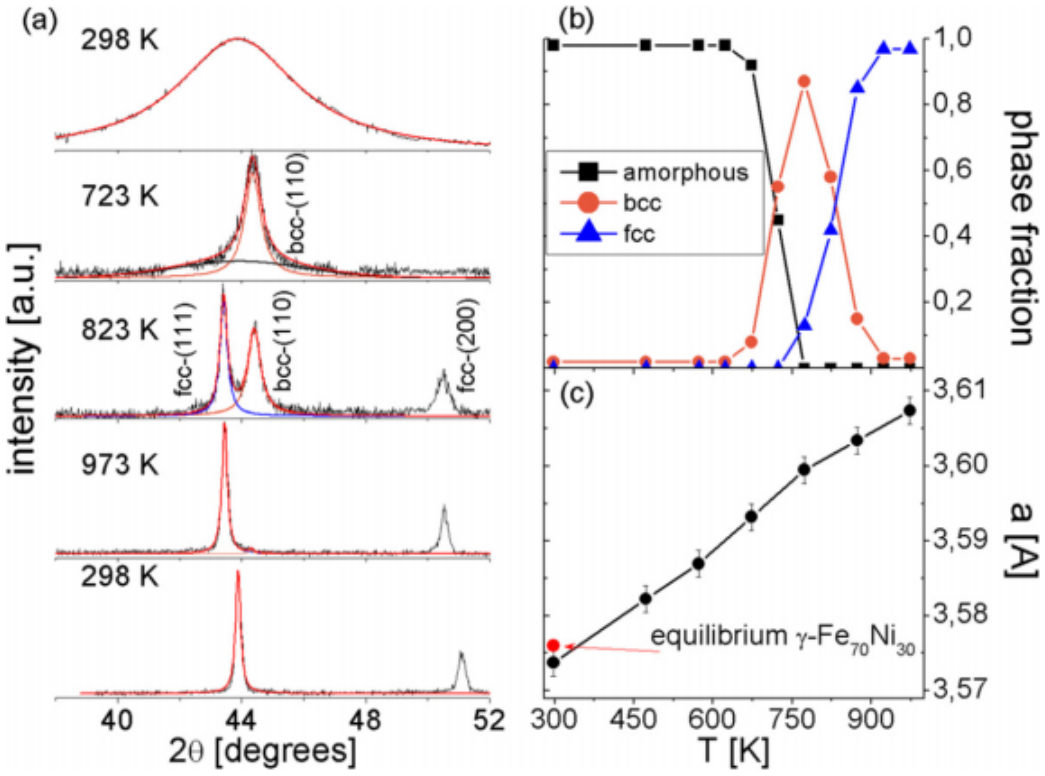

Figure 4.2: (a)In situ high-temperature x ray diffraction for some temperatures. (b) Temperature dependence of the phase fraction evolution. (c) Lattice parameter of the fcc-FeNi phase as a function of temperature.

were synthesized by mechanical alloying. A Vibrating Sample Magnetometer (VSM) was used to assess the stability of fcc phase. In the Fe-rich region, martensitic transformation seems to be the mechanism that can distort the stability of this phase on cooling. In Fe-Ni system, martensitic transformation takes place from austenite γ-FeNi to ferromagnetic α-FeNi phase. Since the magnetic moment of α-FeNi is higher than γ-FeNi, this transformation can readily be observed by VSM (Fig. 4.3a).

From Fig. 4.3b, the influence of non-equilibrium microstructure on the solid state transformations is evident after comparing the data for MA powders to those of equilibrium alloys. However, studying Fe-Ni system under equilibrium condition is difficult due to the slow diffusion rates at low temperatures. As cooling occurs, the diffusion coefficient of Ni decreases, for example, from 1.5×10^{-16} cm^{2}s^{-1} at 600 °C to 1×10^{-22} cm^{2}s^{-1} at 500 °C or in simple terms: at 300 °C, it takes

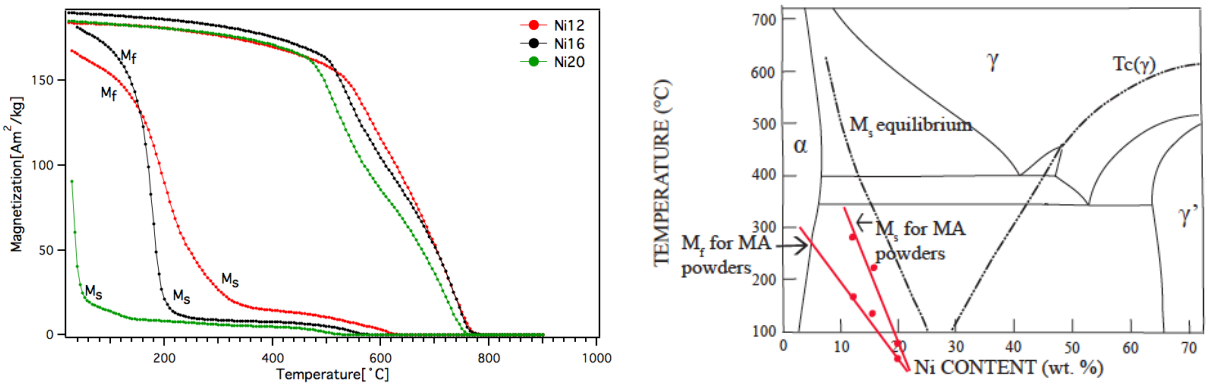

(a) (b)

Figure 4.3: (a) Thermomagnetic measurements of mechanically alloyed (MA) $Fe_{88-x}Ni_{12+x}$, (x =0,4,8) heated to maximum temperature of 900 °C. Martensite start and finish temperatures are designated as (M_s, M_f). (b) Fe-Ni phase diagram reproduced from [59]. Red lines represent M_s and M_f temperatures for the MA powders while the dashed line represents the trasnsformation temperature and Curie temperature for the equilibrium alloys.

more than 10^4 years for one atomic jump to occur [45]. Hence, the only feasible way of obtaining the equilibrium phase diagram for Fe-Ni is through the observations of meteorites.

Nevertheless, martensitic transformation can still take place in this binary regardless of the slow diffusion kinetics of Ni. In fact, it was considered to be the only type of transformation that the FeNi system can undergo on the Fe rich side at relatively low temperatures [59, 60]. Martensite is a term used to describe any diffusionless transformation product, in which from start to completion, only atomic movements that are less than one interatomic spacing take place [80]. While, many metallic compounds or minerals can be incited to undergo martensitic transformation provided that the optimum cooling or heating rates are achieved, it is the preferred mechanism on the Fe rich side of the FeNi binary alloys.

From Fig. 4.3(b), what happens to the γ-phase on the low Ni region (11 to 28 wt. $\%$ Ni) upon cooling is, supersaturated γ likes to transform to a two phase structure (α+γ) by nucleation and growth but can not overcome the nucleation barrier in Eq. 4.2. Put another way, the slow diffusion kinetics of Ni at low temperatures does not permit the formation of a nuclei greater than the critical size given in Eq. 4.3.

Barrier energy that must be overcome to form the new phase and the critical nuclei size are

obtained by differentiating Eq. 4.1 which is the free energy change associated with the nucleation process.

$$\Delta G = -\frac{4}{3}\pi r^3(\Delta G_v - \Delta G_s) + 4\pi r^2\gamma \tag{4.1}$$

$$\Delta G^* = \frac{16\pi\gamma^3}{3(\Delta G_v - \Delta G_s)^2} \tag{4.2}$$

$$r^* = \frac{2\gamma}{(\Delta G_v - \Delta G_s)} \tag{4.3}$$

In Fig. 4.3(b) the transformation temperatures for MA Fe-Ni are plotted against the Ni content. In addition, the respective data for the equilibrium condition is drawn as dashed line. The data for the martensite transformation temperatures differ significantly from those for equilibrium alloys. Not only the martensitic transformation is hindered for the powders synthesized through MA, it occurs over a wide temperature range. These differences can be linked to the rapid cooling rate as opposed to the equilibrium cooling rate and the higher defect density of mechanically alloyed powders introduced during synthesis. The thermomagnetic experiments on $Fe_{88-x}Ni_{12+x}$, (x =0,4,8) alloys revealed that the γ phase is not stable as martensitic transformations took place for all three compositions (Fig. 4.3(a)). However, the martensitic transformation was not observed for the $Fe_{76}Ni_{24}$ alloy mainly because of the increased Ni content which stabilizes the γ phase. The relatively low magnetic moment (from γ phase) on cooling in Fig. 4.4(a) and the results of XRD in Fig. 4.4(b) corraborates this conclusion. Put another way, from Fig. 4.4(b) the structure of the as milled powder is BCC which transforms into FCC upon heating and FCC phase remains to be the stable phase on cooling.

To sum up, the martensitic transformation was suppressed for the MA samples as compared with the equilibrium transformation kinetics due to the extensive refinement of the microstructure,

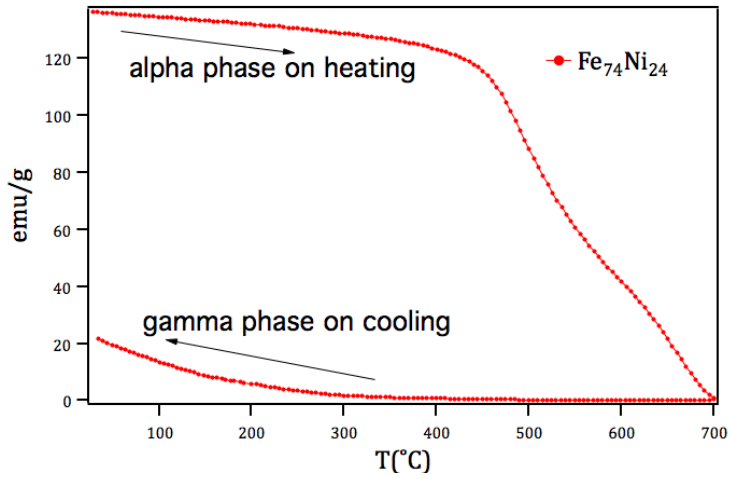

(a)

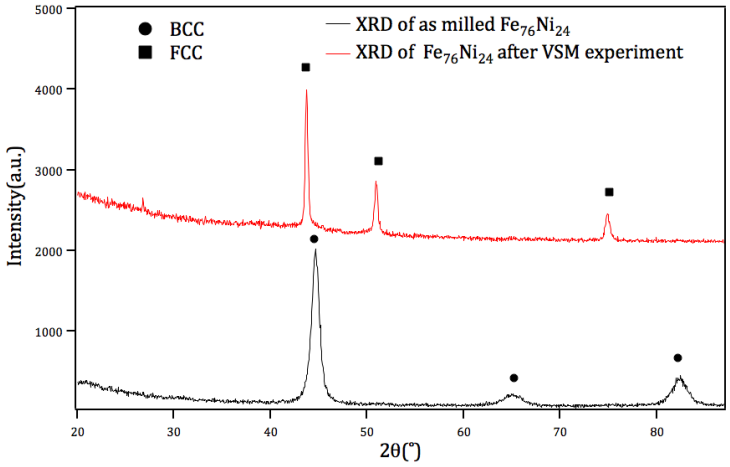

(b)

Figure 4.4: (a) Thermomagnetic measurements of mechanically alloyed (MA) $Fe_{76}Ni_{24}$ powders heated to maximum temperature of 700 °C. (b) X-ray results of as MA powders showing the existence of α phase which is transformed into the γ phase after 700 °C treatment.

added defect denstiy introduced during synthesis and rapid cooling rates. This led to the existence of paramagnetic fcc Fe-Ni alloys at room temperature for the compositions within ∼24-27 at. %Ni. The concentrations that are of interest for the magnetocaloric applications are around ∼30 at. %Ni. Around this concentration, not only γ phase has a relatively larger magnetic moment, its T_C is near room temperature. Besides, the life time of an application could be expected to be long for the alloys with Ni content more than 24 % as the experimental results proved the stability of γ phase.

4.2 Tuning the Curie Temperature in γ-FeNi Nanoparticles for Magnetocaloric Applications by Controlling the Oxidation Kinetics

4.2.1 Oxidation During Mechanical Alloying

During mechanical alloying, heat is generated due to the transferred kinetic energy from the grinding medium, the presence of an exothermic reaction and the transferred energy from the motor and the bearings. The increase in temperature can induce the oxidation in nanostructured materials. In this section, a novel method for tuning the T_C of γ-FeNi nanoparticles by controlling the oxidation during synthesis will be discussed.

In addition, we propose nanostructured γ-FeNi as promising magnetocaloric refrigerants near room temperature. The significance of nanoparticles is that the magnetic entropy peak is spread over a larger temperature span which gives rise to an enhanced refrigeration capacity (RC) [39]. By controlling the growth of the oxide layer on the nanoparticle, the goal is to utilize the surface spin disorder in the core-shell nanoparticles which would result in a larger MCE [81]. Previous work on controlling oxidation kinetics and interfaces in the FeCo system for RF applications inspired us to tune the T_C of γ-FeNi metastable phase with similar processes. Oxidation studies on Fe-Co system showed that, the oxidation of nanoparticles led to a faceted metal core with an oxide layer having epitaxial relationships with the core as in Fig. 4.5 [82].

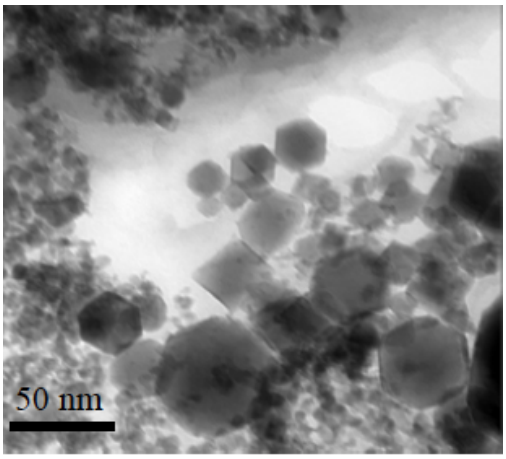

Figure 4.5: Faceted magnetic nanoparticles with oxide layers. Oxide layers appear darker in the micrograph. [after [82]]

The oxidation is mediated through metal cations that diffuse out of the core with oxidation at the gas-oxide interface. The metal cations that diffuse out of the core exchange places with vacancies. Therefore the kinetic barrier to the vacancy formation of each metal species determines the type of oxide that will dominate. Strain and interfacial energies also need to be taken into account as studies showed that they promote preferential nucleation of bcc phase [83]. In the Fe-Co system, Fe was found to oxidize more than Co and the oxidation became perceptible in 2 hours at $300\,^{\circ}\mathrm{C}$ heat treament [84]. For the particles synthesized via Spex mill, the temperature rise for the Fe-1.2wt$\%$C system has been recorded $300\,^{\circ}\mathrm{C}$ [65], while it is $180\,^{\circ}\mathrm{C}$ for the Ni-Zr binary system [66]. The temperature rise in FeNi system during milling was not reported in the literature. Therefore, to a good approximation, the temperature rise in Fe-Ni system will be on the same order of magnitude with those in Ni-Zr and Fe-1.2wt$\%$C systems.

4.2.1.1 Experimental Procedure

$Fe_{70}Ni_{30}$ and $Fe_{72}Ni_{28}$ alloys were produced by ball milling in a shaker mill (Spex 8000D) from elemental Fe (particle size-125 mesh), Ni (particle size-100 mesh) powders obtained from Alfa Aesar with 99.9 $\%$. The mill was operated under Ar with an initial powder mass of 8 g and a ball to powder ratio of 10:1. After selected milling times as mechanically alloyed powder samples were taken out from the hardened steel vials to characterize crystal structure by x-ray diffraction using Cu Kα radiation in a XPert PRO MPD diffractometer. In order to obtain a material with a single γ-FeNi phase, as milled $Fe_{70}Ni_{30}$ and $Fe_{72}Ni_{28}$ powders were subsequently sealed in a quartz crucible with Ar atmosphere and annealed in the γ-phase region, $700\,^{\circ}\mathrm{C}$ and quenched in water to stabilize the metastable γ-FeNi phase. Magnetic properties of the γ-FeNi phase were studied using a Lakeshore 7407 vibrating sample magnetometer using a maximum applied field of 0.55 T at constant temperatures in the range of room temperature to 523 K. The magnetic entropy change due to the application of a magnetic field has been calculated using a numerical approximation to

the equation;

$$\Delta S_M = \int_0^{H_{max}} \left(\frac{\partial M}{\partial T}\right)_H dH \tag{4.4}$$

where ΔS_M is the magnetic entropy change, M is the magnetization, and T is the temperature. The partial derivative is replaced by finite differences and the integration is performed numerically from zero to the maximum value of the applied magnetic field.

In this study, RC_{FWHM}, defined as the product of the peak entropy change times the full width at half maximum (FWHM) of the peak ΔT,

$$RC_{FWHM} = |\Delta S_M^{pk}|\Delta T \tag{4.5}$$

was used as a figure of merit. For materials that didn't cover sufficient area around the peak e.g. $Fe_{72}Ni_{28}$, RC_{FWHM} was estimated by extrapolating the experimental data to the temperatures required for this calculation.

4.2.1.2 Results and Discussion

Nature of Phase Transition

To assess the nature of magnetic phase transitions for the alloys synthesized in this study, Arrott plots are generated and displayed in Fig. 4.6(a). A commercially available ASTM A 753 08 alloy with composition $Fe_{55}Ni_{45}$ produced via conventional metallurgical techniques (i.e., cold drawing of molten ingot) are presented for comparison in Fig. 4.6(b) as well. According to Banerjee criterion [85], the negative slope in $(H/M)^{0.75}$ vs $M^{2.5}$ plots corresponds to a first order transition while the positive slope is a sign of a second order transition. In light of this criterion, both alloys in Fig. 4.6 clearly display second order transformation kinetics.

The idea of plotting $(H/M)^{0.75}$ vs $M^{2.5}$ originates from the Arrott-Noakes equation (Eq. 1.7) that I introduced in the beginning where the exponents 0.75, 2.5 are $1/\gamma$ and $1/\beta$ respectively.

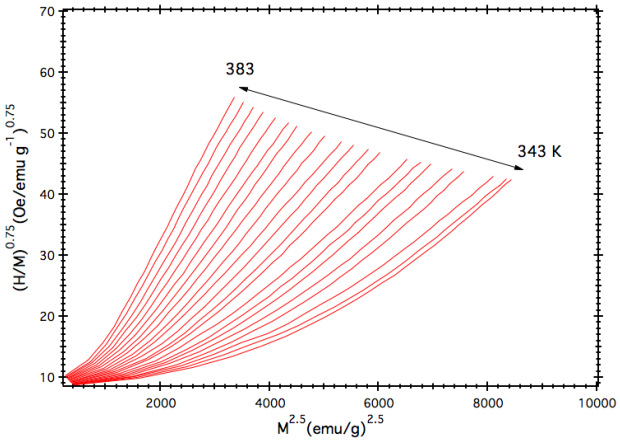

(a)

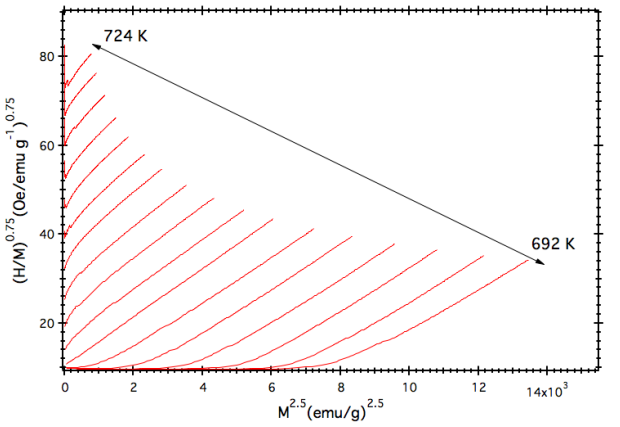

(b)

Figure 4.6: Arrott plots for various temperatures around T_C for samples (a) $Fe_{70}Ni_{30}$ synthesized via mechanical alloying for 30 hrs ($T_C \approx 360$K) (b) $Fe_{55}Ni_{45}$ synthesized via cold rolling ($T_C \approx 707$ K)

According to the predictions of the Arrott-Noakes model, the lines of $(H/M)^{0.75}$ vs $M^{2.5}$ plot should be parallel and spaced linearly in temperature in the neighborhood of T_C [9], as in the case of polycrystalline $Fe_{55}Ni_{45}$ in Fig. 4.6(b). The results of polycrystalline $Fe_{55}Ni_{45}$ agree well with the predictions of the model at high fields but not so well at low fields. The deviation from the model is more pronounced below T_C (≈ 707 K) and it can be attributed to the magnetocrystalline anisotropy arising from the antisymmetric exchange interactions and pinned magnetic domains near lattice defects [9].

As for the ball milled powders of $Fe_{70}Ni_{30}$, the deviation from the model becomes more prominent as the isotherms in Fig. 4.6(a) show large curvature and do not change concavity below

the transition temperature ($\approx 360K$). Far from being evenly spaced, the isotherms cluster together revealing no information about the transition temperature in this case. This anomality was also observed in another study [86] by Lampen et. al., and it was related to the presence of short range ordering with distributed exchange interactions in the structure.

Conversely, the agreement between the model and the experimental data is mainly due to the presence of longe range order in the polycrystalline $Fe_{55}Ni_{45}$ alloy.

XRD

Fig. 4.7 presents x-ray diffraction patterns from powders of $Fe_{70}Ni_{30}$ and $Fe_{72}Ni_{28}$ alloys ball milled for 10, 30, 50 hrs and powders of these which were annealed in the γ-phase field followed by quenching. The diffraction patterns for 10 and 30 hrs milled $Fe_{70}Ni_{30}$ and $Fe_{72}Ni_{28}$ powders reveal both fcc and bcc phases and the fcc ratio is observed to increase with milling time for $Fe_{70}Ni_{30}$ while it is invariant for $Fe_{72}Ni_{28}$. While $Fe_{70}Ni_{30}$ exhibits only fcc peaks and additional oxide peaks that are indexed to FeO (wustite), $Fe_{72}Ni_{28}$ alloy is observed to retain both fcc and bcc phases after 50 hrs of milling. In addition to the wustite which is observed for the two compositions after solution annealing the 50 hrs milled alloys, the γ-stabilized $Fe_{70}Ni_{30}$ exhibits $NiFe_2O_4$ (NiFe oxide) peaks. The lattice parameter of the wustite was found to be a=4.290$\pm$003 Å which agrees well with the results from JCPDS index of wustite [87].

Even though the equilibrium phase diagram predicts the coexistence of bcc and fcc at low temperatures [58], the supersaturation of fcc γ-FeNi is obvious from 50 hrs ball milled powder of $Fe_{70}Ni_{30}$. The two phase region is reported to narrow with milling intensity which is caused by the temperature dependence of the metastable equilibria [57]. Here, we observe the narrowing of the two-phase field with milling time which induces the additional dissolution of Fe in fcc FeNi.

Fig. 4.8 shows lattice constants for fcc and bcc structures for the two compositions and the phase fractions of each phase in addition to the oxide. Lattice parameters found in this study agrees well with the reported results [88]. From Fig. 4.8a), the lattice parameter of the fcc phase is observed to increase with milling time while that of bcc remains invariant. Fig. 4.8b) shows that the ratio of fcc phase increases to that of bcc in $Fe_{70}Ni_{30}$ while it remains the same in $Fe_{72}Ni_{28}$.

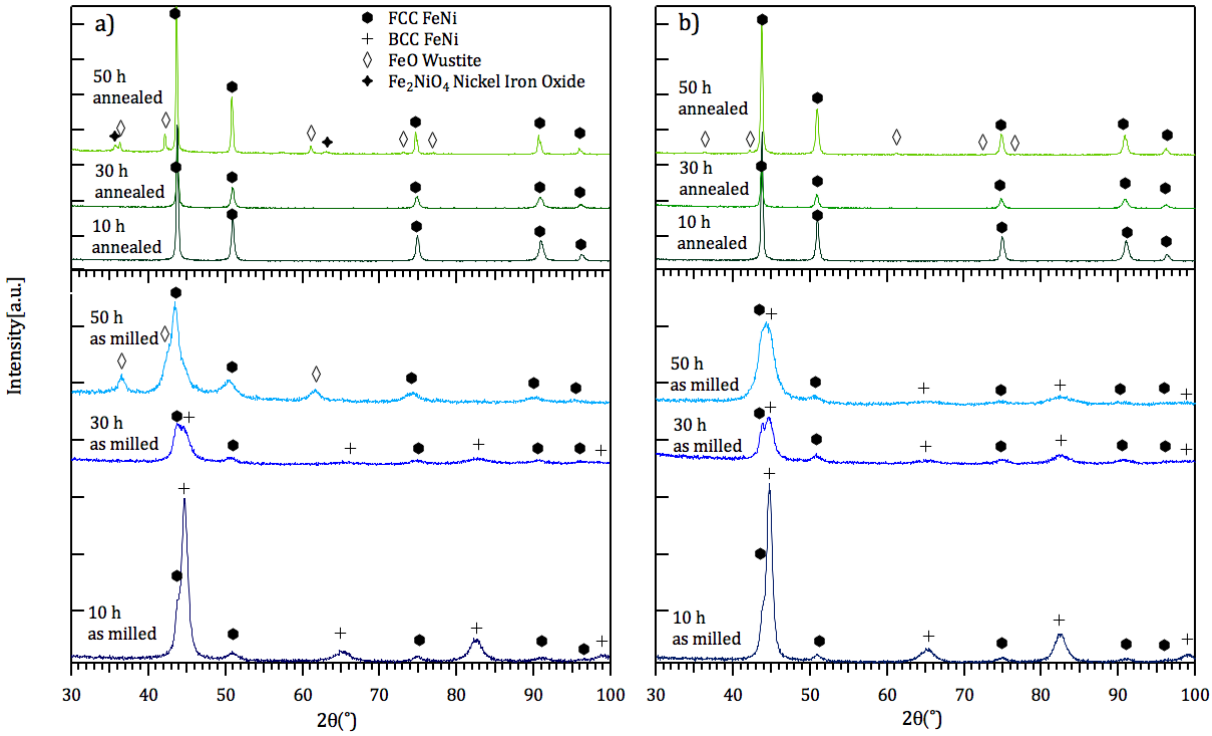

Figure 4.7: X-ray diffraction patterns of 10, 30, 50 hours as-milled powders and solution annealed powders at 700 °C for 1h followed by quenching for a)$Fe_{70}Ni_{30}$, b) $Fe_{72}Ni_{28}$

This is ascribed to the presence of additional Ni in $Fe_{70}Ni_{30}$ as it stabilizes the fcc structure.

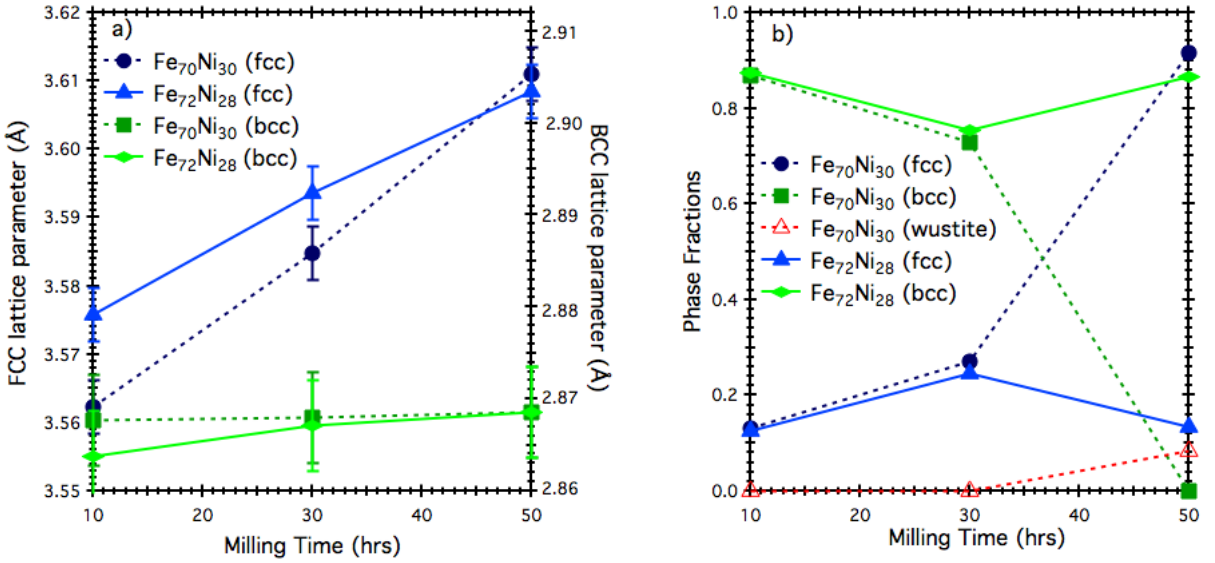

Figure 4.8: a) Lattice parameters of bcc and fcc phases in as-milled $Fe_{70}Ni_{30}$ and $Fe_{72}Ni_{28}$ against milling time. b) Fractions of bcc and fcc phases and oxide in as-milled $Fe_{70}Ni_{30}$ and $Fe_{72}Ni_{28}$ alloys against milling time determined by x-ray diffractometry.

As previously introduced, the heat generated due to grinding of steel balls against the powder leads to oxidation of particles as is seen in the x-ray diffraction patterns of 50 hrs as milled powder and γ-phase stabilized $Fe_{70}Ni_{30}$. However, the oxidation for the $Fe_{72}Ni_{28}$ took place during the annealing process. In the FeNi system there is a strong compositional dependence of the Curie temperature, T_C, on composition in the γ-phase [44]. Since wustite and nickel-iron oxide are rich in Fe, formation of these oxides depletes the Fe in the core which changes the core composition. This in turn changes the T_C of the system. Tuning the RC along with the T_C can be accomplished with the formation of an oxide layer. In tuning the RC, exchange coupling of the 2-phase core/shell structure is exploited. This is analogous to disorder induced broadening of the transition due to distributed exchange interactions [16].

In earlier studies on the FeNi binary system, Gorria et. al. also observed the increase in the T_C by means of mechanical alloying after a heat treatment at 1073 K. However, the increase in the T_C was ascribed to the introduction of microstrains during milling in that study [89]. They arrived at this conclusion based on the assumption that induced microstrain around Fe increases the interatomic distance between Fe-Fe atoms which eventually enhances the ferromagnetic interactions due to the magnetoelastic coupling in the Invar compounds.

To evaluate the effect of microstrains on the T_C, Williamson-Hall plots were generated. Williamson and Hall proposed a method for deconvoluting contributions to the strain broadening by evaluating the peak width as a function of θ. This model originates from the observation that strained or imperfect crystals produce line broadening of a different sort than the broadening caused by small crystallites [67].

It is expressed as;

$$Bcos(\theta) = 2(\epsilon)sin(\theta) \tag{4.6}$$

where B is the full width at half maximum of the XRD peaks, ϵ is the internal microstrains and θ is the Bragg angle. According to this model, if strain is the only reason for broadening then Bcos(θ) is a linear function of sin(θ). Therefore, the larger the slope is, the more accumulated

microstrains there are in the structure. On the contrary, if strain is eliminated then Bcos(θ) is a constant for all peaks.

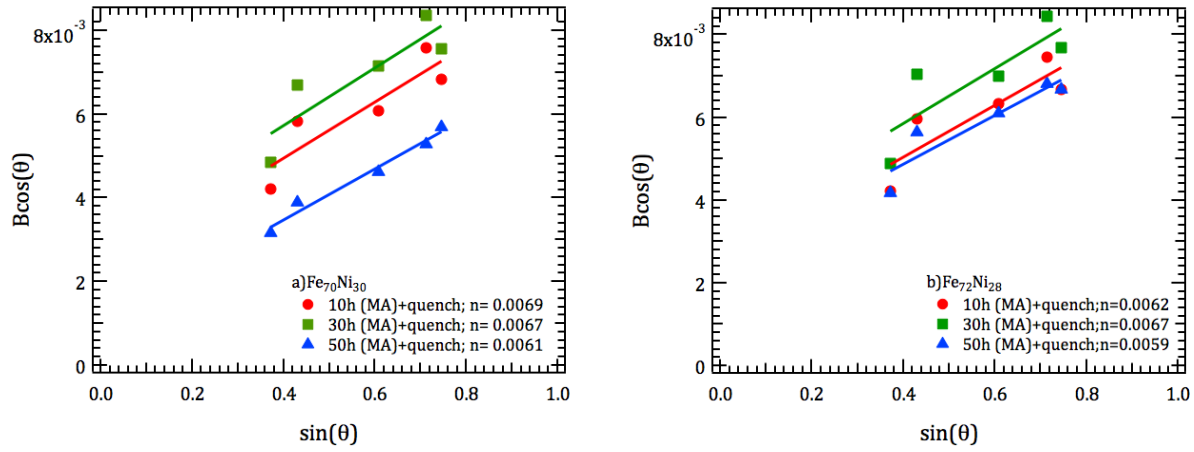

(a) (b)

Figure 4.9: Williamson-Hall plots of mechanically alloyed particles followed by solution annealing for the compositions (a) γ-$Fe_{70}Ni_{30}$ (b) γ-$Fe_{72}Ni_{28}$

From Fig. 4.9, the slope represented by n increases slightly after 30 hrs of milling as compared with 10 hrs milled powder and decreases after 50 hrs of milling for the two compositions. However, as shown in Fig 4.17 on page 73, the T_C of $Fe_{70}Ni_{30}$ and $Fe_{72}Ni_{28}$ increases systematically with milling time thus rendering the microstrain argument invalid for this study. Put another way, a direct correlation between the shift in T_C and the amount of strain in the microstructure is not observed which arises the need for new arguments to account for the change in T_C.

The average grain sizes were calculated by analyzing the width of the fcc(111) diffraction with the Scherrer equation:

$$L = \frac{0.9\lambda}{B(2\theta)cos\theta} \tag{4.7}$$

where B(2θ) is the full width at half maximum(in radians) of a Lorentzian function fit to the diffraction peak. This analysis was carried out for the solution annealed powders at $700\,^{\circ}\mathrm{C}$, as these particles had minimum strain in the microstructure thus making the particle size calculation more reliable. This method yields 43.7 nm $\pm$0.4 nm for the size of the crystals.

XRF

A major concern with mechanical alloying is the extent of contamination introduced during milling. The small size of the particles and a large surface area that comes with it are some of the factors that can induce contamination. In addition, the milling atmosphere, grinding medium and the purity of starting elements are equally important too. However, there are certain measures that one can take to minimize it.

One way of minimizing the contamination stemming from the grinding medium is to use the same material for the container as the powder being milled. Contamination could also occur when the container is not properly sealed which results in the leakage of the surrounding atmosphere into the medium. Therefore, it is vitally important to seal the grinding medium with a high purity argon atmosphere to ensure the processing of high-quality alloys. One should also keep in mind that cross contamination could occur if a container which was used previously is used in the subsequent run without properly cleaning it.

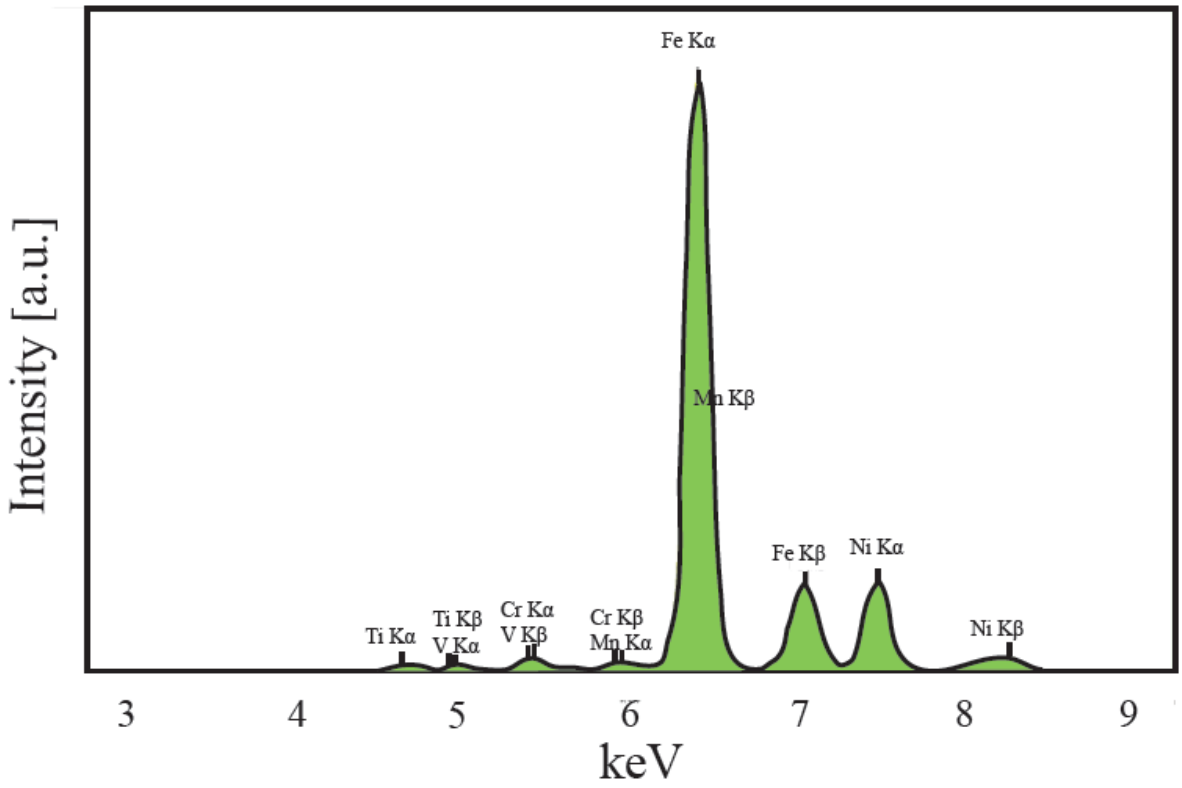

Figure 4.10: XRF data of $\gamma Fe_{70}Ni_{30}$ milled for 50 hrs.

To analyze the degree of contamination, XRF measurements were performed on the alloys of γ-$Fe_{70}Ni_{30}$ and γ-$Fe_{72}Ni_{28}$. As mentioned in the experimental section, mechanical alloying of powders took place in hardened steel vials. According to the data obtained from the manufacturer of the vials, while the major constituent element is Fe, trace amount of Cr, Mn, C and Si are also present in the vials that were used [90]. Therefore, after operating the mill for a long period of time it is very likely to observe the presence of these minor elements in the synthesized alloys as well. The XRF peak profile is given in Fig. 4.10 for the γ-$Fe_{70}Ni_{30}$ alloy milled for 50 hrs. In addition to the major elements (Fe and Ni), trace amount of elements such as Ti, V, Cr and Mn are also detected. While it is possible that Mn and Cr are introduced to the system from the hardened steel vials, the presence of contaminants such as Ti and V could be due to the poor handling and cleaning of the vial from the previous run.

The amount of each element is calculated from the peak intensity and its variation with milling time is given in Fig. 4.11. This plot shows that each element is between 0.1-0.2 at. % in the overall composition while Cr is nearly 1 at. % in the γ-$Fe_{70}Ni_{30}$ alloy after 50 hours of milling. In the remainder of this section, the influence of these elements on the magnetic properties of γ-FeNi alloy will be discussed. Conclusions of this section will also be tied to our general hypothesis of tuning the magnetic properties of the γ-FeNi by preferential oxidation of Fe.

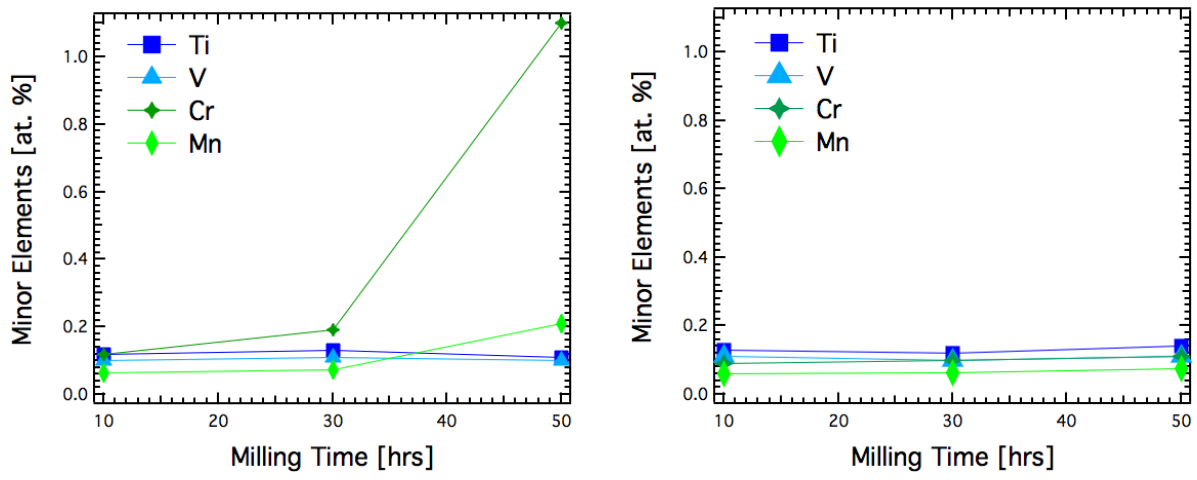

Figure 4.11: Amount of minor elements as a function of milling time for (a) γ-$Fe_{70}Ni_{30}$ (b) γ-$Fe_{72}Ni_{28}$

Bethe-Slater curve which shows the variation of the exchange integral, J_{ex}, with the radius of its 3d shell of electrons, r_a/r_{3d}, needs to be taken into account when assessing the effect of anti-ferromagnetic elements such as Mn and Cr on the magnetic properties of γ-FeNi (Fig. 4.12). This curve is a quantum mechanical interpretation of the exchange force and led to many conclusions of great value in magnetism. According to the model, the exchange integral is positive for ferromagnetic materials as in Fe, Co and Ni. However, as the ratio r_a/r_{3d} decreases to a certain value the 3d electrons will be close enough that their spins favor antiparallel alignment as in antiferromagnetic materials e.g., Mn and Cr.

The Bethe Slater curve is used to estimate the J_{ex} based on the composition of an alloy as it is shown for the pure γ-$Fe_{70}Ni_{30}$ in Fig. 4.12. The XRF data showed that the alloy had trace amount of Mn and Cr. Any additions of these antiferromagnetic elements will lower the J_{ex} and weaken the ferromagnetic response of the alloy. This will eventually decrease the T_C of the alloy according to the following approximate form of relation that shows the dependence of T_C on J_{ex} (Eq. 4.8).

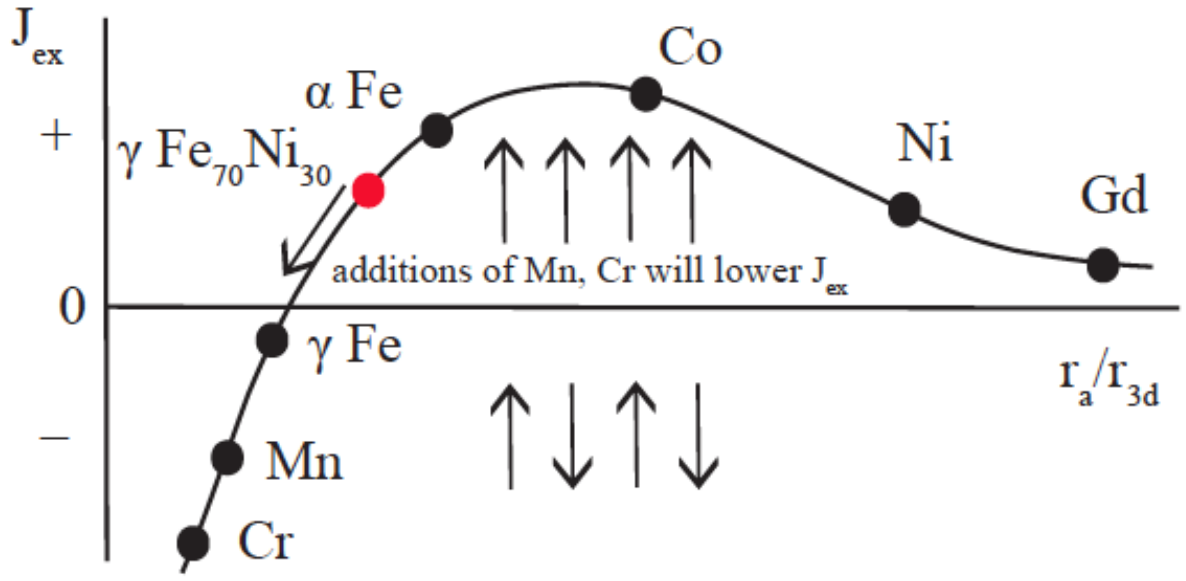

Figure 4.12: Bethe-Slater curve (schematic).

$$J_{ex} = \frac{3kT_C}{2zS(S+1)} \tag{4.8}$$

where k is the Boltzmann constant, Z is the coordination number and S is the orbital spin number.

As for the Vanadium and Titanium, the structure and magnetic properties of Fe-Ni alloys containing these elements have not been extensively studied. However, there have been a few studies claiming the suppression of T_C by small additions of V or Ti into the Fe-Ni matrix [91, 92].

In brief, XRF results showed that there are trace amount of Cr, Mn, Ti and V due to the contamination during milling. However, literature findings and theory on the exchange interactions suggest that these elements decrease the T_C of the FeNi binary system rather than increasing it. This is why, the increase in the Curie temperature of the γ-FeNi with milling time can not be explained by the contamination argument either.

SEM

The size and shape of the particles may be determined accurately using direct method of Scanning Electron Microscopy (SEM) for relatively coarse powders. Fig. 4.13 shows the SEM micrographs of $Fe_{72}Ni_{28}$ at different magnifications. The particle size is around $10\mu m \pm 5\mu m$ which is much larger than the particle size estimated from the XRD peaks.

Here, it is important to keep in mind that the particles are agglomerated during mechanical alloying which leads to results that are difficult to interpret. A powder particle may consist of several individual particles and an individual particle may contain a number of crystallites defined as coherently diffracting domains [54]. Therefore, while macroscopic examination gives the particle size as in Fig. 4.13 , diffraction techniques gives the crystallite size.

Magnetocaloric Properties

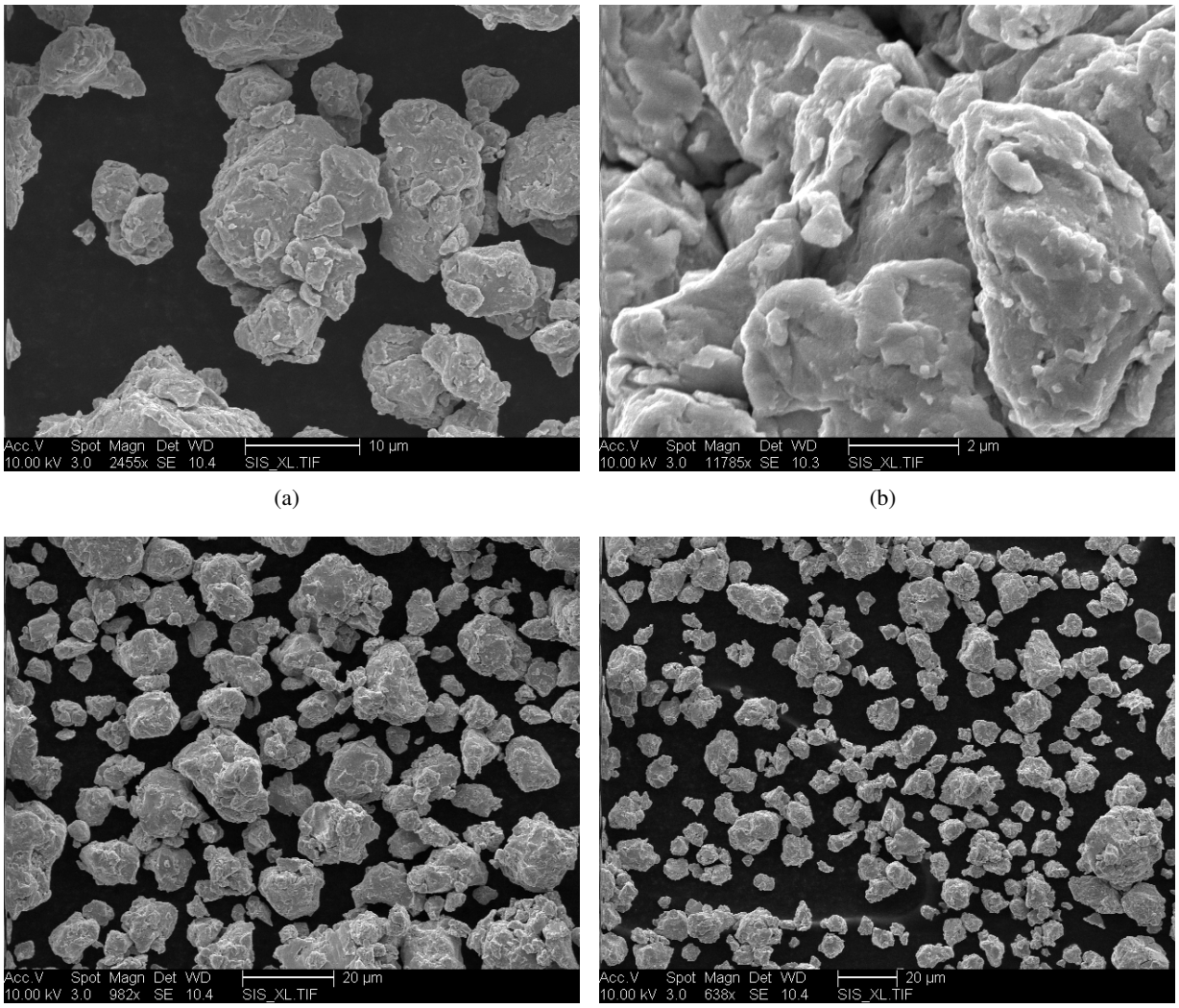

(a) (b)

(c) (d)

Figure 4.13: SEM micrographs of Fe28% Ni at different magnifications

Isothermal magnetization curves for a maximum applied field of 0.55 T were taken every 10 K in a temperature range of room temperature to 553 K (Fig. 4.14(a)).

From Fig. 4.14(a), a continuous decrease in magnetization as the temperature increases is evident and it is due to the ferromagnetic to paramagnetic transformation.

Fig. 4.14(b) shows the magnetization as a function of temperature for the quenched powder at a field of 0.55 T. The transition from ferromagnetic to paramagnetic phase has been calculated to be $\sim$ 360K for the γ-phase $Fe_{70}Ni_{30}$ powders that are milled for 30 hours. This value was estimated using the inflection point method and is in good agreement with the estimated values

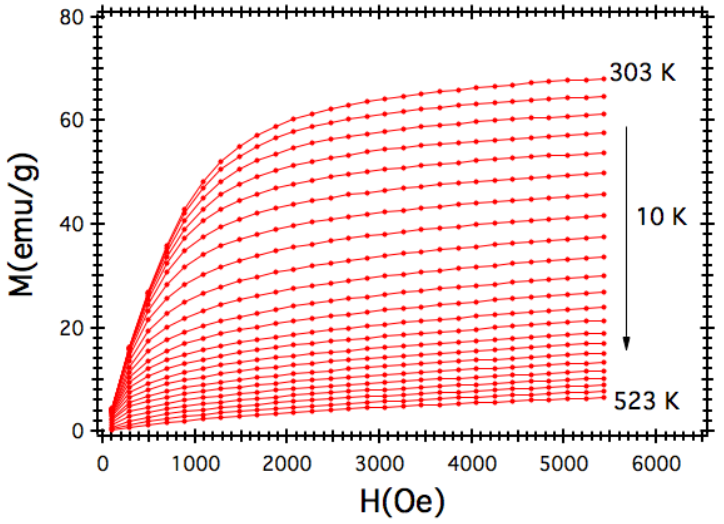

(a)

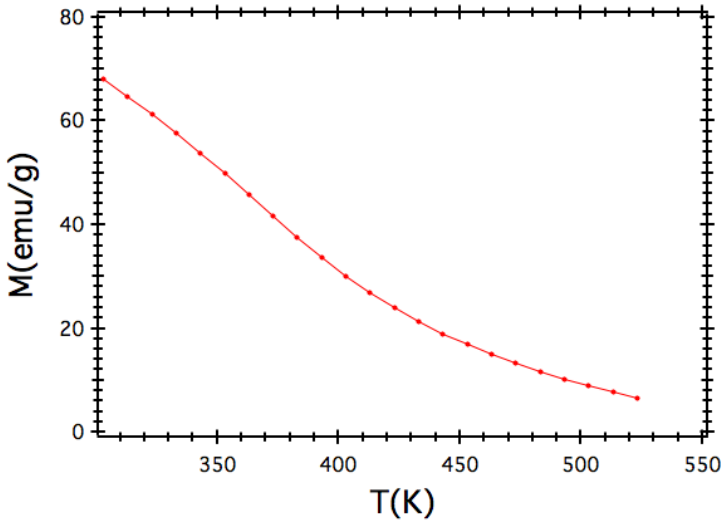

(b)

Figure 4.14: (a) Magnetization isotherm curves obtained from room temperature to 533 K for a maximum applied field of 0.55 T. (b) Temperature dependence of spontaneous magnetization for quenched sample for an applied field of 0.55 T.

obtained from the compositional dependence of T_C with Ni content in the γ-phase of the Fe-Ni equilibrium phase diagram [79]. The presence of a magnetic moment at high temperatures can be ascribed to the trace amount of α-phase in the system as it preserves its ferromagnetic properties at elevated temperatures.

In order to evaluate the magnetic entropy change, ΔS_M, a numerical approximation to equation 4.4 is needed. In the case of magnetization measurements at discrete field and temperature

intervals, ΔS_M can be approximated by;

$$|\Delta S_M| = \sum_i \frac{M_i - M_{i+1}}{T_{i+1} - T_i} \Delta H_i \tag{4.9}$$

Where M_i and M_{i+1} are the experimental magnetization values at temperatures T_i and T_{i+1} respectively. Using the approximation given by equation 4.9, ΔS_M as a function of temperature for each sample can be computed numerically by first differentiating the magnetization data, M, with respect to temperature, and then integrating the resulting derivatives from zero field to the maximum field achieved H_{max}.

Following this procedure, the magnetic entropy was calculated for a range of fields from 100 Oe to 5500 Oe in Fig. 4.15.

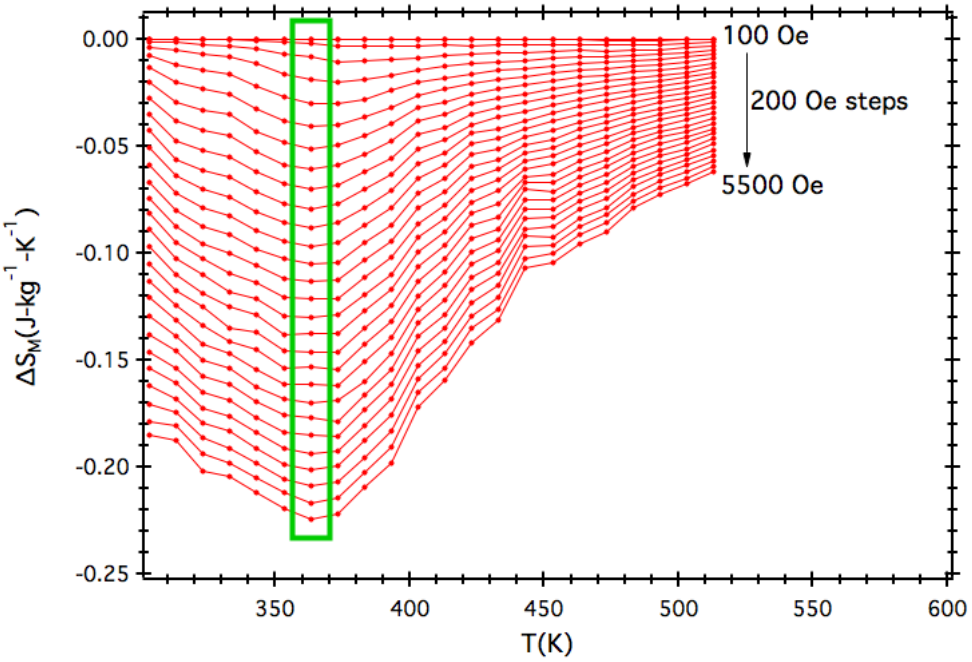

Figure 4.15: Temperature dependence of the magnetic entropy change curves of a $Fe_{70}Ni_{30}$ alloy milled for 30 hours for maximum applied fields ranging from 100 Oe up to 5500 Oe

The temperature where the maximum entropy is observed, T_{pk} in Fig. 4.15 is ~360 K which coincides with the T_C of this alloy. This is an expected result for materials undergoing a second order transition [93].

One point that needs careful consideration is the relationship between T_{pk} and T_C and their

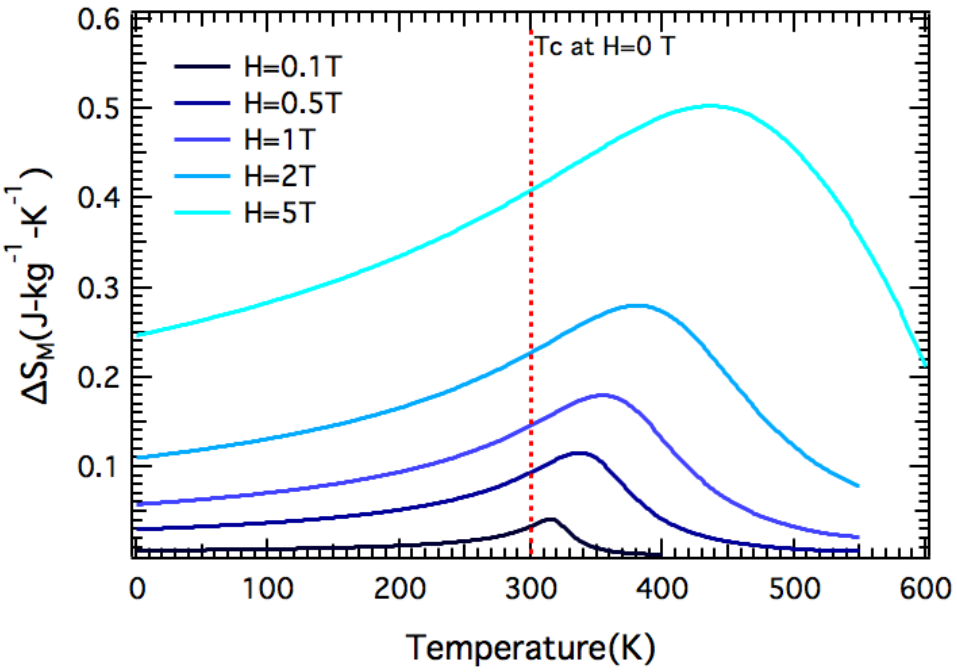

Figure 4.16: Temperature dependence of the magnetic entropy change for maximum applied fields of 0.1, 0.5, 1, 2, 5 T. The dashed line at 300 K designates the Curie temperature.

dependence on field for materials undergoing second order transition. First, T_{pk} and T_C was assumed to occur at the same temperature. However, Franco et. al. showed that T_{pk} increases with field following a power law $H^{1/\Delta}$ with (Δ=$\beta + \gamma$) [94]. Here β and γ are critical exponents describing the temperature dependence of magnetization and inverse susceptibility respectively as defined in Eq. 1.7.

To support the experimental findings, theoretical magnetic entropy curves (Fig. 4.16) can be plotted by solving the Arrott-Noakes equation (Eq. 1.7) with critical exponent values (γ=1.35, β=0.39) that are typical for an Fe-based amorphous alloy. These plots were generated using MATHEMATICA@TM .

At high fields, the shift in T_{pk} in Fig. 4.15 is what one would expect for a material undergoing second order phase transition. However, the curves don't seem to follow the same trend at lower fields, i.e. slightly shifting to lower temperatures with field. In one study, this was ascribed to the compositional inhomogeneities in the microstructure which yields a distribution of local Curie points [95]. Therefore, it is likely that the compositional inhomogeneties caused by mechanical

alloying is the reason for such a deviation from theory.

Following the same procedure used to obtain Fig. 4.15, the magnetic entropy change, ΔS_M, of $Fe_{70}Ni_{30}$ and $Fe_{72}Ni_{28}$ powders for different milling times at a maximum applied field of 0.55 T is calculated and presented in Fig. 4.17.

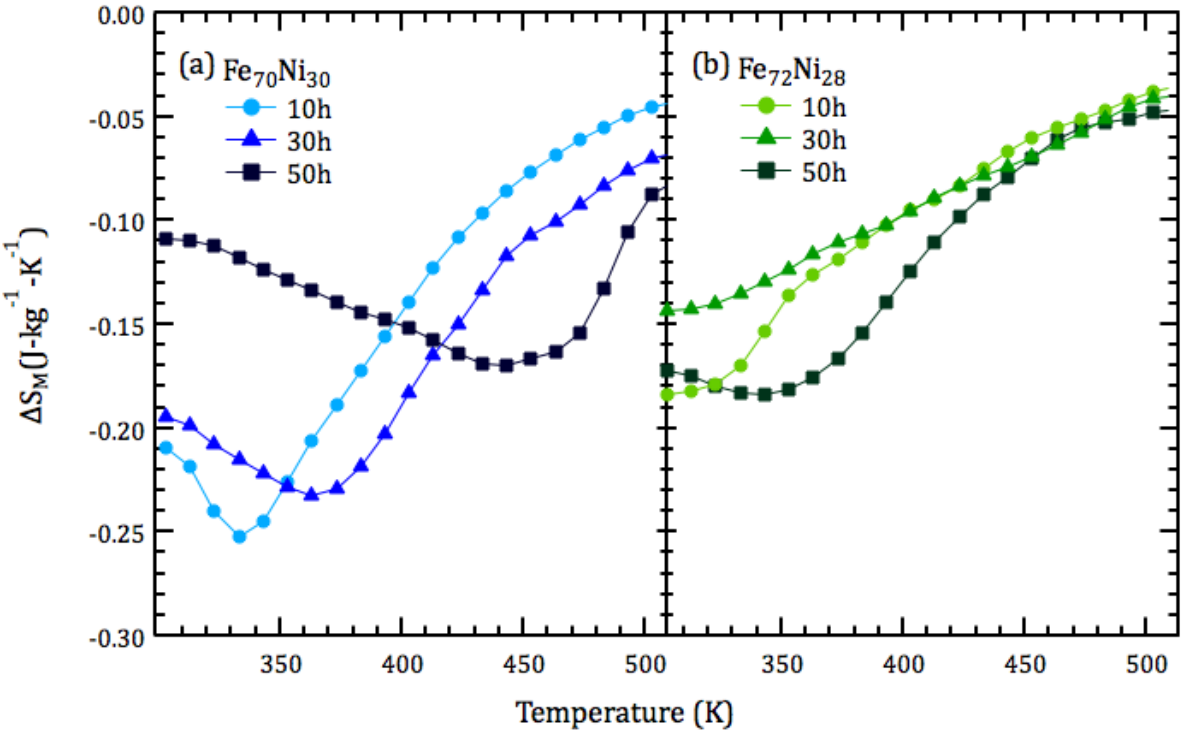

Figure 4.17: Temperature dependence of the magnetic entropy change, ΔS_M, corresponding to a magnetic field change ΔH_M=0.55 T for different milling times in the (a)annealed γ-$Fe_{70}Ni_{30}$, (b)annealed γ-$Fe_{72}Ni_{28}$

The maximum magnetic entropy change values observed for γ-$Fe_{70}Ni_{30}$ are 0.32, 0.22 and 0.17 $Jkg^{-1}K^{-1}$ for 10, 30 and 50 hrs of ball milling respectively. The peak entropy change temperatures are 333 K, 363 K and 443 K for the same composition for 10, 30 and 50 hrs milled powders respectively. From the Fe-Ni phase diagram [58] and the composition dependence of the Curie temperatures of each powder, the Fe content in the nanoparticles can be estimated. The Fe content is 71 at. % Fe after 10 hrs of milling and systematically decreases to 69 and 67 at. % Fe for 30 and 50 hrs of milling for the γ-$Fe_{70}Ni_{30}$. The maximum entropy change is 0.19 $Jkg^{-1}K^{-1}$ with a peak entropy change around 333 K for 50 hrs milled γ-$Fe_{72}Ni_{28}$ powder. Since the Curie temperatures of the 10 and 30 h milled γ-$Fe_{72}Ni_{28}$ powders were slightly below the room temperature, their peak

entropy and other magnetocaloric properties could not be assessed.

The ΔS_M can be expressed as a power law for materials with a second order phase transition [96].

$$\Delta S_M = AH^n \tag{4.10}$$

where A is a prefactor and n is the temperature dependence of the exponent characterizing the field dependence of ΔS_M. With this equation, ΔS_M and RC_{FWHM} can be extrapolated to higher fields, which is necessary for comparing the magnetocaloric response with other refrigerants.

RC_{FWHM} at 5 Tesla can be estimated in the same way as magnetic entropy by calculating the respective RC_{FWHM} values within the experimental range following the relationship in Eq. 4.11:

$$RC_{FWHM} = |\Delta S_M^{pk}|\Delta T \tag{4.11}$$

where $|\Delta S_M^{pk}|$ is the peak entropy values in the rectangle in Fig. 4.15 and ΔT is the temperature span at the half maximum of the peak entropy values. Following this procedure, RC_{FWHM} values are plotted against magnetic field for γ-$Fe_{70}Ni_{30}$ powders milled for 30 hours in Fig. 4.18. This method yields a value of 495 Jkg^{-1} when only the high field portion of the data is taken into account for fitting while a value of 470 Jkg^{-1} is obtained when all the data points are used. The former technique supposedly provides more accurate results since the RC_{FWHM} is a straight line at high fields on account of the alloy being magnetically saturated.

When the RC_{FWHM} value was extrapolated for the γ-$Fe_{72}Ni_{28}$ powders, it yields 250 Jkg^{-1}. The reduction in the RC_{FWHM} is a result of the decrease in magnetic moment at this concentration.

In Fe-Ni system, the saturation magnetization of Fe, M_s, is known to decrease with small additions of Ni attaining its minimum at 30% Ni. The experimental saturation magnetization values obtained against Ni content is given in Fig. 4.19(b) together with the Slater Pauling curve which is a plot of stoichiometric mean atomic moment as a function of electrons filling the d-orbitals of transition metal binary alloys. According to the Slater Pauling curve, the initial additions of Ni to

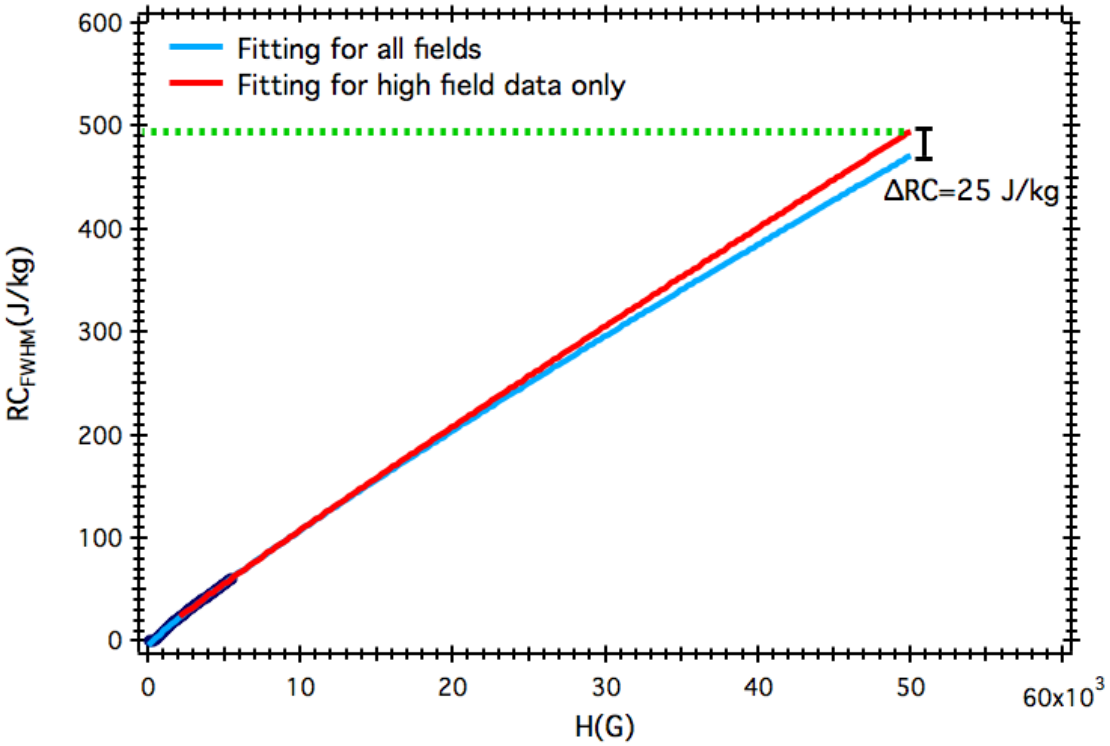

Figure 4.18: Field dependence of the refrigeration capacity, RC_{FWHM}. Thick black line corresponds to the experimental data. Blue line represents the extrapolated values from the power law fitted using all field data, red line represents the exptrapolated valies from the power law fitted using only high field data. RC_{FWHM} corresponds to 470 Jkg^{-1} for the former and 495 Jkg^{-1} for the latter at 5 T for the γ-$Fe_{70}Ni_{30}$ alloy milled for 30 hours.

bcc Fe slightly increase the average magnetic moment of the alloy followed by a linear decrease. The results shown in Fig. 4.19(b) agree with the theory up until about 28% Ni. This slight shift in Ni content at which the minimum occurs can be explained by the milling intensity used in this study as it has been proven with earlier studies that milling intensity shifts the concentration where the deviation from Slater Pauling curve takes place [57].

The peak magnetic entropy change and RC values of the studied alloys with their extrapolations to 5 T are presented in Table 4.1. Other promising magnetocaloric materials reviewed in this study are also listed for comparison. From Table 4.1, $Gd_5Ge_{1.9}Si_2Fe_{0.1}$ and $Fe_{88}Zr_7B_4Cu_1$ have slightly higher refrigeration capacities than γ-$Fe_{70}Ni_{30}$ milled for 30 hours. However, when each alloy is considered in terms of their cost, FeNi system clearly is the most economically advantageous refrigerant with respectable magnetocaloric properties, which will facilitate industrial scale

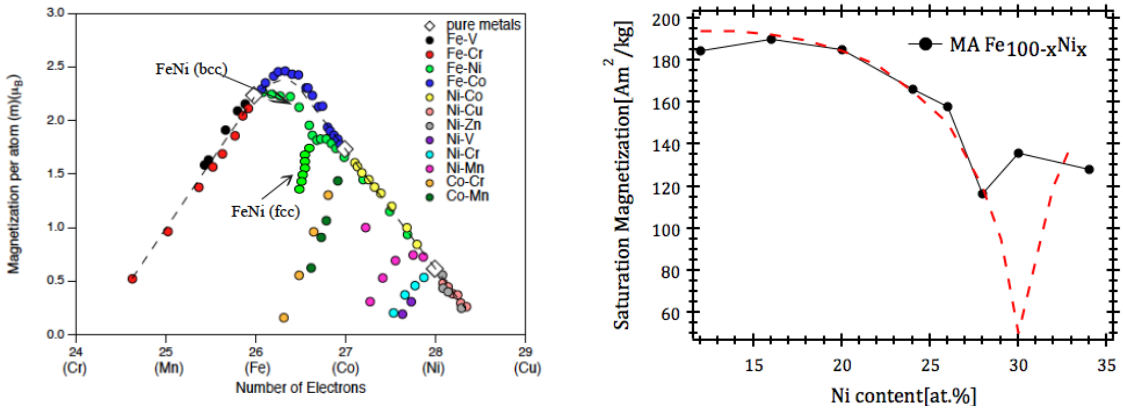

(a) (b)

Figure 4.19: (a) Slater Pauling curve (b)Saturation magnetization as a function of Ni content for mechanically alloyed $Fe_{100-x}Ni_x$(this study). The dashed line represents data for as-cast alloys (after Ref. [97])

up [98]. It is also important to point out that, Fe based alloys suffer from relatively low magnetic entropy change, which would result in low adiabatic temperature changes but may be attractive in cycles designed to span large temperature ranges, i.e. between the freezing and boiling points of typical fluid carriers.

Table 4.1: Peak temperature, peak entropy change, RC_{FWHM} values of promising magnetocaloric materials are presented.

Nominal Composition	T_{pk} (K)	$\lvert\Delta S_M^{pk}\rvert$(1.5T) $Jkg^{-1}K^{-1}$	RC_{FWHM}(1.5T) Jkg^{-1}	RC_{FWHM}(2T) Jkg^{-1}	RC_{FWHM}(5T) Jkg^{-1}	Ref.
$La(Fe_{0.89}Si_{0.11})_{13}H_{1.3}$	291			165.6		[23]
Pr_2Fe_{17}	300				573	[39]
$Gd_5Ge_{1.9}Si_2Fe_{0.1}$	300				630	[21]
$Fe_{88}Zr_7B_4Cu_1$	300	1.3	166		654	[37]
$Fe_{79}Gd_1Cr_8B_{12}$	355	1.42	153		627	[38]
$MnNiGa$	317			30		[42]
γ-$Fe_{72}Ni_{28}$-50 h milled	333	0.5	84	110	250	this study
γ-$Fe_{70}Ni_{30}$-30h milled	363	0.65	158	204	470	this study

Adiabatic Temperature Change, ΔT_{ad}

As mentioned before, the isothermal application of a field, H_{max}, causes a change in entropy, ΔS_M. In this study, the magnetic refrigerants are compared based on their relative cooling powers (RCP) which is obtained from the magnetic entropy curves. However, there is another figure of merit which is equally important in the assessment of magnetic refrigerants. It is the temperature change upon the application of a field under adiabatic conditions, ΔT_{ad}:

$$\Delta T_{ad}(T, H_{max}) = \int_0^{H_{max}} \frac{T}{C_p(T,H)} \left(\frac{\partial M}{\partial T}\right)_H dH \tag{4.12}$$

Zverev et. al., [99] made a simplifying assumption that, within a small temperature interval $(\partial M/\partial T)_H$ is constant and they put forward two extreme cases to Eq. 4.12. First case corresponds to materials undergoing second order transitions that are characterized by their broad curves but relatively lower peak magnetic entropy values in the ΔS_M(T). ΔT_{ad} is approximated as:

$$\Delta T_{ad} = \left(\frac{T}{C_p}\right) \times \Delta S_{max} \tag{4.13}$$

For these type of materials ΔT is determined by the magnitude of the peak ΔS_{max}, temperature at which the maximum mangetic entropy is observed T, and the heat capacity of the material, C_p.

Second extreme case addresses the materials undergoing first order transitions that are known for their large but narrow magnetic entropy curves. Since the materials synthesized in this study fall into the first category, details of the second case will not be given here.

A sample calculation of the adiabatic temperature change for the γ-$Fe_{70}Ni_{30}$ milled for 10 hr will be provided in the remainder of this section. Using the DSC scan in Fig 4.20, C_p of this powder was calculated yielding a value of $\approx$440 J $kg^{-1}K^{-1}$.

Invoking Eq. 4.13 and plugging in the values for T and Δ S_{max} at 5 Tesla for this powder,

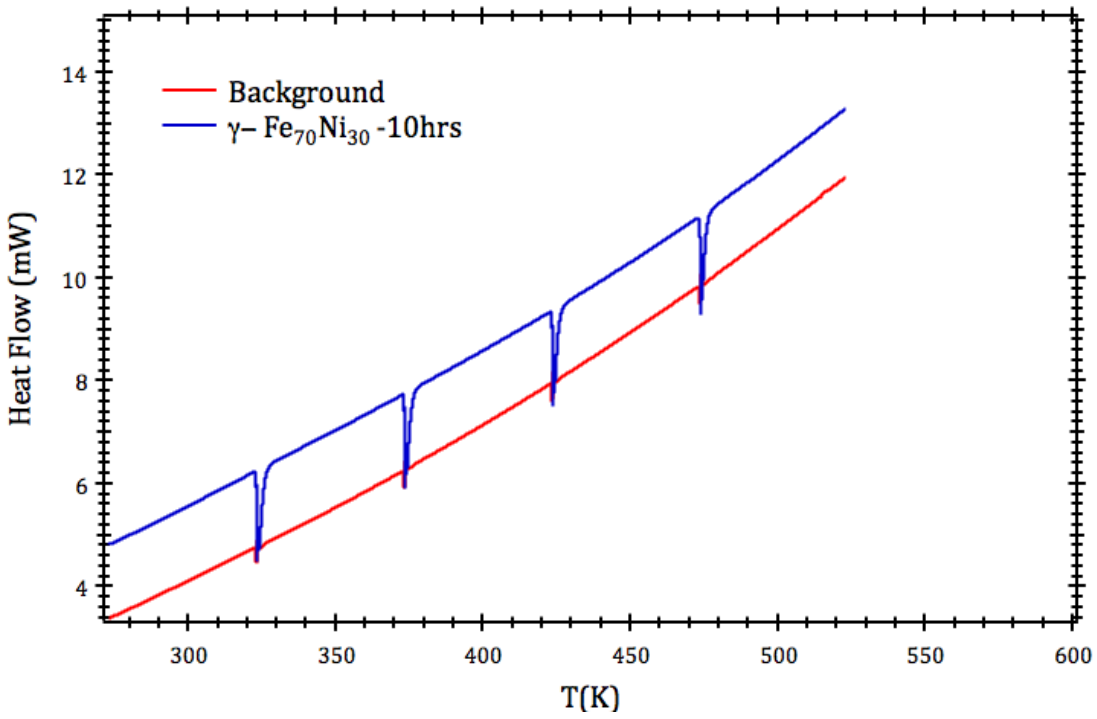

Figure 4.20: DSC scans of γ-$Fe_{70}Ni_{30}$ milled for 10 hrs and the background which is obtained by running the experiment with empty sample holders.

one gets:

$$\Delta T_{ad} = \left(\frac{335K}{440 Jkg^{-1}K^{-1}} \right) \times 2.6 Jkg^{-1}K^{-1}$$
$$\Delta T_{ad} = 2K \tag{4.14}$$

or ΔT_{ad}= 0.4 K at 1 Tesla which is relatively lower than that of materials with first order transition kinetics. For a magnetic refrigerant in the solid state, however, ΔT_{ad} of 1 K/T is taken as a minimum requirement considering several loss mechanisms during operation. These losses could arise from the heat exchange between the refrigerant and the surroundings, viscous flow entropy generation in the heat exchanger and thermal backflow in the refrigerant bed [100].

On the plus side, FeNi alloys can still be used in ferrofluidic applications (see Sec. 3.1) in which broad transition temperatures that span the freezing and boiling points of the carrier fluid are required. Energy losses associated with the heat exchange would also be minimized due to the enhanced surface area of nanoparticles that are suspended in the fluid.

4.2.1.3 Conclusions

Microstructure and magnetocaloric response of mechanically alloyed $Fe_{70}Ni_{30}$ and $Fe_{72}Ni_{28}$ compositions have been studied with the following observations:

I) With milling time, we found that the bcc phase was destabilized with respect to fcc phase for the $Fe_{70}Ni_{30}$ alloy. This agrees well with previous studies, which state that the composition ranges of the fcc and bcc single phase regions are greatly extended with respect to their equilibrium ranges by mechanical alloying [101, 57].

II) Extended milling times induce oxidation of particles due to high temperatures achieved during operation. This can be utilized to tune the T_C of γ-FeNi alloy since preferential oxidation of Fe atoms changes the composition of the particles.

III)γ-$Fe_{70}Ni_{30}$ and γ-$Fe_{72}Ni_{28}$ have desirable magnetocaloric properties near room temperature and extreme economic viability as compared with some other benchmark magnetocaloric refrigerants.

4.2.2 Isothermal Oxidation of γ-FeNi

In section 4.2.1, the idea of tuning the Curie temperature and other magnetic properties through oxidation during milling was conveyed. Here, I present the structure and magnetic properties of γ-FeNi after isothermal oxidation. A VSM was used to oxidize the powders and monitor the changes in the magnetic moment after oxidation. XRD and magnetic entropy calculations were performed on the oxidized alloys which helped to identify the type of oxides present.

4.2.2.1 Results and Discussion

XRD

Fig 4.21 shows x-ray diffraction patterns from powders of annealed γ-$Fe_{72}Ni_{28}$ and after oxidizing at 850, 950 and 1050 K for 1 minute. The oxidation studies were done in a boron nitride crucible which accounts for the presence of boron nitride and iron oxide borate peaks for the powders oxidized at 950 K and 1050 K.

While as quenched γ-$Fe_{72}Ni_{28}$ is single phase FCC, Fe_2NiO_4-Fe_3O_4 and NiO begins to form after oxidizing the powder at 850, 950 and 1050 K.

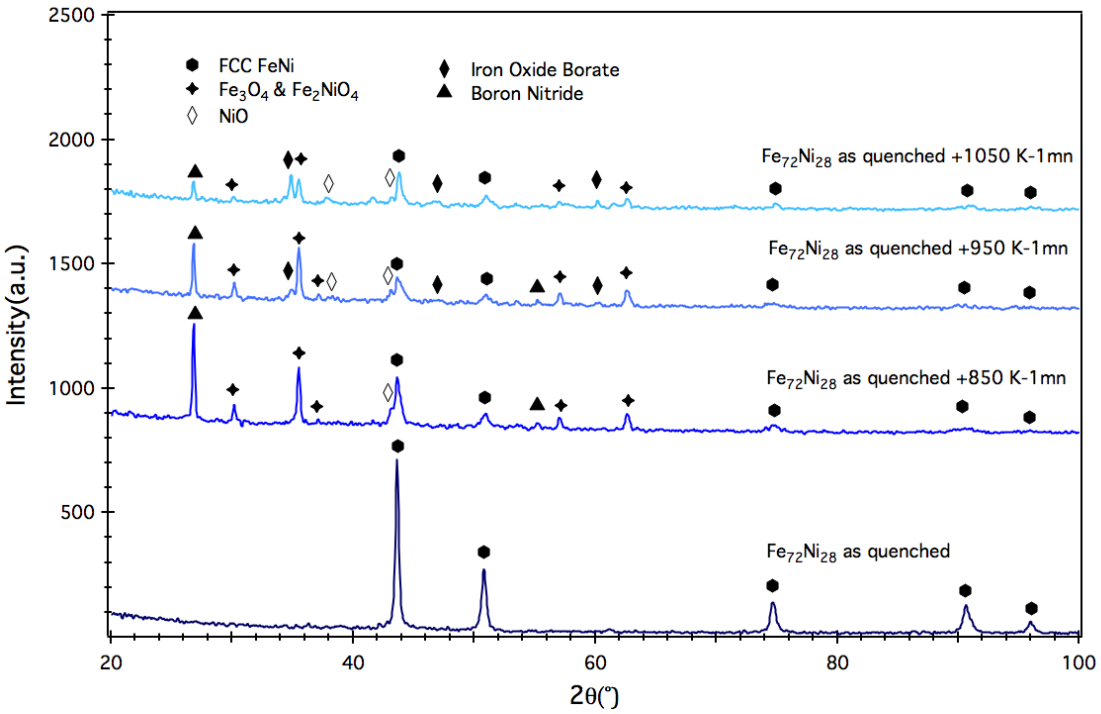

Figure 4.21: X-ray diffraction patterns of as quenched γ-$Fe_{72}Ni_{28}$ and after oxidizing at 850, 950 and 1050 K.

Magnetocaloric Properties

The effect of an oxide can also be observed on the magnetic entropy curves as long as there is a change in oxide's configurational entropy with temperature. This change could be due to a transition from ferromagnetic to paramagnetic state as in a typical ferromagnetic material (γ-FeNi) or from a ferrimagnetic to a paramagnetic state as in Fe_2NiO_4 or Fe_3O_4.

Fig 4.22 presents the entropy curves for annealed γ-$Fe_{72}Ni_{28}$ and after oxidizing it at 850, 950 and 1050 K.

The peak entropy value is observed at 373 K for the as quenched γ-$Fe_{72}Ni_{28}$ and the magnitude of this peak decreases after oxidizing the powder at 850 K for 1 minute. This is mainly because of the growing oxide phases at the expense of the FCC γ-FeNi. As shown in the x-ray diffraction patterns, NiO is one oxide product with a Néel temperature, T_N, $\sim$ 523 K [102]. Therefore, the change in NiO's magnetic state at this temperature is the reason we see a slight bump around 515 K in the magnetic entropy calculations. The slight difference in the temperature can be attributed to the heating rate applied during each experiment.

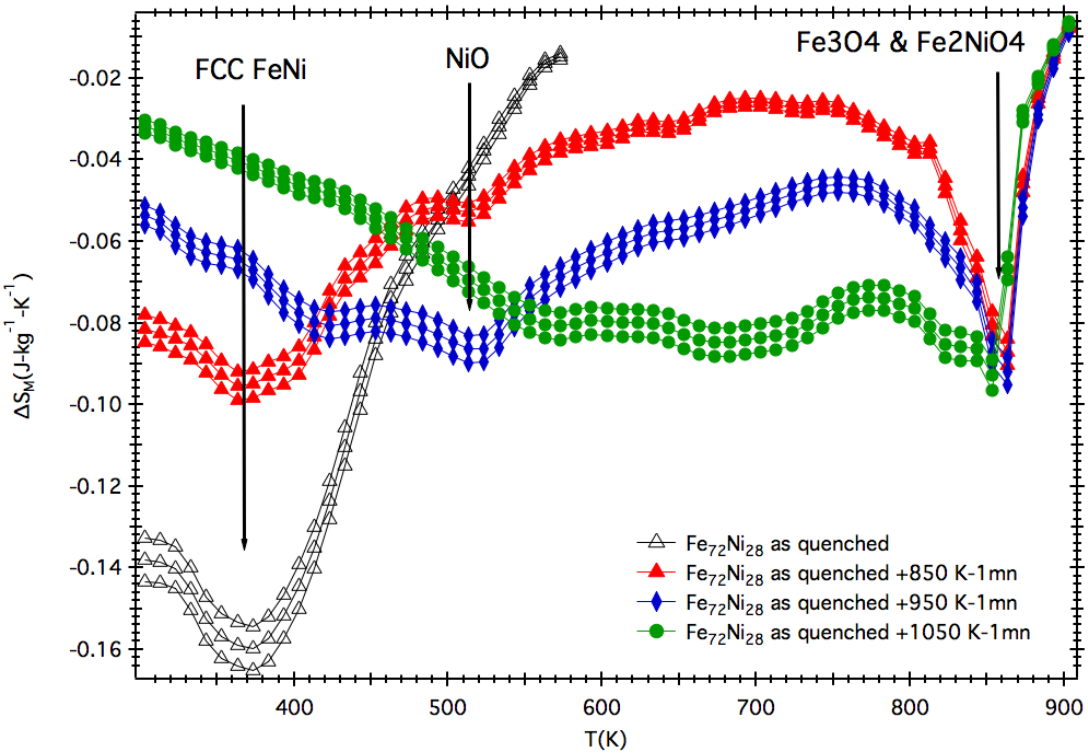

Figure 4.22: Magnetic entropy curves of as quenched γ-$Fe_{72}Ni_{28}$ and after oxidizing at 850, 950 and 1050 K. Entropy curves at a field of 5100, 5300 and 5500 G are presented for each.

Another major peak around 856 K in the entropy curves is due to the presence of both Fe_2NiO_4 (nickel ferrite) and Fe_3O_4 (magnetite). The Néel temperature of nickel ferrite is $\sim$ 858 K while it is $\sim$ 855 K for magnetite [46] which accounts for the magnetic entropy peak at that temperature in Fig. 4.22. Since both oxides have virtually indistinguishable structure (lattice constant) and magnetic properties (Néel temperature), it is not trivial to quantitatively analyze the contribution of each oxide to the entropy peak around $\sim$ 855 K. Both oxides are ferrimagnets meaning that the magnetic moments of the atoms on different sublattices are opposed as in antiferromagnetism. However, unlike an antiferromagnetic material, opposing moments in a ferrimagnet do not cancel out thus resulting in a net magnetic moment.

From Fig. 4.22, even though the magnitude of the entropy peak was reduced after oxidizing the powder at 850 K, the Curie temperature of the fcc phase remained the same. Based on the assumption that the T_C strongly depends on the composition in FeNi system, I conclude that there was not a significant change in the initial composition of the γ-$Fe_{72}Ni_{28}$ after oxidizing at 850 K.

The proposed oxidation reaction which preserves the initial composition during oxidation can be as follows;

$$Fe_{70-7x}Ni_{30-3x} + \frac{13x}{2}O_2 \rightarrow xNiO + 2xFe_2NiO_4 + xFe_3O_4 \tag{4.15}$$

For simplicity, this reaction is given for the $Fe_{70}Ni_{30}$ and the same logic can be applied to $Fe_{72}Ni_{28}$ as well. For the particles oxidized at 850 K, the reaction proceeded in such a way that the starting composition of $Fe_{72}Ni_{28}$ was preserved as demonstrated in Eq. 4.15.

Another important feature of Fig. 4.22 is the enhanced breadth in the entropy curves as the oxidation temperature is elevated. This is due mainly to the graded oxide formation resulting in distributed magnetic exchange interactions thus yielding a distributed Néel temperatures for the oxides depending on their stoichiometries. The "table-like" character of the ΔS_M is desirable for Ericsson type refrigerators in the temperature range of the operation of the device [103]. Processes that make up the Ericsson cycle are slightly different from that of the Carnot cycle presented in Fig. 3.1. The major difference is that the heat transfer occurs in processes during which the magnetic field is kept constant in addition to the two isothermal processes thus resulting in an enhanced heat transfer between the magnetic refrigerant and the fluid. Studies indicate that a constant ΔS_M is required in the refrigeration temperature range for an ideal Ericsson cycle based refrigeration [104, 105]. This can be accomplished either by using magnetocaloric materials that undergo successive magnetic phase transitions or by combining two magnetic materials with slightly different T_C's thus broadening the entropy curve [106]. Here, the table-like character of the magnetic entropy curve was accomplished by the formation of the graded oxide in the nanostructured γ-FeNi.

While XRD and entropy curves do not provide clear evidence for the presence of Fe_3O_4 (magnetite) because of magnetite and nickel ferrite having similar properties, in situ M(T) experiments confirm the presence of this oxide. Fig. 4.23 shows the magnetic moment values against temperature on heating for the as quenched γ-$Fe_{72}Ni_{28}$ and on cooling for the powders of the

same composition oxidized at various temperatures i.e. 850, 950, 1050 K. Heating of the particles was performed under Ar atmosphere up to their respective oxidation temperatures. Then the Ar source was disconnected upon which the oxygen started to enter the system. Powders remained in their respective oxidation temperatures under these conditions for 1 minute and cooled down to room temperature without an Ar source. Oxidizing the particles in VSM using the high temperature furnace equipment allowed us to monitor the magnetic moment during this process. The magnetic moment of the alloy systematically increased with the oxidation temperature on cooling (Fig. 4.23). This is due mainly to the formation of Fe_3O_4 (magnetite) on the surface as it is the only oxide product with a larger magnetic moment than γ-$Fe_{72}Ni_{28}$ (See Table 4.2).

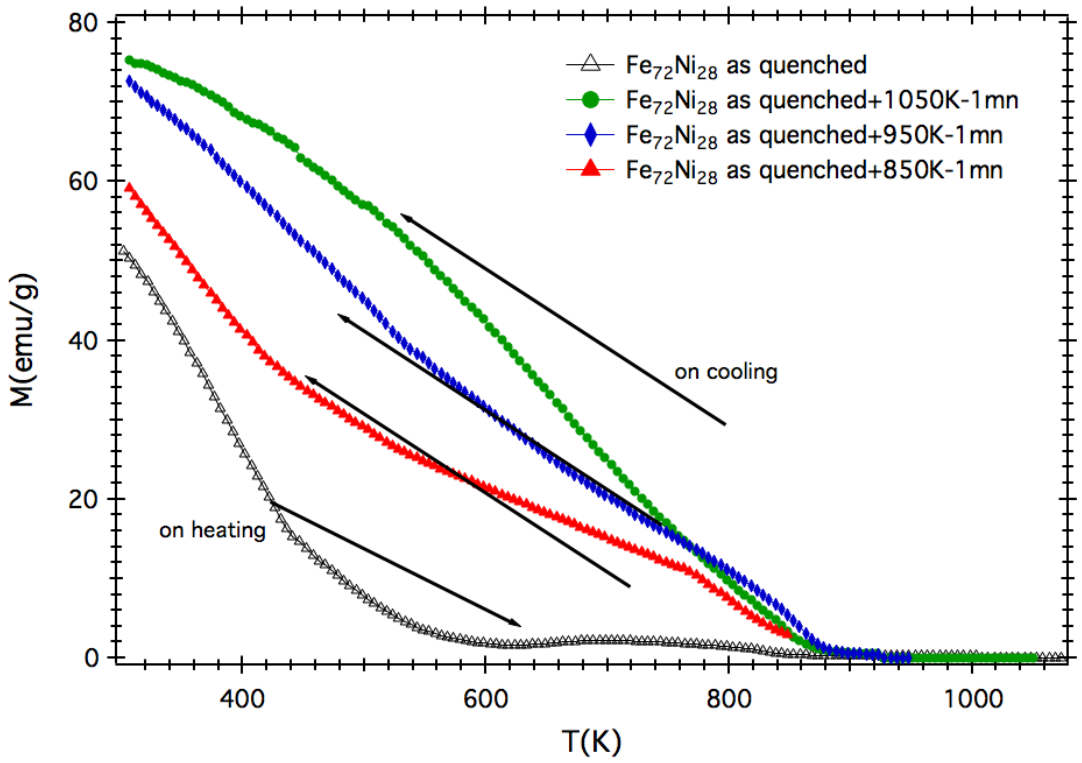

Figure 4.23: In situ M(T) experiments during oxidation of the γ-$Fe_{72}Ni_{28}$ at 850, 950 and 1050 K for 1 minute.

Table 4.2: Curie and Néel temperatures of each phase

Phase	T_C (K)	T_N (K)	M_s (emu/g)	Ref.
γ-$Fe_{72}Ni_{28}$	350		50	[58]
Fe_2NiO_4		858	50	[107]
Fe_3O_4		855	92	[107]
NiO		523	0	[102]

As the results of this section made it clear, the idea of oxidizing only Fe is not a trivial task. It requires a careful adjustment of the temperature and the partial pressure of oxygen. To see what conditions favor the oxidation of Fe only, one can simply construct predominance diagrams. A predominance diagram is a convenient representation of the domains of predominance of the various oxides of metals as temperature and the oxygen potential is varied.

The partial pressure of oxygen at which the metal and the oxide coexist can be expressed as:

$$P_{O_2}^{eq} = \frac{a_{MO_2}}{a_M} exp \frac{\Delta G^o}{RT} \tag{4.16}$$

Using the relationship in Eq. 4.16 and assuming that the activity of metal and the oxide is 1, the predominance diagram for the Fe and Ni can be constructed as in Fig. 4.24.

If the temperature and the partial pressure of oxygen are chosen in such way that they intersect on the right side of each curve in Fig. 4.24, the oxide of each element predominates over the metal component. On the contrary, if they intersect on the left side of each equilibrium line metal does not oxidize. In light of this, the conditions that favor the oxidation of Fe over Ni are designated by horizontal red lines in Fig. 4.24. The desired partial pressure of oxygen can be achieved using Ar as balance at the corresponding oxidation temperature so that the formation of FeO and

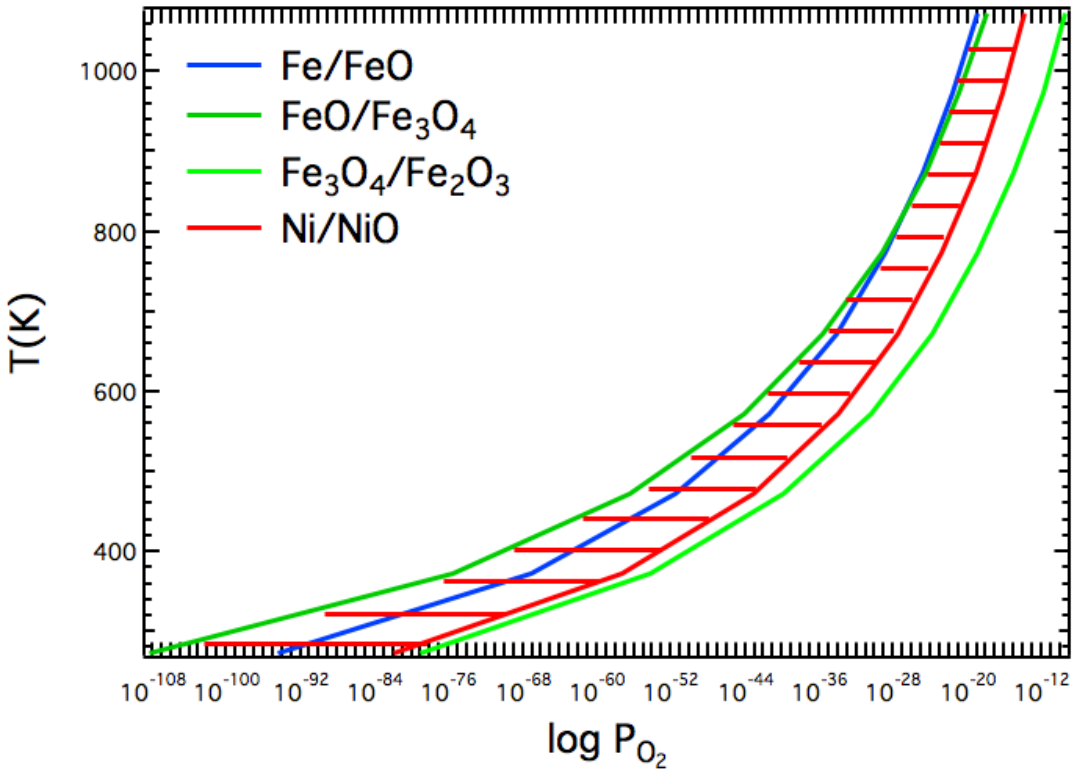

Figure 4.24: The predominance diagram in (log P_{O_2}—T(K) space for the Fe, Ni and O system.

Fe_3O_4 are favored over NiO.

4.3 The Effect of Mo Additions on Structure and Magnetocaloric Effect in γ-FeNi Nanoparticles

The aim of this study is to show the effect of Mo on the structure and magnetic properties of γ-FeNi nanoparticles. The possibility of tuning the Curie Temparature (T_C) of γ-FeNi by small additions of Mo will also be discussed. Additions of molybdenum to the iron-nickel system were made not only for obtaining a high initial permeability also for increasing the electrical resistivity in the early studies. This would, in return, decrease the eddy-current losses and make these alloys preferable alternatives for magnetocaloric and high frequency applications [108]. It was also believed that the high permeability, high resistivity and low energy loss of these alloys could be improved further when the bulk material is reduced to powder followed by annealing [109]. Even though small amounts of sulfur was added into the alloy composition in the past to ease the pulverization process, the alloys in this study were made Sulfur-free.

4.3.1 Experimental Procedure

Alloys of $(Fe_{70}Ni_{30})_{100-x}Mo_x$ (x=1 to x=4) were produced via ball milling. For simplicity, $Fe_{70}Ni_{30}$ will be designated as FeNi and $(Fe_{70}Ni_{30})_{100-x}Mo_x$ alloys from x=1 to x=4 will be designated as Mo_1, Mo_2, Mo_3, Mo_4 respectively. Elemental Fe (particle size-125 mesh), Ni (particle size-100 mesh) and Mo (particle size-100 mesh) obtained from Alfa Aesar with 99.9% purity were mixed and sealed in a steel vial in an Ar atmosphere. Ball milling was performed with a Spex 8000 mixer/mill using hardened steel vials and balls, with a ball-to-powder weight ratio of 10:1. Powders were milled for 30 h. According to Hong et. al., 12 h is sufficient time to reach a steady state microstructure in these alloys [88]. After 30h of milling, powders were characterized by a Philips XPert MPD diffractometer working in a continuous scanning mode using the Cu Kα radiation (λ = 0.154056 nm). Magnetic properties were studied using a Lakeshore 7407 vibrating sample magnetometer using a maximum applied field of 0.55 T. For low temperature magnetic properties a Physical Properties Measurement System (PPMS) with a VSM head was used instead using a maximum applied field of 5 T. The magnetic entropy change due to the application of a magnetic

field has been calculated using a numerical approximation to the equation;

$$\Delta S_M = \int_0^{H_{max}} \left(\frac{\partial M}{\partial T}\right)_H dH \tag{4.17}$$

where ΔS_M is the magnetic entropy change, M is the magnetization, and T is the temperature. The partial derivative is replaced by finite differences and the integration is performed numerically from zero to the maximum value of the applied magnetic field.

4.3.2 Results and Discussion

XRD

Structural analysis of as milled $(Fe_{70}Ni_{30})_{100-x}Mo_x$ powders were performed by x-ray diffraction. Figure 4.25 shows the x-ray diffraction patterns (XRD), to exhibit both BCC and FCC phases for all Mo concentrations. However, FCC to BCC volume ratio was found to increase with increasing Mo content.

The fractions of FCC and BCC phases were determined by comparing the intensities of the BCC(211) and FCC(220) peaks (Fig. 4.25). Unlike BCC(110) and FCC(111) peaks, the selected peaks do not overlap with each other which would otherwise lead to more difficult to interpret results. To correctly estimate the fractions of each phase, XRD peaks need to be corrected for Lorentz polarization, multiplicity and structure factors [67]. The equation for calculating the phase fractions of each phase is [88];

$$\frac{f_{bcc}}{f_{fcc}} = CF\frac{I_{bcc}}{I_{fcc}} \tag{4.18}$$

where f_{bcc} and f_{fcc} are the fractions of the phases, I_{bcc} and I_{fcc} are the intensities measured from the experimental data. The correction factor, CF, can be calculated by dividing the theoretical

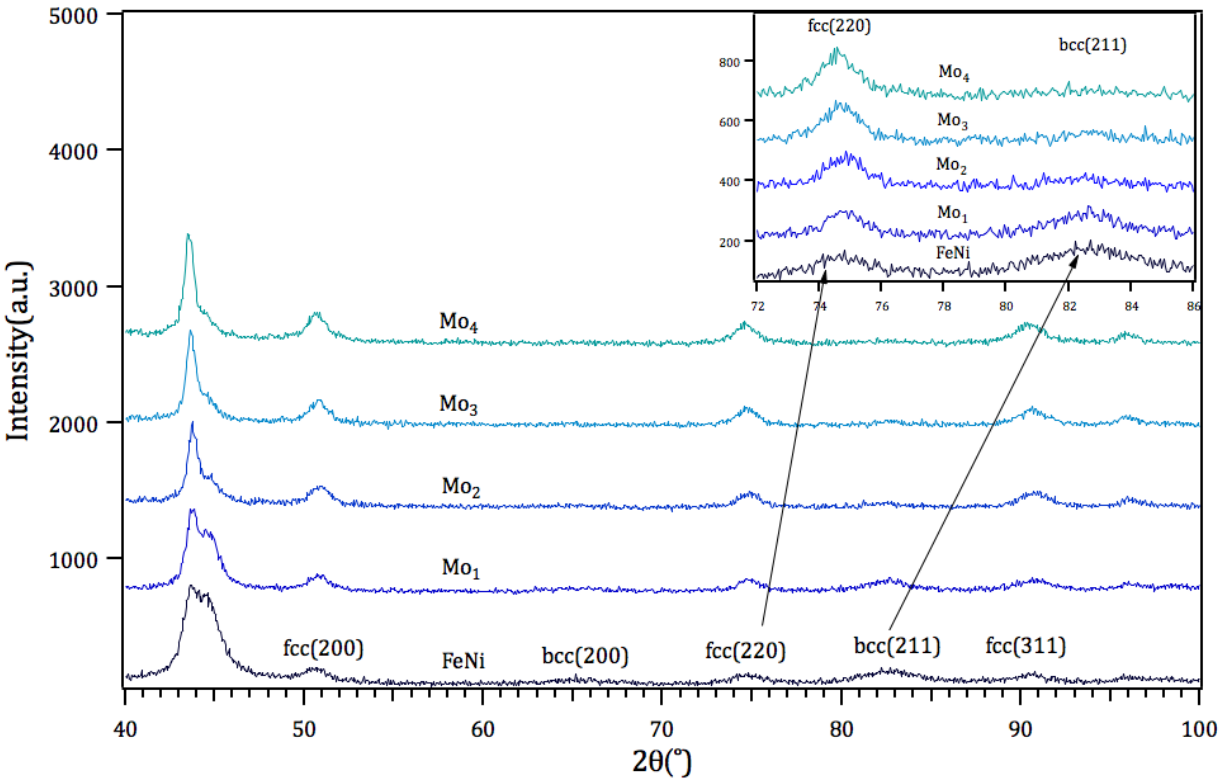

Figure 4.25: Inset: fcc(220) and bcc(221) peaks of as milled $(Fe_{70}Ni_{30})_{100-x}Mo_x$ (x=1 to x=4) alloys . Main Figure: x-ray diffraction patterns of as milled $(Fe_{70}Ni_{30})_{100-x}Mo_x$ (x=1 to x=4) alloys which are labeled as FeNi, Mo_1, Mo_2, Mo_3, Mo_4 respectively.

intensities of $I_{theoretical(bcc)}$ to $I_{theoretical(fcc)}$:

$$CF = \frac{I_{theoretical(bcc)}}{I_{theoretical(fcc)}} \tag{4.19}$$

and the theoretical intensity is expressed as:

$$I_{theoretical} = |F|p\left(\frac{1+cos^2(2\theta)}{sin^2(2\theta)cos(\theta)}\right) \tag{4.20}$$

where F is the structure factor, p is the multiplicity and the term in parenthesis is the Lorentz polarization factor. For the BCC(211) and FCC(220) planes CF is calculated to be, 2.62. Following this procedure, the phase fractions were calculated and plotted against Mo concentration in Fig. 4.26.

While several studies present Molybdenum as a ferrite stabilizer [110, 111, 112, 113], quite a few claim that Mo can also be used to stabilize the austenite phase [114, 115]. The effect of Mo on

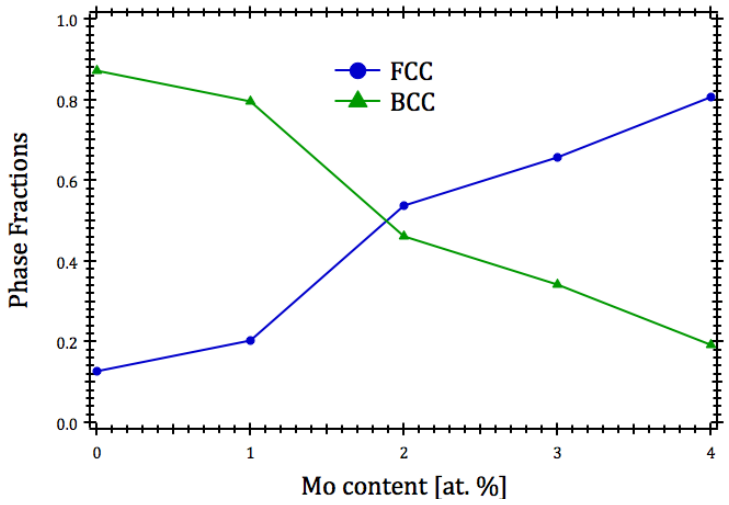

Figure 4.26: Fractions of bcc and fcc phases in as milled $(Fe_{70}Ni_{30})_{100-x}Mo_x$ (x=1 to x=4) alloys, determined by x-ray diffractometry.

the stability of austenite can be understood better considering the Fe-Ni-Mo ternary phase diagram in Fig. 4.27 which shows the phase boundaries for the alloys cooled slowly to room temperature. When quenched, a few modifications to the phase diagram are needed. For instance, the magnetic transformation boundary line disappears for the alloys that are quenched due to the suppresion of the θ phase.

As designated in Fig. 4.27, $Fe_{70}Ni_{30}$ is on the boundary line between the two phase region (α+γ) and single phase region γ and additions of Mo pulls the alloy into the γ phase region thus further stabilizing the γ. Put another way, with additions of Mo to the FeNi binary less Nickel is needed to stabilize the γ phase.

Similar conclusions can be drawn with the FactSage^{TM} calculations as well. The diagram given in Fig. 4.28 shows the effect of Mo on the phase stability of the austenite(A1) and the ferrite (A2) phases. Additions of Mo stabilize the austenite phase simply because the boundary between the austenite and the (austenite+ferrite) phase fields is slightly lower ($\approx$455 °C) in the presence of Mo while it is $\approx$490 °C for the Mo free alloy. Namely, additions of Mo supress all other phases other than austenite and ferrite by depressing the A2 temperature.

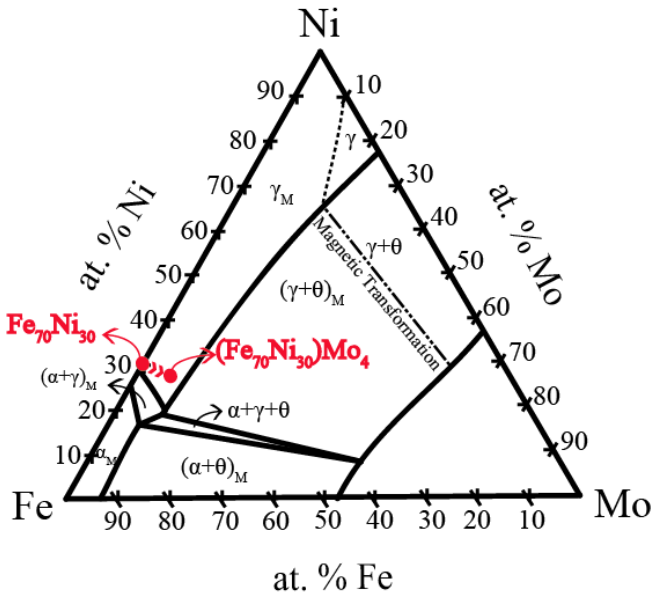

Figure 4.27: Phase diagram of Fe-Ni-Mo system at low temperatures (adapted from [108]).

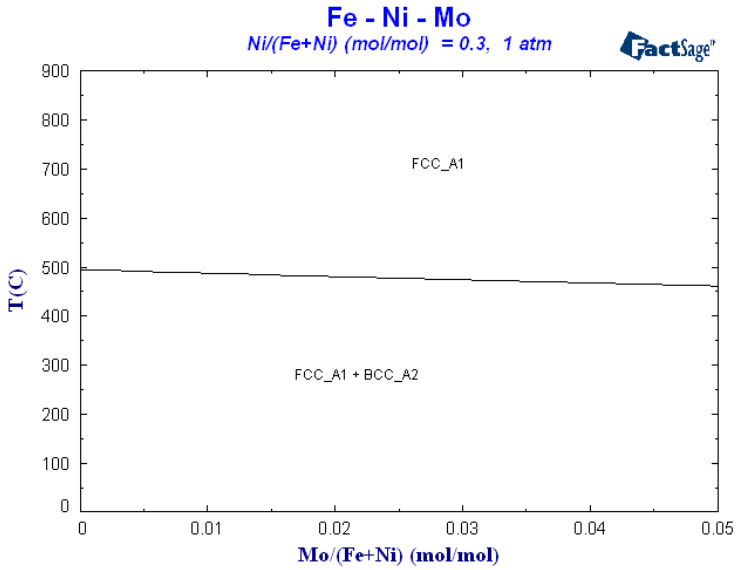

Figure 4.28: Calculated phase diagram of Fe-Ni-Mo system showing the effect of Mo at low concentrations on the phase stability of austenite and ferrite phases (calculated using FactSage^{TM}).

Magnetocaloric Properties

The magnetocaloric response is calculated according to Eq. 4.17 using the isothermal magnetization curves. The magnetic entropy changes, ΔS_M, for the annealed γ-FeNi, γ-Mo_1, γ-Mo_2, γ-Mo_3 and γ-Mo_4 alloys are illustrated in Fig. 4.29 for a maximum applied field of 0.55 T.

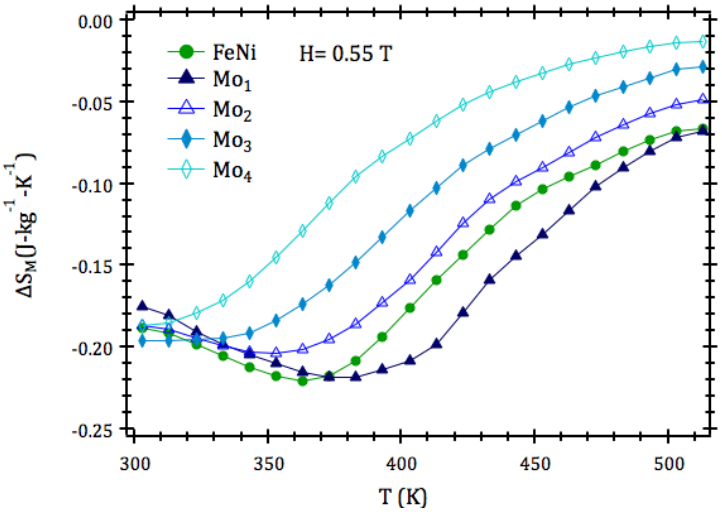

(a)

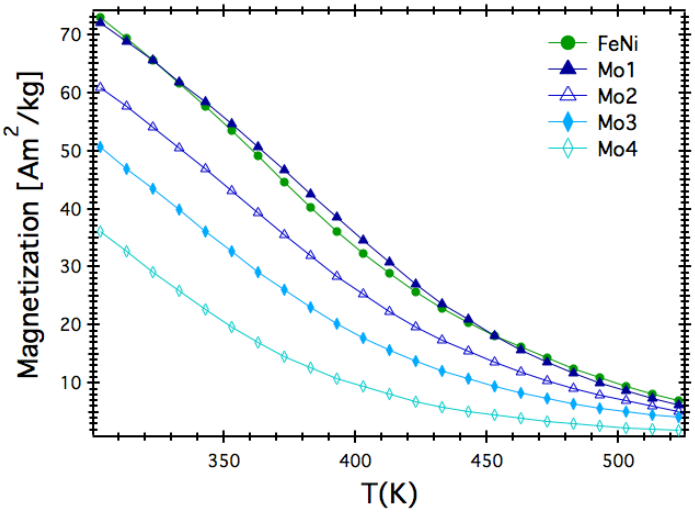

(b)

Figure 4.29: (a) Temperature dependence of the magnetic entropy change, ΔS_M of solution annealed $(Fe_{70}Ni_{30})_{100-x}Mo_x$ (x=0 to x=4) at 0.55 T; (b)Magnetization vs. temperature measurements for solution annealed $(Fe_{70}Ni_{30})_{100-x}Mo_x$ (x=0 to x=4)

From Fig. 4.29, it can be seen that small additions of Mo into the γ-$Fe_{70}Ni_{30}$ decrease the T_C of the alloy and the magnetic moment, which agrees well with previous studies [96]. There are

two reasons for the reduction in magnetic moment with additions of the Mo. First, the T_C reaches near room temperature, which brings about reduction in the magnetic moment as it can be seen in Fig. 4.29(b). Secondly, Mo decreases the spin up electron density of the d-band state, $n_d^{\uparrow}$, in the FeNi system, which reduces the magnetic moment as dictated by the virtual bound state model [46, 116] Virtual bound state and magnetic valence models [117] have been used ubiquitously in interpreting the moment reduction in crystalline and amorphous alloys [118] due to early transition metal additions.

Since γ-Mo_4 has the T_C closest to room temperature, magnetocaloric properties of this alloy was measured using PPMS to obtain the data below room temperature. First, magnetization vs. field measurements were taken from 140 K to 500 K as shown in Fig. 4.30

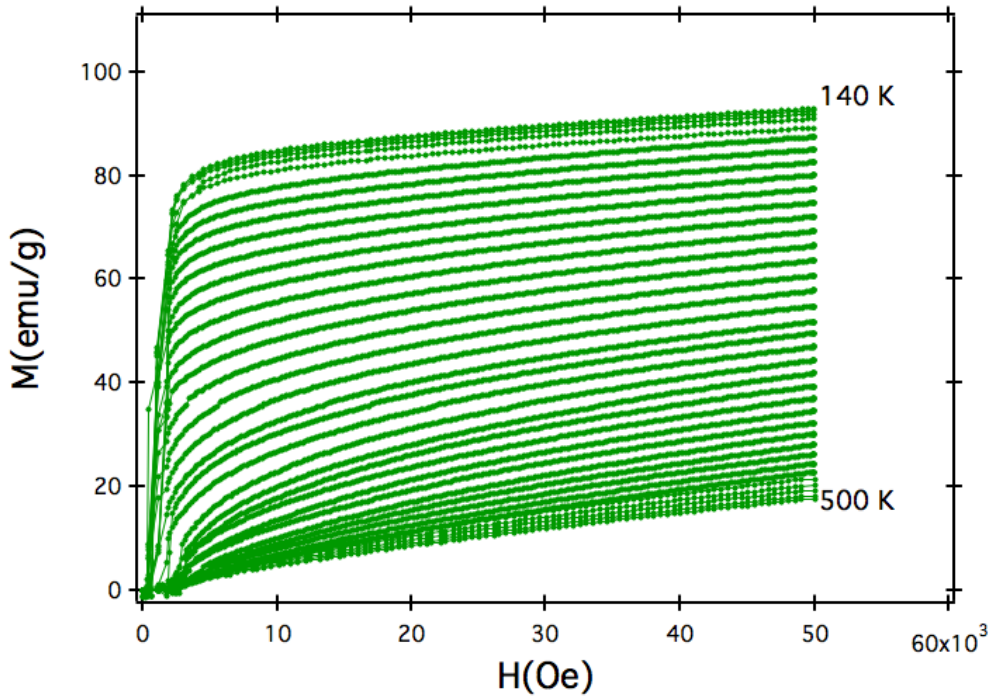

Figure 4.30: Magnetization isotherm curves obtained from 190K to 500 K for a maximum applied field of 5 T.

Then the magnetic entropy was calculated in the same way as for the other alloys in this study (See Fig. 4.31). The experimental RC_{FWHM} value of $(Fe_{70}Ni_{30})_{96}Mo_4$ was calculated to be 432 Jkg^{-1}. For the alloys lacking the experimental data at high fields, the RC_{FWHM} can be expressed as a power law for materials with a second order phase transition. By extrapolating the

experimental data to higher fields, one can compare the response of the alloy of interest to some of the benchmark refrigerants.

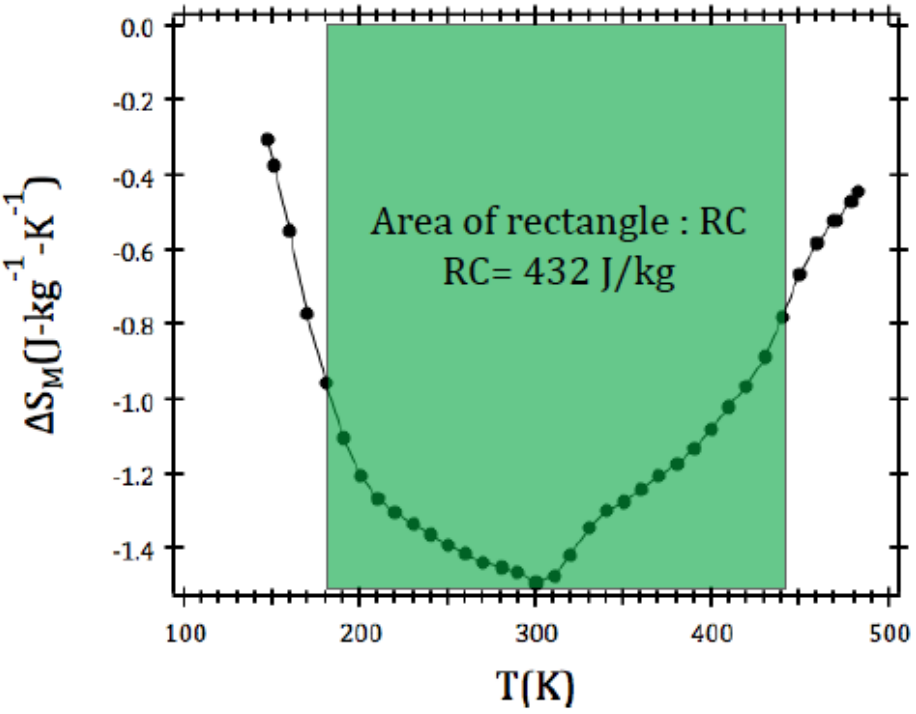

Figure 4.31: Temperature dependence of the magnetic entropy change, ΔS_M of solution annealed $(Fe_{70}Ni_{30})_{96}Mo_4$ at 5 T.

In Table 4.3, the alloys presented in this study are compared to those well known magnetic refrigerants. From Table 4.3, it is clear that Mo can be used as a means to tune the T_C without compromising the RC_{FWHM}. Even though the magnetic moment is slightly suppressed with additions of Mo into the FeNi, the RC_{FWHM} of the Mo alloys remains virtually the same. This is because of the enhanced width of the entropy curve through Mo additions which balances out the reduction resulting from the suppressed magnetic moment. For maximum thermodynamic efficiency, a thermodynamic cycle is typically operated of a range of temperatures so a large peak entropy is not necessarily desirable. This technique offers advantages over previously published routes designed to produce nanocrystal/amorphous nanocomposites [119], with near room temperature Curie temperatures in the size of the RC and cost of the alloy. It also has advantages over chemical synthesis techniques [75] in the potential scalability of the process. Finally, besides magneto caloric appli-

cations, it may also offer possibilities for self-regulated RF heating for hyperthermia applications [120].

Table 4.3: Peak temperature, peak entropy change, RC_{FWHM} values of promising magnetocaloric materials are presented.

Nominal Composition	T_{pk} (K)	$\|\Delta S_M^{pk}\|$(1.5T) $Jkg^{-1}K^{-1}$	RC_{FWHM}(1.5T) Jkg^{-1}	RC_{FWHM}(2T) Jkg^{-1}	RC_{FWHM}(5T) Jkg^{-1}	Ref.
$La(Fe_{0.89}Si_{0.11})_{13}H_{1.3}$	291			165.6		[23]
Pr_2Fe_{17}	300				573	[39]
$Gd_5Ge_{1.9}Si_2Fe_{0.1}$	300				630	[21]
$Fe_{88}Zr_7B_4Cu_1$	300	1.3	166		654	[37]
$Fe_{79}Gd_1Cr_8B_{12}$	355	1.42	153		627	[38]
$MnNiGa$	317			30		[42]
$Fe_{72}Ni_{28}$	333	0.5	84	110	250	this study
$Fe_{70}Ni_{30}$	363	0.65	158	204	470	this study
$(Fe_{70}Ni_{30})_{99}Mo_1$	373	0.65	154	201	460	this study
$(Fe_{70}Ni_{30})_{98}Mo_2$	353	0.62	144	190	445	this study
$(Fe_{70}Ni_{30})_{97}Mo_3$	320	0.6	137	186	440	this study
$(Fe_{70}Ni_{30})_{96}Mo_4$	300	0.6	130	175	432	this study

Economics

As mentioned before, the cost associated with the production of magnetocaloric refrigerants is a big barrier against industrial scale-up. To have better insight in the economic aspect of this issue, a detailed price analysis was undertaken. In Fig. 4.32, RC of the most promising magnetic refrigerants with respect to its cost at a field of 5T are compared. The values of RC for these materials were calculated by FWHM method and the results were divided by the cost per kilogram

of the constituent elements of each material [121]. This figure considers not only the magnetocaloric properties but also the prices of each compound. Therefore, it can be used as a means to highlight the most economically advantageous refrigerant with good magnetocaloric properties. For instance, $Gd_5Ge_{1.9}Si_2Fe_{0.1}$, $Fe_{88}Zr_7B_4Cu_1$, and Pr_2Fe_{17} have respectable RC values from the energy standpoint only. However, the prices associated with Gd, Zr, B, and Pr elements lower their RC in terms of J/$ (Fig. 4.32). In contrast, FeNi is a lowcost compound coupled with good magnetocaloric properties, which accounts for the giant response we see in Fig. 4.32.

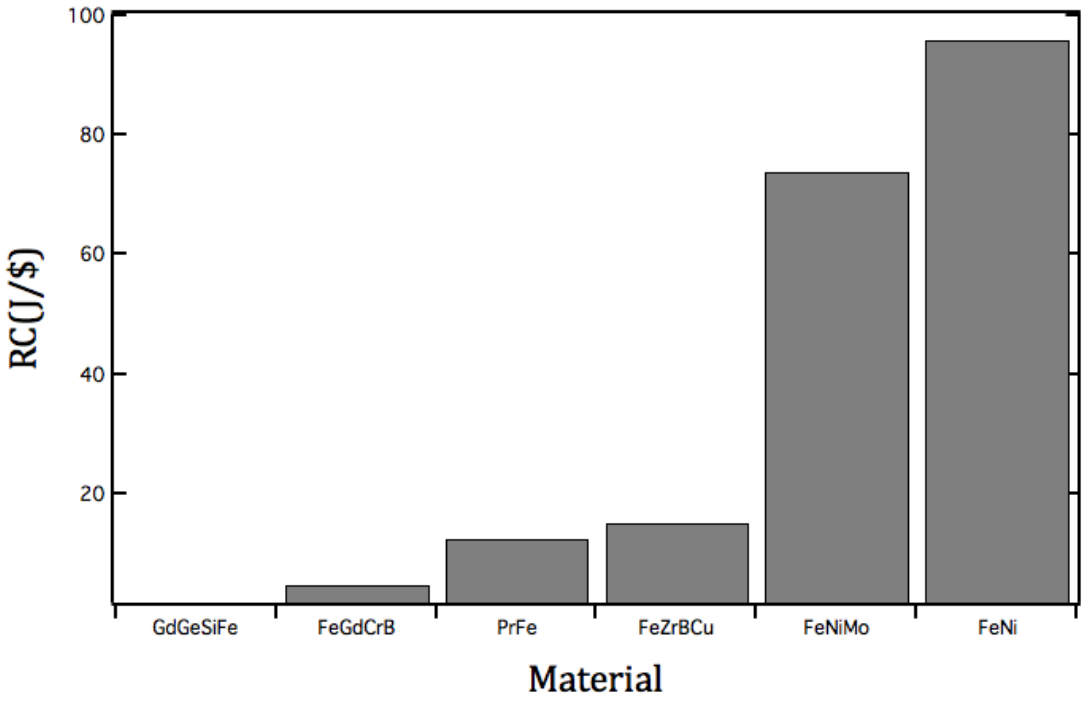

Figure 4.32: Refrigeration capacity in J/$ for various magnetocaloric refrigerants.

4.4 Conclusions

This study can be summarized as follows:

I) The ball milling of the Fe, Ni and Mo particles for 30 hours led to alloy formation as indicated by structural data.

II) Increasing the Mo content has been found to promote the FCC γ-phase formation over the BCC α-phase.

III) The Mo was used to tune the T_C of the FeNi alloy without lowering the RC_{FWHM} values significantly. The Mo_3 and Mo_4 alloys have peak temperatures 320 K and 300 K respectively, thus making these alloys appropriate for applications operating near room temperature such as magnetic refrigeration and self-regulated hyperthermia for cancer treatments.

IV) Even though the RC_{FWHM} of the Mo alloys are slightly lower than that of other important refrigerants (Table 4.3), their attractive economic viability would make them preferable alternatives for large scale production.

5 Summary & Outlook

In the last decade, the worldwide shortage of rare-earth elements gave considerable impetus to the research efforts in synthesizing rare-earth free magnetic materials that can meet the needs of advanced devices and motors of every kind. As for the United States, the transfer of the rare-earth manufacturing facilities to China made it clear that alternative ways had to be investigated that will result in new types of magnetic materials with superior performance [76].

Magnetic materials are versatile and can be utilized in power plants, sensors, data storage systems and more importantly in green energy technologies such as wind turbines and refrigerators. It was reported that, every year, ≈42 % of energy in US is used in residential and commercial sectors and ≈50 % of this energy goes into climate control devices i.e., air conditioners, refrigerators [122]. Therefore, even 1 % improvement in cooling technology will save million dollars on the budget. The growing consensus is that the magnetic refrigeration could find a solution to the energy problem as it is 20 % more energy efficient than conventional refrigerators. This motivated numerous researchers to concentrate on magnetic cooling technology which explains the radical increase in the number of publications in the last decade.

Magnetocaloric materials are classified as those undergoing first order and second order magnetic transition. First order materials are known to exhibit large magnetic entropy changes but with a thermal/magnetic hysteresis and a narrow operation temperature range. Materials undergoing second order transition, on the other hand, have lower magnetic entropy changes with virtually no hysteresis and a broad temperature range. The major component in these alloys is Fe which makes these alloys economically more viable than their rare earth containing counterparts with first order phase transition. Transition metal based refrigerants have good mechanical properties, high resistivity and corrosion resistance too, thus making them attractive candidates in magnetic refrigeration technology. The goal of the thesis was to show the possibility of synthesizing FeNi alloys, which are abundant in the Earth's crust, through nonequilibrium routes that could yield promising magnetic refrigerants of the future and lower the demand on the rare-earth elements.

In this study, we utilized mechanical alloying, a nonequilibrium synthesis procedure, to pro-

duce nanoparticles of γ-$Fe_{70+x}Ni_{30-x}$ for room temperature applications. This entails the T_C to be near room temperature. After finding the optimum composition in binary FeNi, $Fe_{70}Ni_{30}$, which has both a relatively higher magnetic moment with a low T_C, the tunability of the T_C was demonstrated both by controlling the oxidation kinetics and by additions of a ternary element. While oxidation during milling exhibited a systematic increase of the T_C with milling time, isothermal oxidation at elevated temperatures provided more difficult to interpret results. Isothermal oxidation results also showed that the idea of tuning the magnetic properties by controlling the oxidation is not an easy task to undertake. This was mainly due to the difficulties arising from controlling the gas environment to oxidize only Fe in the alloy.

In contrast, tuning the T_C with additions of a ternary element was significantly easier than controlling the oxidation. There are a number of elements known to suppress the T_C in Fe, Ni, Co alloy systems; Mn, Cr, Mo. In this study, Mo was added to the binary FeNi binary and the composition $(Fe_{70}Ni_{30})_{96}Mo_4$ was shown to have $T_C \approx 30\,^{\circ}\mathrm{C}$ with a refrigeration capacity of 432 J/kg at a field of 5 T. This is on the same order of magnitude with those of rare-earth based refrigerants and the economic analysis made it clear that these alloys are far more cost-effective which would facilitate mass production.

Finally, as demonstrated in the applications section, the ultimate goal is to use the γ-FeNi nanoparticles in a liquid medium by suspending the nanoparticles in a fluid carrier. This requires fine sized nanoparticles with a polar surface. In this application, the fluid is expected to circulate in a loop by taking the heat from a heat source and transferring it to the surroundings. Magnetic nanoparticles with a T_C near room temperature will maximize the amount of heat transferred in each cycle through the magnetocaloric effect. γ-FeNi alloy does have relatively lower peak magnetic entropy changes compared to their rare-earth containing counterparts but with broader transitions nonetheless, thus making it a prominent candidate for ferrofluid applications.

6 Future Work

The adjustments to the composition in γ-FeNi alloys having T_C's near room temperature with respectable magnetic properties was mostly accomplished. With additions of Mo, alloys having T_C at room temperature were synthesized. Other elements such as Mn, Cr as a ternary can be added to the γ-$Fe_{70}Ni_{30}$ which would result in alloys with larger moments and magnetic entropy changes than FeNi-Mo alloys. With additions of Mn and Cr, the antiferromagnetic elements distribute themselves in the matrix thus reinforcing the FeNi spins to align in a direction which would eventually give rise to a larger response in a magnetic field.

The path forward with the nanocomposite alloys is to narrow the distribution of exchange interactions because the transition temperature of FeNi system seems to be too wide for most interesting thermodynamic cycles. One way to realize this is by coarsening the FeNi grains. This will enhance the MCE response of the alloy. However, one needs to strike the right balance when coarsening because for a heat pump application particles still need to be on the nanoscale for them to be viably suspended in solutions.

Regarding the synthesis procedure, the alloys were synthesized using spex mill with particle size ≈5-10 μm. However, as it was made clear in Sec. 3.1, the particles need to be on the nanoscale to be suspended in solutions. Spex milling, however, is inadequate for producing such nanoparticles as particles tend to agglomerate at elevated temperatures achieved during milling. Milling at cryogenic temperatures would provide a solution to this problem. This is mainly because the particles become more brittle at cryogenic temperatures thus resulting in alloys that are size appropriate for suspension in solvents.

An alternative way of minimizing the agglomeration can be realized by the addition of a process control agent (PCA) during milling. This is important especially when the particles are ductile. The function of the PCA is to adsorb on to the surface of the particles and minimize cold welding during milling thus inhibiting agglomeration. The reduction of cold welding lowers the surface tension of the particles which results in finer particles with shorter milling times.

In this thesis, the main focus was to investigate γ-FeNi alloys as a possible candidate in

magnetic refrigeration. However, these alloys can also be studied for biomedical applications , cancer therapies being the most prominent one. This entails performing RF heating experiments on the compositions having T_C's in the range of $42 - 46\,^{\circ}\mathrm{C}$. As shown in Table 4.3, $(Fe_{70}Ni_{30})_{97}Mo_3$ alloy has T_C around $47\,^{\circ}\mathrm{C}$ thus making it an ideal candidate for hypothermia treatment of cancer cells provided that they have a respectable amount of heat dissipation upon the application of an AC magnetic field. Besides, particles have an oxide layer which will facililate the attachment of the surfactants to their surface thus allowing the formation of stable ferrofluids. Oxide layer also introduces additional anisotropies to the system which increases the power-loss thus giving rise to larger heating rates.

References

[1] J. K. A. Gschneidner and V. Pecharsky, "Magnetocaloric materials," *Ann. Rev. Mater. Sci*, vol. 30, p. 387, 2000.

[2] E. Bruck, O. Tegus, L. Zhang, X. Li, F. de Boer, and K. Buschow, "Magnetic refrigeration near room temperature with fe2 p-based compounds," *J. Alloy. Compd.*, vol. 32, p. 383, 2004.

[3] A. Planes, L. Manosa, and A. Saxena, *Magnetism and Structure in Functional materials*. Springer-Verlag Berlin, 2005.

[4] E. Warburg, "Magnetische untersuchungen," *Ann. Phys. (Leipzig)*, vol. 13, p. 141, 1881.

[5] W. Giaque *J. Am. Chem. Soc.*, vol. 49, p. 1870, 1927.

[6] P. Debye *Ann. Phys. (Leipzig)*, vol. 81, p. 1154, 1926.

[7] R. McMichael, R. Shull, L. Swartzendruber, L. Bennett, and R. Watson, "Magnetocaloric effect in superparamagnets," *J. Magn. Magn. Mater.*, vol. 111, p. 29, 1992.

[8] A. Tishin and Y. Spichkin, *The Magnetocaloric Effect and its Applications*. Institute of Physics Publishers, Bristol, UK, 2003.

[9] A. Arrott and J. Noakes, "Approximate equation of state for nickel near its critical temperature," *Phys. Rev. Lett.*, vol. 19, p. 786, 1967.

[10] V. Franco and A. Conde, "Scaling laws for the magnetocaloric effect in second order phase transitions: From physics to applications for the characterization of materials," *Int. J. Refrig.*, vol. 33, p. 465, 2010.

[11] H. Oesterreicher and F. Parker, "Magnetic cooling near curie temperatures above 300 k," *J. Appl. Phys.*, vol. 55, p. 4334, 1984.

[12] V. Franco, J. Blázquez, and A. Conde, "Field dependence of the magnetocaloric effect in materials with a second order phase transition: A master curve for the magnetic entropy change," *Appl. Phys. Lett.*, vol. 89, p. 222512, 2006.

[13] J. Kouvel and Fisher, "Detailed magnetic behavior of nickel near its curie point," *Phys. Rev.*, vol. 136, p. A1626, 1964.

[14] V. Franco, J. Blázquez, C. Conde, and A. Conde, "A constant magnetocaloric response in femocub amorphous alloys with different fe/b ratios," *Appl. Phys. Lett.*, vol. 88, p. 042505, 2006.

[15] V. Franco, J. Borrego, C. Conde, and A. Conde, "Refrigerant capacity of fecrmocugapcb amorphous alloys," *J. Appl. Phys.*, vol. 100, p. 083903, 2006.

[16] K. Gallagher, M. Willard, V. Zabenkin, D. Laughlin, and M. McHenry, "Distributed exchange interactions and temperature dependent magnetization in amorphous fe(88-x)co(x)zr7b4cu1 alloys," *J. Appl. Phys.*, vol. 85, p. 5130, 1999.

[17] N. Jones, H. Ucar, J. Ipus, M. McHenry, and D. Laughlin, "The effect of distributed exchange parameters on magnetocaloric refrigeration capacity in amorphous and nanocomposite materials," *J. Appl. Phys.*, vol. 111, p. 07A334, 2012.

[18] M. Wood and W. Potter, "General analysis of magnetic refrigeration and its optimization using a new concept: maximization of refrigerant capacity," *Cryogenics*, vol. 25, p. 667, 1985.

[19] A. O. Pecharsky, K. A. Gschneidner, and V. K. Pecharsky, "The giant magnetocaloric effect of optimally prepared gd5si2ge2," *J. Appl. Phys.*, vol. 93, p. 4722, 2003.

[20] L. Morellon, J. Stankiewicz, B. Garca-Landa, P. Algarabel, and M. Ibarra *Appl. Phys. Lett.*, vol. 73, p. 3462, 1998.

[21] V. Provenzano, A. Shapiro, and R. Shull, "Reduction of hysteresis losses in the magnetic refrigerant gd5ge2si2 by the addition of iron," *Nature*, vol. 429, p. 853, 2004.

[22] F. Hu, M. Ilyn, A. Tishin, J. Sun, and G. Wang, "Direct measurements of magnetocaloric effect in the first-order system lafe11.7si1.3," *J. Appl. Phys.*, vol. 93, p. 5503, 2003.

[23] S. Fujieda, A. Fujita, and K. Fukamichi, "Large magnetocaloric effect in la(fe(x)si(1-x))13 itinerant-electron metamagnetic compounds," *Appl. Phys. Lett.*, vol. 81, p. 1276, 2002.

[24] J. Lyubina, R. Schäfer, N. Martin, L. Schultz, and O. Gutfleisch, "Novel design of la(fe,si)13 alloys towards high magnetic refrigeration performance," *Adv. Mater.*, vol. 22, p. 3735, 2010.

[25] M. Q. Huang, W. E. Wallace, and M. E. McHenry, "Soft magnetic properties of laco13 and la?co, fe13 alloys," *J. Appl. Phys.*, vol. 83, p. 6471, 1998.

[26] M. P. Annaorazov, S. A. Nikitin, A. L. Tyurin, K. A. Asatryan, and A. K. Dovletov, "Anomalously high entropy change in ferh alloy,"

[27] M. Manekar and S. B. Roy, "Reproducible room temperature giant magnetocaloric effect in ferh," *J. Phys. D: Appl. Phys.*, vol. 41, p. 192004, 2008.

[28] H. Wada and T. Asano, "Effect of heat treatment on giant magnetocaloric properties of mn1+δ as1-xsbx," *J. Magn. Magn. Mater.*, vol. 290, p. 703, 2005.

[29] O. Gutfleisch, M. A. Willard, E. Brck, H. Christina, Chen, S. G. Sankar, and J. Ping Liu, "Magnetic materials and devices for the 21st century: Stronger, lighter, and more energy efficient," *Adv. Mater.*, vol. 23, p. 821, 2011.

[30] J. Liu, T. Gottschall, K. P. Skokov, J. D. Moore, and O. Gutfleisch, "Giant magnetocaloric effect driven by structural transitions," *Nature Materials*, vol. 11, p. 620, 2012.

[31] M. McHenry, M. Willard, and D. Laughlin, "Amorphous and nanocrystalline materials for applications as soft magnets," *Prog. Mater. Sci.*, vol. 44, p. 291, 1998.

[32] I. Skorvanek and J. Kovac, "Magnetocaloric behaviour in amorphous and nanocrystalline fenbb soft magnetic alloys," *Czech J. Phys.*, vol. 54, p. D189, 2004.

[33] S. Min, K. Kim, S. Yu, H. Suh, and S. Lee, "Analysis of magnetization and magnetocaloric effect in amorphous fezrmn ribbons," *J. Appl. Phys.*, vol. 97, p. 10M310, 2005.

[34] V. Franco, J. Blázquez, and A. Conde, "The influence of co addition on the magnetocaloric effect of nanoperm-type amorphous alloys," *J. Appl. Phys.*, vol. 100, p. 064307, 2006.

[35] V. Franco, J. Blázquez, M. Millán, J. Borrego, C. Conde, and A. Conde, "The magnetocaloric effect in soft magnetic amorphous alloys," *J. Appl. Phys.*, vol. 101, p. 09C503, 2007.

[36] V. Franco, C. Conde, J. Blázquez, and A. Conde, "A constant magnetocaloric response in femocub amorphous alloys with different fe/ b ratios," *J. Appl. Phys.*, vol. 101, p. 093903, 2007.

[37] R. Caballero-Flores, V. Franco, A. Conde, K. Knipling, and M. Willard, "Influence of co and ni addition on the magnetocaloric effect in fe88-2xcoxnixzr7b4cu1 soft magnetic amorphous alloys," *Appl. Phys. Lett.*, vol. 96, p. 182506, 2010.

[38] J. Law, R. Ramanujan, and V. Franco, "Tunable curie temperatures in gd alloyed febcr magnetocaloric materials," *J. Alloy. Compd.*, vol. 508, p. 14, 2010.

[39] P. Gorrá, J. Sánchez-Lamazares, P. Alvarez, M. Pérez, J. Sanchez-Marcos, and J. Blanco, "Relative cooling power enhancement in magneto-caloric nanostructured pr2fe17," *J. Phys. D Appl. Phys.*, vol. 41, p. 192003, 2008.

[40] B. Hansen, R. Kuhn, L. Bahl, C. R. H. Lundberg, M. C. Ancona-Torres, and M. Katter, "Properties ofmagnetocaloricla(fe,co,si)$_1$3 produced by powder metallurgy," *Journal of Magnetism and Magnetic Materials*, vol. 322, p. 3447, 2010.

[41] R. Bjørk, C. R. H. Bahl, and M. Katter, "Magnetocaloric properties of lafe13-x-ycoxsiy and commercial grade gd," *Journal of Magnetism and Magnetic Materials*, vol. 322, p. 3482, 2010.

[42] Y. Long, Z. Y. Zhang, D. Wen, R. C. Wu, G. H. andYe, Y. Q. Chang, and F. R. Wan, "Controlled oxidation of feco magnetic nanoparticles to produce faceted feco/ferrite nanocomposites for rf heating applications," *J. Appl. Phys.*, vol. 98, p. 033515, 2005.

[43] O. Kubaschewski and C. B. Alcock, *Metallurgical thermochemistry,*. Pergamon International Library. Pergamon Press, 1979.

[44] K. J. Miller, M. Sofman, K. McNerny, and M. E. McHenry, "Metastable γ-feni nanostructures with tunable curie temperature," *J. Appl. Phys.*, vol. 107, p. 09A305, 2010.

[45] R. Scorzelli, "A study of phase stability in invar feni alloys obtained by non-conventional methods," *Hyperfine Interactions*, vol. 110, p. 143, 1997.

[46] R. O'Handley, *Modern magnetic materials: principles and applications*. Wiley New York, 2000.

[47] C. Suryanarayana, *Non-equilibrium processing of materials*. Oxford: Pergamon Press, 1999.

[48] H. H. Liebermann, *Rapidly solidified alloys: Processes, structures, properties, applications.* New York, NY: Marcel Dekker, 1993.

[49] C. Koch and R. W. Cahn, *Processing of metals and alloys, vol. 15 of materials science and technology-a comprehensive treatment.* Weinheim, Germany: VCH Verlagsgesellschaft GmbH, 1991.

[50] K. Upadhya, *Plasma synthesis and processing of materials.* Warrendale, PA: TMS, 1993.

[51] R. Bickerdike, D. Clark, J. Easterbrook, G. Hughes, W. Mair, P. Partridge, and H. Ranson, *Internat J Rapid Solidification*. 1984.

[52] F. Froes, C. Suryanarayana, K. Russell, and C.-G. Li *Mater Sci and Engng*, vol. A192/193, p. 612, 1995.

[53] J. J. Dunkley, "Atomization, metal powder production and characterization, powder metal technologies and applications," *ASM International*, vol. 7, p. 35, 1998.

[54] C. Suryanarayana, "Mechanical alloying and milling," *Progress in Materials Science*, vol. 46, p. 1, 2001.

[55] C. Koch, "Milling of brittle and ductile materials, metal powder production and characterization, powder metal technologies and applications," *ASM International*, vol. 7, p. 53, 1998.

[56] W. Hume-Rothery and G. Raynor, *The structure of metals and alloys.* London: Institute of Metals, 1962.

[57] C. Kuhrt and L. Schultz, "Phase formation and martensitic transformation in mechanically alloyed nanocrystalline feni," *J. Appl. Phys.*, vol. 73, p. 1975, 1993.

[58] T. B. Editors, Massalski, H. Okamoto, P. R. Subramanian, and L. Kacprzak, "Binary alloy phase diagrams, 2nd ed.," *ASM International*, vol. 2, p. 1736, 1990.

[59] C. Yang and D. Williams, "A revision of the fe-ni phase diagram at low temperatures ($< 400\,^{\circ}$c," *Journal of Phase Equilibria*, vol. 17, p. 522, 1996.

[60] K. Reuter, D. Williams, and J. Goldstein, "Determination of the fe-ni phase diagram below $400\,^{\circ}$c," *Metallurgical Transactions A*, vol. 20A, p. 719, 1989.

[61] L. Takacs and M. Pardavi-Horvath, "Nanocomposite formation in the fe3o4-zn system by reaction milling," *J. Appl. Phys.*, vol. 75, p. 5864, 1994.

[62] C. Suryanarayana, "Metal powder production and characterization," *ASM International*, vol. 7, p. 80, 1998.

[63] M. Miki, T. Yamasaki, and Y. Ogino, "Preparation of nanocrystalline nbn and (nb, al)n powders by mechanical alloying under nitrogen atmosphere," *Mater Trans Japan Inst Metals*, vol. 75, p. 839, 1992.

[64] C. Koch *Journal of Mechanochem and Mechanical Alloying*, vol. 1, p. 56, 1994.

[65] R. Davis, B. McDermott, and C. Koch *Metall Trans*, vol. A19, p. 2867, 1988.

[66] R. Schulz, M. Trudeau, J. Huot, and N. Van *A. Phys Rev Lett.*, vol. 62, p. 2849, 1989.

[67] B. D. Cullity and S. Stock, *X-ray Diffraction*. Prentice Hall,, 2001.

[68] R. E. Rosensweig, *Ferrohydrodynamics*. Cambridge University Press, Cambridge, UK, 1985.

[69] G. Brown, "Magnetic heat pumping near room temperature," *J. Appl. Phys.*, vol. 47, p. 3673, 1976.

[70] J. A. Barclay, "Use of a ferrofluid as the heat exchange fluid in a magnetic refrigerator," *J. Appl. Phys.*, vol. 53, p. 2887, 1982.

[71] W. A. Steyert, "Stirling cycle rotating magnetic refrigerators and heat engines for use near room temperature," *J. Appl. Phys.*, vol. 49, p. 1216, 1978.

[72] J. R. Gomez, R. Ferreiro Garcia, A. De Miguel Catoira, and M. R. Gomez, "Magnetocaloric effect: A review of the thermodynamic cycles in magnetic refrigeration," *Renewable and Sustainable Energy Reviews*, vol. 17, p. 74, 2013.

[73] "Toyota motor corporation, public affairs division, toyota hybrid system," 2003.

[74] I. Hilger, W. Andra, R. Hergt, R. Hiergeist, H. Schubert, and W. A. Kaiser, "Electromagnetic heating of breast tumors in interventional radiology: in vitro and in vivo studies in human cadavers and mice," *Radiology*, vol. 218, p. 570, 2001.

[75] K. McNerny, Y. Kim, D. E. Laughlin, and M. E. McHenry, "Chemical synthesis of monodisperse γ-fe-ni magnetic nanoparticles with tunable curie temperatures for self-regulated hyperthermia," *J. Appl. Phys.*, vol. 107, p. 09A312, 2010.

[76] L. H. Lewis and F. Jimenez-Villacorta, "Perspectives on permanent magnetic materials for energy conversion and power generation," *Metallurgical and Materials Transaction*, vol. 44A, p. S2, 2012.

[77] W. Benecki, "A producers and buyers perspective: The permanent magnet outlook," *Magnetics 2008 Conference, Denver, CO*, 2008.

[78] J. J. Ipus, P. Herre, P. Ohodnicki, and M. E. McHenry, "High temperature x ray diffraction determination of the body-centered-cubicface-centered-cubic transformation temperature in (fe70ni30)88zr7b4cu1 nanocomposites," *J. Appl. Phys.*, vol. 111, p. 07A323, 2012.

[79] L. Swartzendruber, V. Itkin, and C. Alcock, "The fe-ni (iron-nickel) system," *J. Phase Equilib.*, vol. 12, p. 288, 1991.

[80] D. Porter and K. Easterling, *Phase transformations in Metals and Alloys*. CRC Press United Kingdom, 2001.

[81] P. Poddar, S. Srinath, J. Gass, B. L. V. Prasad, and H. Srikanth, "Magnetic transition and large magnetocaloric effect associated with surface spin disorder in co and co core ag shell nanoparticles," *J. Phys. Chem.*, vol. 111, p. 14060, 2007.

[82] N. J. Jones, K. L. McNerny, A. T. Wise, M. Sorescu, and D. E. McHenry, M. E.and Laughlin, "Observations of oxidation mechanisms and kinetics in faceted feco magnetic nanoparticles," *J. Appl. Phys.*, vol. 107, p. 09A304, 2010.

[83] P. R. Ohodnicki, D. E. Laughlin, M. E. McHenry, and M. Widom, "Application of classical nucleation theory to phase selection and composition of nucleated nanocrystals during crystallization of co-rich (co,fe)-based amorphous precursors.," *Acta Mat.*, vol. 58, p. 4804, 2010.

[84] K. N. Collier, N. J. Jones, K. J. Miller, Y. L. Qin, D. E. Laughlin, and M. E. McHenry, "Controlled oxidation of feco magnetic nanoparticles to produce faceted feco/ferrite nanocomposites for rf heating applications," *J. Appl. Phys.*, vol. 105, p. 07A328, 2009.

[85] S. K. Banerjee *Phys Lett.*, vol. 12, p. 16, 1964.

[86] P. Lampen, A. Puri, M. Phan, and H. Srikanth, "Structure, magnetic, and magnetocaloric properties of amorphous and crystalline la0.4ca0.6mno3+a nanoparticles," *Journal of Alloys and Compounds*, vol. 512, p. 94, 2012.

[87] "Joint committee on powder diffraction standards," *The International Center for Diffraction Data*, pp. file 89–0686, 1999.

[88] L. B. Hong and B. Fultz, "Two-phase coexistence in feni alloys synthesized by ball milling," *J. Appl. Phys.*, vol. 79, p. 3946, 1996.

[89] P. Gorria, R. Boada, A. Fernandez-Martinez, G. Garbarino, R. I. Smith, J. Chaboy, J. I. Garca Alonso, D. Martnez-Blanco, , G. R. Castro, M. Mezouar, A. Hernando, and J. A. Blanco, "Stress-induced curie temperature increase in the fe64ni36 invar alloy," *Phys. Status Solidi*, vol. 3, p. 115, 2009.

[90] "Spex sample prep sample container materials selection chart," *www.spexsampleprep.com*.

[91] M. Hansen, *Constitution of Binary alloys.* Julius Springer, Berlin.

[92] J. Marsh, *Alloys of Iron and Nickel*. McGraw Hill, N.Y.

[93] V. Franco, A. Conde, M. D. Kuzmin, and J. M. Romero-Enrique, "The magnetocaloric effect in materials with a second order phase transition: Are tc and tpeak necessarily coincident?," *J. Appl. Phys.*, vol. 105, p. 07A917, 2009.

[94] . V. Franco, A. Conde, M. D. Kuzmin, and J. M. Romero-Enrique, "The magnetocaloric effect in materials with a second order phase transition: Are tc and tpeak necessarily coincident?," *J. Appl. Phys.*, vol. 105, p. 07A917, 2009.

[95] M. D. Kuz min and T. A. M. Richter, Manuel and, "The magnetocaloric effect in materials with a second order phase transition: Are tc and tpeak necessarily coincident?," *Journal of Magnetism and Magnetic Materials*, vol. 321, p. L1, 2009.

[96] V. Franco, C. F. Conde, A. Conde, and L. F. Kiss, "Enhanced magnetocaloric response in cr/mo containing nanoperm-type amorphous alloys," *Applied Physics Letters*, vol. 90, p. 052509, 2007.

[97] G. Y. Chin and e. b. W. E. P. Wernick, J. H., *in Ferromagnetic Materials, (1980), p. 55*. North-Holland, Amsterdam, 1980.

[98] H. Ucar, J. J. Ipus, V. Franco, M. E. McHenry, and D. E. Laughlin, "Overview of amorphous and nanocrystalline magnetocaloric materials operating near room temperature," *Journal of Metals*, vol. 64, p. 782, 2012.

[99] V. I. Zverev, A. M. Tishin, and M. D. Kuzmin, "The maximum possible magnetocaloric $delta$t effect," *J. Appl. Phys.*, vol. 107, p. 043907, 2010.

[100] K. G. Sandeman, "Magnetocaloric materials: The search for new systems," *Scripta Materialia*, vol. 67, p. 566, 2012.

[101] S. Kaloshkin, V. Tcherdyntsev, I. Tomilin, Y. Baldokhin, and E. Shelekhov, "Phase transformations in feni system at mechanical alloying and consequent annealing of elemental powder mixtures," *Physica B*, vol. 299, p. 236, 2001.

[102] W. L. Roth *Phys. Rev.*, vol. 110, p. 1333, 1958.

[103] A. Smaili and R. Chahine, "Composite materials for ericsson-like magnetic refrigeration cycle," *J. Appl. Phys.*, vol. 81, p. 824, 1997.

[104] A. Smaili and R. Chahine, "Composite materials for ericsson-like magnetic refrigeration cycle,"

[105] I. G. de Oliveiraa, P. J. von Rankec, and E. P. Nobrega, "Understanding the table-like magnetocaloric effect," *Journal of Magnetism and Magnetic Materials*, vol. 261, p. 112, 2003.

[106] A. Chaturvedi, S. Stefanoski, M. Phan, G. S. Nolas, and H. Srikanth, "Table-like magnetocaloric effect and enhanced refrigerant capacity in eu8ga16ge30-euo composite materials," *J. Appl. Phys.*, vol. 99, p. 162513, 2011.

[107] B. Cullity and C. Graham, *Introduction to magnetic materials*. Wiley-IEEE Press, 2008.

[108] R. M. Bozorth, *Ferromagnetism*. New York, D. Van Nostrand Company, 1951.

[109] S. Chikazumi and C. Graham, *Physics of ferromagnetism*, vol. 94. Oxford University Press, USA, 2009.

[110] K. Ishida and T. Nishizawa, "Ferrite/austenite stabilizing parameters of alloying elements in steel at 200-500c," *Trans. JIM*, vol. 15, p. 217, 1974.

[111] N. Enomoto, M. and Maruyama, K. M. Wu, and T. Tarui, "Alloying element accumulation at ferrite/austenite boundaries below the time/temperature/transformation diagram bay in an fe/c/mo alloy," *Materials Science and Engineering*, vol. A343, p. 151, 2003.

[112] L. Vitos, P. A. Korzhavyi, and B. Johansson, "Elastic property maps of austenitic stainless steels," *Physical Review Letters*, vol. 88, pp. 155501–1, 2002.

[113] J. Kirkaldy, "Prediction of alloy hardenability from thermodynamic and kinetic data," *Metallurgical Transactions*, vol. 4, p. 2327, 1973.

[114] M. G. Akben, B. Bacroix, and J. J. Jonas, "Effect of vanadium and molybdenum addition on high temperature recovery, recrystallization and precipitation behavior of niobium-based microalloyed steels," *Acta Metall*, vol. 31, p. 161, 1983.

[115] M. I. Ahmed, I. Nasim, and S. Husain, "Influence of nickel and molybdenum on the phase stability and mechanical properties of maraging steels," *Journal of Materials Engineering and Performance*, vol. 3(2), p. 249, 1994.

[116] J. Friedel and N. Cimento, "On some electrical and magnetic properties of metallic solid solutions," *Metallic alloys*, vol. 10, p. 287, 1958.

[117] A. P. Malozemoff, A. R. Williams, and V. L. Moruzzi, ""band-gap theory" of strong ferromagnetism: Application to concentrated crystalline and amorphous fe- and co-metalloid alloys," *Physical Review B*, vol. 29, p. 1620, 1984.

[118] M. Ghemawat, A. McHenry and R. OHandley, "Magnetic moment suppression in rapidly solidified co-te-b alloys," *J. Appl. Phys.*, vol. 63, p. 3388, 1988.

[119] J. J. Ipus, H. Ucar, and M. E. McHenry, "Near room temperature magnetocaloric response of an (feni)zrb nanocomposite alloy.," *IEEE Trans. Magn.*, vol. 47, p. 2494, 2011.

[120] C. L. Ondeck, A. H. Habib, P. R. Ohodnicki, K. Miller, C. A. Sawyer, P. Chaudhary, and M. E. McHenry, "Theory of magnetic fluid heating with an alternating magnetic field with temperature dependent materials properties for self-regulated heating.," *J. Appl. Phys.*, vol. 105, p. 07B324, 2009.

[121] "www.metalprices.com,"

[122] D. U. G. Washington, "Us energy information administration,"